Quaternary grounding-line fluctuations in Antarctica

Trevor Ray Hillebrand

A dissertation

submitted in partial fulfillment of the

requirements for the degree of

Doctor of Philosophy

University of Washington

2019

Reading Committee:

John O.H. Stone, Chair

Michelle R. Koutnik

Howard B. Conway

Program Authorized to Offer Degree:

Earth and Space Sciences

University of Washington

Abstract

Quaternary grounding-line fluctuations in Antarctica

Trevor Ray Hillebrand

Chair of the Supervisory Committee:
Dr. John O.H. Stone
Department of Earth and Space Sciences

The West Antarctic Ice Sheet may be prone to rapid collapse under climates warmer than today due to a dynamic instability at the grounding line, where the ice sheet goes afloat over seawater. However, there is to-date no conclusive evidence that the ice sheet has gone away in last few million years. Thus, characterizing and understanding the transitions between the glacial and interglacial states of the ice sheet is a fundamental step towards predicting its response to future warming. Here, I investigate the history of ice sheet fluctuations in the Ross and Weddell Sea sectors of Antarctica over thousand- to million-year timescales, using cosmogenic nuclide analysis of glacial deposits and glaciated bedrock surfaces, ice-penetrating radar surveys, and numerical modeling of radar waveforms and ice flow. I have mapped and dated glacial deposits from Darwin and Hatherton glaciers, which have been used to constrain the last deglaciation in the Ross Embayment. I find that these glaciers thinned slowly and steadily through the Holocene,

thousands of years later than other glaciers in the region. I use ice flow models to show (1) that their thickness changes require changing catchment boundaries upstream, and (2) that ice thickness changes at the glacier mouth are not a simple proxy for grounding line position. Next, I present new ice-penetrating radar surveys from Crary Ice Rise, a promontory in the Ross Ice Shelf that provides stability to portions of the West Antarctic Ice Sheet. I find that the ice rise contains large amounts of marine ice that accreted in basal crevasses and rifts before or during ice rise formation. Marine ice could have strengthened the damaged ice shelf, facilitating ice rise formation. Finally, I use cosmogenic nuclide concentrations in a subglacial bedrock core and a large ensemble of ice sheet model simulations to investigate the long-term stability of the West Antarctic Ice Sheet. The concentrations in the core preclude 150 m of ice sheet thinning at the Pirrit Hills since at least 2 Ma. The ice sheet model results show that continuous burial of the bedrock core requires a stable Filchner-Ronne ice shelf.

TABLE OF CONTENTS

LIST OF FIGURES

LIST OF TABLES

ACKNOWLEDGEMENTS

None of this work could have been done without the aid of my mentors. Twit Conway and Michelle Koutnik have provided me with incredible opportunities and indispensable guidance time after time. Bernard Hallet enticed me to come to the University of Washington by sending me to Nepal for a month. John Stone has given me freedom, support, and coffee throughout my entire time at the UW. The other members of the UW glaciology group have always offered constructive feedback and creative ideas. I am especially indebted to Perry Spector, T.J. Fudge, David Shean, Knut Christianson, Nick Holschuh, and Ed Waddington in this regard.

Next, I must thank the friends who got me through six years of graduate school: Chloe Hart, Matthew Koehler, Luke Dow, and Hannah Glover. Without their constant companionship, I would be a much more mature and successful individual than I am today. Bryan Stockton, my oldest friend, provided a place to live while finishing my dissertation, and refused payment.

Finally, I thank my family. My mom and dad have always supported me in every endeavor, and are the most patient, kind, and fun people I know. Fletcher never beat me up when I deserved it. Petra, my sister-out-law, kept me in check. Rob and Shirley welcomed me into their family. Sarah has gotten me through every bad time of the last six years. Without her, I would be nowhere.

DEDICATION

For Uncle Tim, the original Dr. Hillebrand.

Chapter 1. INTRODUCTION

The West Antarctic Ice Sheet (WAIS) could be susceptible to rapid retreat under climates warmer than today (Weertman, 1974; Mercer, 1978). The fate of the ice sheet hinges on the stability of the grounding line, where the ice becomes thin enough to achieve floatation and lose contact with the bed. Ice flux across the grounding line is strongly dependent on ice thickness, so grounding-line retreat into an area of thicker ice can lead to a runaway retreat of the ice sheet (Schoof, 2007). Much of the WAIS lies on a bed far below sea level, which deepens towards the ice sheet interior. The marine-based sectors of the WAIS contain ~3.3 m of global sea level equivalent (Bamber et al., 2009). Marine ice sheet retreat could already be underway in one sector of the ice sheet (Joughin et al., 2014), driven by increased access of warm Circumpolar Deep Water to the ice shelves and grounding lines of the Amundsen Sea sector (Hellmer et al., 2012). While ice sheet model projections vary widely, the most drastic scenarios predict total deglaciation of the marine basins of the WAIS within centuries (DeConto and Pollard, 2016).

Yet, there is still no definitive evidence that the WAIS has collapsed in the past. Global mean sea level prior to 800 kyr BP is essentially unconstrained (Raymo et al., 2018). Sea level during the warmest interglacials of the last 800 kyr was likely 6 - 13 m higher than present (Raymo and Mitrovica, 2012; Dutton et al., 2015; Spratt and Lisiecki, 2016). Cosmogenic nuclide measurements in subglacial bedrock recovered from beneath the GISP2 ice core in central Greenland show that the ice sheet has been 90 – 95% smaller than today for a total of ~300 kyr during the Pleistocene (Schaefer et al., 2016). The Greenland ice sheet contains ~7 m of global sea-level equivalent and could thus account for all or most of the excess volume of the oceans during warm interglacial periods of the last 800 kyr. However, estimates of the Greenland Ice

Sheet contribution to the last interglacial sea level are generally <3.5 m (NEEM community Members et al., 2013; Stone et al., 2013), which does imply a substantial contribution from the WAIS. Ice sheet models that simulate WAIS collapse during the last interglacial require ocean warming of >2°C relative to present day (DeConto and Pollard, 2016; Sutter et al., 2016), but ocean temperature proxy estimates do not unequivocally pass this threshold, and model-based estimates are generally lower (Capron et al., 2014).

Recent work has highlighted stabilizing mechanisms that could effectively counteract the Marine Ice Sheet Instability, and existing geologic constraints and current glaciological assumptions are now being called into question. Pleistocene marine diatoms and meteoric ^{10}Be found in subglacial sediments beneath the WAIS were formerly thought to be the best evidence of large-scale ice sheet collapse (Scherer et al., 1998). Recent ^{14}C analyses of these sediments indicate that the grounding line has been far upstream of its modern position in the last few kyr, and subsequently re-advanced due to glacial isostatic adjustment before the ice sheet could collapse (Kingslake et al., 2018). A rapid solid earth response to the decreasing ice load could also be stabilizing the Amundsen Sea sector of the ice sheet (Barletta et al., 2018; Larour et al., 2019), long thought to be the most vulnerable part of the ice sheet to warming ocean temperatures (Hughes, 1981). It is increasingly apparent that the thresholds of ice sheet collapse are not understood.

This dissertation comprises three projects motivated by the need to understand past ice sheet changes in Antarctica. In Chapter 2, *Holocene thinning and grounding-line retreat of the Darwin-Hatherton glacier system, Antarctica* I present mapping and geochronology of extensive glacial deposits from the Darwin and Hatherton Glaciers in the Transantarctic Mountains. I constrain a flowband model of the glacier system with these data to help understand the controls

on glacier retreat following the last glaciation, and to determine how well the response of these glaciers represents the larger ice sheet. In Chapter 3, *Structure of Crary Ice Rise revealed by HF and UHF radio-echo sounding,* I characterize the englacial structures of an important yet understudied feature at the grounding line of the Ross Ice Shelf. I use a 2D numerical waveform model to test hypotheses for the properties and origins of the detected structures within the ice. In Chapter 4, *West Antarctic Ice Sheet fluctuations during Pleistocene interglacials,* I use a large ensemble of 3D ice sheet model simulations to understand what a point measurement of burial and/or exposure can tell us about the stability of the whole ice sheet over long timescales.

Chapter 2. HOLOCENE THINNING AND GROUNDING-LINE RETREAT OF DARWIN AND HATHERTON GLACIERS, ANTARCTICA

Trevor R. Hillebrand, John O. Stone, Courtney King, Michelle Koutnik, Howard Conway, Brenda Hall, Brent Goehring, Keir Nichols, Mette K. Gillespie, David Pollard

2.1 ABSTRACT

Exposure ages and radiocarbon ages of glacial deposits at four locations alongside Hatherton and Darwin glaciers record several hundred meters of late Pleistocene to early Holocene thickening relative to present. As the grounding-line of the Ross Sea Ice Sheet retreated rapidly southward, Darwin and Hatherton Glaciers thinned steadily through the Holocene, until about 3 kyr BP. This contrasts with records from many other glaciers in the Transantarctic Mountains, which experienced a drawdown of hundreds of meters over roughly a one-thousand-year period in the early Holocene. We model these glaciers using a 1.5-dimensional flowband model, and find that our data imply a near doubling of the catchment area at the Last Glacial Maximum relative to today, followed by a steady decrease in catchment area and slow and steady thinning at the glacier mouth from 10-3 kyr BP. Results from an ensemble of three-dimensional ice-sheet model runs suggest that Darwin and Hatherton Glaciers are strongly buttressed by convergent flow with neighboring Byrd and Mulock glaciers, and by lateral drag past Cape Crozier and Minna Bluff, which could have led to a pattern of grounding-line retreat distinct from other glaciers throughout the Transantarctic Mountains. These results highlight the difficulties inherent in constraining the

timing and pattern of grounding-line retreat from terrestrial records, but also offer insights into some of the complexities of ice dynamics during the last deglaciation in the Ross Embayment of Antarctica.

2.2 INTRODUCTION

Quaternary glacial deposits preserved in ice-free regions in the Darwin-Hatherton Glacier system (DHGS) have been used to infer glacial history of the region (Bockheim et al., 1989; Storey et al., 2010; Joy et al., 2014; King, 2017). In this paper, we present new glacial geologic maps, new exposure ages of 95 samples of glacial erratics and bedrock, and 129 new radiocarbon ages of freeze-dried algae from former ice-marginal ponds (King, 2017). We use these data to constrain a 1.5-D glacier flowband model of the DHGS forced by an ensemble of Pennsylvania State University (PSU) 3-D ice sheet model simulations (Pollard & DeConto, 2009; 2012), to investigate the most recent deglaciation of the DHGS and the former Ross Ice Sheet.

2.2.1 *The last deglaciation in the Ross Embayment*

A thick ice sheet filled the Ross Embayment of Antarctica during Marine Isotope Stage 2 (MIS-2; 29-14 kyr BP), grounded near Coulman Island (Figure 2-1); the grounding-line of the Ross Ice Sheet retreated more than 1,200 km to its current position from 13 to 2 kyr BP (Anderson et al., 2014). Conway et al. (1999) proposed that grounding-line recession followed the pattern of a swinging gate, with its hinge in the eastern Ross Sea. Radiocarbon ages from deposits alongside Hatherton Glacier (Bockheim et al., 1989) suggested that the glacier had reached its modern configuration >6.8 kyr BP, which provided one of the key constraints for this model of grounding-line retreat.

The ~800 km-long section of the Transantarctic Mountains (TAMs) front between Terra Nova Bay and Shackleton Glacier may have deglaciated almost simultaneously in the early Holocene, followed by slow recession into the late Holocene (Spector et al., 2017). Shackleton and Beardmore Glaciers had reached their modern configurations by 7.4 kyr BP, roughly contemporaneous with dramatic thinning in McMurdo Sound (Baroni and Hall, 2004; Hall et al., 2004) and at Mackay Glacier (Jones et al., 2015). The pattern of deglaciation was likely complex, as the grounding-line temporarily stabilized on pinning points and retreated in deep troughs (Dowdeswell et al., 2008; Halberstadt et al., 2016). Ice sheet thinning in the southern Ross Embayment slowed as the grounding-line neared its modern positions between Scott and Reedy glaciers around 3 kyr BP (Spector et al., 2017).

2.2.2 *Physiographic setting of Darwin and Hatherton Glaciers*

Darwin Glacier and its major tributary Hatherton Glacier are outlets of the East Antarctic Ice Sheet that flow through the TAM into the modern Ross Ice Shelf. In contrast to the neighboring fast-flowing Byrd and Mulock glaciers, ice-flow velocities for the DHGS do not exceed 110 m yr^{-1}, and everywhere the velocity of Hatherton Glacier is <12 m yr^{-1} (Rignot *et al.*, 2011; Gillespie *et al.*, 2017). The catchment for the DHGS is small (8060 km^2) due to both high bedrock topography preventing flow into their canyons and to the proximity of the much larger Byrd and Mulock glaciers, whose catchments effectively cut off the Darwin-Hatherton catchment (Swithinbank *et al.*, 1988; Gillespie *et al.*, 2017). While Byrd and Mulock glaciers currently contribute about 22 and 5 Gt a^{-1} to the Ross Ice Shelf, respectively (Stearns, 2011), Darwin Glacier contributes 0.24 ± 0.05 Gt a^{-1} (Gillespie et al., 2017).

The surface mass balance of the DHGS is spatially complex, with persistent blue ice areas and seasonal surface melt (Brown and Scambos, 2004; Gillespie et al., 2017). The boundary layer

meteorology is dominated by strong, dry, and cold downslope winds between April and September, with mean monthly air temperatures around -25°C (Noonan *et al.,* 2015). In December and January, relatively humid winds dominate, and mean monthly temperatures rise to -4°C. Blue ice areas form due to convergence of katabatic winds and due to turbulence as the winds flow over mountains and nunataks (Bintanja, 1999). Therefore, most ablation likely occurs during the winter months, due to removal of surface snow by strong downslope winds. Brown and Scambos (2004) showed that blue ice areas on Darwin Glacier are likely very near their maximum extent, and only small climate fluctuations are required to greatly reduce their area. Gillespie et al. (2017) noted that of the available gridded data products that provide estimates of the surface mass balance over the Darwin-Hatherton glacier system (Arthern *et al.,* 2006; van de Berg *et al.*, 2006; Lenaerts *et al.*, 2012a; Lenaerts *et al.*, 2012b) only the 5.5 km simulation of Lenaerts et al. (2012a) (hereafter referred to as RACMO 2.1; Lenaerts *et al.*, 2012b as RACMO 2.3) includes ablation areas; however, the modeled spatial pattern of ablation does not match observed blue ice extents.

Numerous lakes and ponds are found at the edges of Darwin and Hatherton glaciers, including large frozen lakes at the glacier margins, seasonal supraglacial ponds at low elevations, and isolated moraine-dammed ponds around Diamond Hill (Webster-Brown et al., 2010). While some of the larger lakes could be frozen through to their beds, the ice-shelf dammed Lake Wilson is capped by floating ice, with a stratified water column ~100 m deep (Hendy, 2000; Webster et al., 1996). All of these environments host modern blue-green algae (cyanobacterial mats), which are the living equivalents of the freeze-dried algae material preserved within glacial deposits and described by Bockheim et al. (1989) and King (2017).

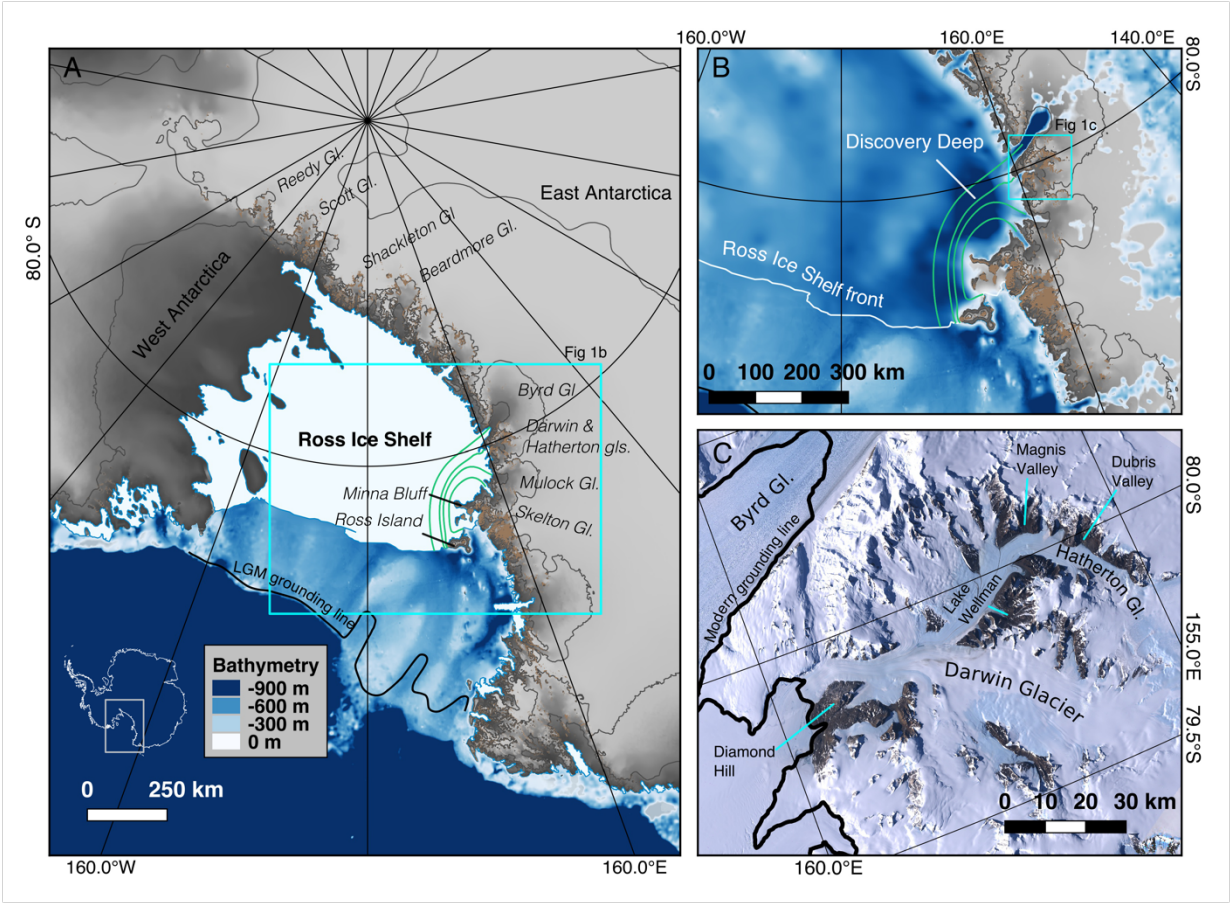

Figure 2-1: A) The Ross Embayment of Antarctica, with regional and study locations noted. The modern ice sheet surface is shown in grey, the modern ice shelf is shown in white and exposed rock is shown in brown. Bathymetry beyond the Ross Ice Shelf front is shown in blues (Fretwell et al., 2013). Flowlines through the ice shelf from Byrd, Darwin, Mulock, and Skelton glaciers are shown in green, and calculated using the MATLAB toolbox of Greene et al. (2017). B) Inset of area outlined with cyan box in panel A, with bathymetry shown in the same colormap as panel A. The combined Byrd-Darwin-Mulock-Skelton flow path covers Discovery Deep, which is the deepest part of the seafloor in the Ross Embayment. C) Landsat image of Darwin and Hatherton Glaciers, with labels for locations mentioned in the text. The modern grounding line is shown by the thick black line. Note the prominent blue-ice field on the glacier surfaces.

Gillespie et al. (2017) provided the first measurements of ice thickness for Darwin and Hatherton glaciers and characterized the glacier beds using ground-based and airborne ice-penetrating radar. The modern grounding-line of Darwin Glacier sits on a forward sloping bed ~925 m below sea level. The bed reflection is weak with numerous hyperbolae, characteristic of a

frozen and rough bed with basal crevasses. The basal reflection is stronger and smoother beneath the floating ice shelf downstream from the grounding line. Hydrostatic equilibrium is reached ~2.5 km downstream of the grounding-line (Gillespie et al., 2017).

Farther into the Ross Ice Shelf, ice from the DHGS converges with ice from Byrd and Mulock glaciers (Figure 2-1). The convergence occurs over 'Discovery Deep', the deepest part of the Ross seafloor on the continental shelf (up to ~1300 m below sea level). On the south side of the flow path from Byrd Glacier, tensile crevasses and rifts are oriented ~45° to flow; however, the stress exerted by Darwin and Mulock glaciers causes the crevasses and rifts on the north side to be angled ~30° to the flow direction (Hughes et al., 2017). Thomas et al. (1984) measured positive vertical strain rates along this flow path south of Minna Bluff. They suggested that the convergence of flow from Byrd, Mulock, Darwin, and Skelton glaciers, combined with the influence of Minna Bluff causes the ice shelf there to thicken. Whillans and Merry (2001) also identified Minna Bluff and Cape Crozier as obstacles that provide stabilizing backpressure to the Ross Ice Shelf and cited the presence of rifts at the tip of Minna Bluff as evidence of stress concentration on the upstream side. Hughes et al. (2017) posited that Byrd Glacier effectively buttresses ice from West Antarctica by "nailing" the Ross Ice Shelf to the TAM and reducing extensional strain rates in the ice shelf. If this is correct, the history of ice dynamics in the Byrd-Darwin-Mulock region may be key to understanding grounding-line retreat of the West Antarctic Ice Sheet during the last deglaciation.

2.2.3 *The Darwin-Hatherton Glacier System during Marine Isotope Stage 2 and the Holocene*

Outlet glaciers throughout the TAM thickened first at their mouths during MIS-2 in response to grounded, thickening ice in the Ross Sea, and later at their heads due to increased

accumulation after the LGM (Todd et al., 2010). Lateral moraines of MIS-2 age have been used to interpret ice thicknesses of both the grounded Ross Ice Sheet and EAIS outlet glaciers (Bockheim et al., 1989; Denton et al., 1989; Jones et al., 2015; Joy et al., 2014; Spector et al., 2017; Todd et al., 2010).

Bockheim et al. (1989) mapped lateral moraines and drift sheets in ice-free valleys alongside Hatherton Glacier, and dated these deposits based on weathering, soil characteristics, and radiocarbon ages of freeze-dried algae. These algae grew in glacier-dammed ponds and died when the ponds disappeared as the glacier retreated downslope; the ages provide a proxy for the glacier margin position through time. Bockheim et al. (1989) tentatively attributed the Britannia II drift sheet to the LGM and interpreted the less extensive Britannia I drift as a period of re-advance or stability of the glacier margin in the Holocene. They named the unweathered drift sheet immediately adjacent to the glacier margin the Hatherton drift. Two much older drifts were termed the Danum and Isca, and inferred to date to MIS-6 and a much older glaciation, respectively.

The Britannia II drift lies 100 m above the current glacier margin at the head of Hatherton Glacier, and 450 m above the current margin in the middle of the glacier profile. Bockheim et al. (1989) extrapolated these elevations to infer up to 1100 m of thickening at the confluence of Darwin Glacier with the Ross Ice Sheet during MIS-2, although they found no deposits there. Subsequent numerical modeling experiments by Anderson *et al.,* (2004) yielded a more modest 800 m of thickening, although they had to infer the bed topography by mass conservation.

Storey et al., (2010) revisited the Lake Wellman area, where Bockheim et al. (1989) found 450 m of LGM thickening and used surface exposure dating to determine the age of the Britannia and Hatherton drift limits. Their exposure ages suffer from significant pre-exposure, resulting in a random distribution of ages and an overestimate of exposure since the LGM. Our own efforts to

use surface exposure dating at Lake Wellman were also thwarted by prior exposure, but King (2017) was able to date the advance and retreat of Hatherton Glacier in the Lake Wellman valley using radiocarbon dating of freeze-dried algae. Joy et al. (2014) measured the exposure age of deposits in Dubris and Bibra Valleys alongside the upper Hatherton Glacier. They showed the Britannia II drift is in fact of MIS-6 (~125 kyr BP) age, and the Britannia I drift is of Holocene age.

Bockheim et al.'s (1989) deglaciation chronology of Hatherton Glacier was based on a small number of bulk radiocarbon ages, which likely resulted in an averaging effect on the ages. Furthermore, the majority of the samples were more than 50 km upglacier from the modern grounding line. Anderson et al. (2004) used a numerical model of the DHGS to show that fluctuations of Hatherton Glacier may have lagged changes at the mouth of Darwin Glacier by as much as 1100 years. Here we present additional constraints needed to infer the regional deglaciation history of the DGHS.

2.3 RECORDS OF GLACIER FLUCTUATIONS

2.3.1 *Geochronological methods*

2.3.1.1 Exposure dating of bedrock and glacial erratics

We selected minimally weathered samples from the Britannia and Hatherton deposits in an attempt to avoid sampling rocks with prior exposure to cosmic rays. We avoided sampling rocks near frost cracks or atop thick deposits or moraines, as these could have been disturbed (e.g., rolled or exhumed by cryoturbation) after deposition, leading to anomalously young exposure ages. We also noted the relative height of nearby boulders and the dominant orientation of local snowfields so as to avoid sampling rocks that may have been covered by deep snow. However, significant

attenuation of the cosmic ray flux requires a large amount of snow; for example, 1 m of dense (400 kg/m^3), wind-packed snow would reduce the production rate of cosmogenic isotopes by ~22%. In these wind-swept areas adjacent to blue ice glacier margins, it is unlikely that such deep snow cover would persist for long enough to strongly skew the exposure ages. Furthermore, the internal consistency of the exposure-age datasets (with the exception of the samples from Lake Wellman) suggest that snow-cover was not an issue for our samples.

We analyzed cosmogenic ^{14}C produced *in situ* in quartz along an elevation transect of granitic bedrock from Diamond Hill in order to constrain the ice thickness there at the LGM. We preferentially sampled very weathered bedrock to ensure minimal erosion over the last glacial cycle. Because any rock exposed prior to the LGM will contain some amount of inherited ^{14}C, an apparent ^{14}C exposure age acts as an upper bound on the timing of exposure since the LGM. Within the range of subaerial erosion rates typical of Antarctic bedrock (<1 m/Myr), ^{14}C concentrations reach secular equilibrium in <30 kyr (Balco et al., 2016). Because of the short half-life of ^{14}C, a few thousand years of ice cover during the LGM will create a detectable signal of burial, while rock that was not covered with ice in the last 30 kyr will remain at its equilibrium concentration. Therefore, the LGM ice surface elevation is bracketed between the lowest sample that is saturated with respect to ^{14}C and the highest unsaturated sample.

We crushed and sieved our rock samples to 250-500 μm, and isolated quartz aliquots using heavy liquid density separation, surfactant separation, and dilute HF etching at 69°C (Kohl and Nishiizumi, 1992). For samples to be analyzed for *in-situ* ^{14}C, the quartz was treated with a HF/HNO_3 solution to remove any extra organic material left behind by the heavy liquids or surfactants, as these can cause very high levels of contamination. We isolated Be and Al from quartz aliquots at the University of Washington Cosmogenic Nuclide Laboratory following the

standard ion-exchange chromatography method of Ditchburn and Whitehead (1994). ^{14}C cathodes were prepared at Tulane University using the new fully-automated carbon extraction and graphitization system (Goehring et al., 2019).

We analyzed samples for *in situ* ^{10}Be and ^{14}C at the Center for Accelerator Mass Spectrometry (CAMS) at Lawrence Livermore National Laboratory. Aluminum-26 was analyzed at the Purdue Rare Isotope Measurement Laboratory (PRIME). The exposure ages presented in this paper have been calculated using the latitude-altitude scaling scheme of Stone (2000). While the choice of another scaling scheme changes the individual exposure ages, there is no major impact on the overall results. We therefore have chosen the simplest and best-established scaling scheme. If desired, the reader may recalculate the exposure ages using the CRONUS v3 calculator (hess.ess.washington.edu) using another scaling scheme.

2.3.1.2 Radiocarbon dating of algae

The Britannia I and Hatherton drifts contain abundant freeze-dried algae that grew in ice-marginal ponds and were preserved within lake pavements and under embedded erratics. Assuming the topography requires an ice dam to hold a pond or lake, these algae act as a proxy for the ice margin location through time. We were careful to sample algae only at locations where the pond would have required the presence of the glacier margin to hold water; however, we acknowledge that outliers may exist due to the progressive down-wasting of ice-cored topography after glacier recession. The algae samples were analyzed for ^{14}C at the National Ocean Sciences Accelerator Mass Spectrometry Laboratory at Woods Hole Oceanographic Institution. We converted isotope ratios to calendar years using CALIB 7.0.2 and the IntCal13 dataset (Reimer et al., 2013). The dates presented here are in calendar years with a reported 1-sigma error. The data we use here have been described by King (2017).

2.3.2 *Description of deposits*

The Britannia II limit lies ~450m above the modern margin of Hatherton Glacier. It is composed of weathered dolerite and yellowed sandstone boulders, which are often chipped and flakey, but very rarely exhibit extensive pitting indicative of very old (>1 Myr) deposits. Unlike the younger deposits, the Britannia II lacks any ice-cored moraines or hummocky topography. In general, the Britannia II grades into the older Danum drift without a clear limit, but boulder-rich moraines do mark the limit in some places.

The Britannia I drift is found up to ~350 m above the modern margin of Hatherton Glacier. The deposit is similar in composition to the Britannia II deposit, though the sandstone clasts are often less weathered. This deposit still retains large ice-cored moraines, especially at Lake Wellman and Magnis Valley. A boulder-rich moraine, sometimes ice-cored, separates the Britannia I and II deposits. We found numerous relict lake pavements within the Britannia I deposit. The deposit thickens towards the glacier margin. Bockheim et al. (1989), Storey et al. (2010), Joy et al. (2014), and King (2017) mapped a boundary between the Britannia I and Hatherton deposits ~50 – 100 m above the modern glacier margin based on deposit thickness and weathering.

The Hatherton drift is a minimally weathered deposit found within 50 – 100 m elevation of the modern margin of Hatherton Glacier. While Bockheim et al. (1989), Storey et al. (2010), and Joy et al. (2014) agree on the general characteristics of the Hatherton drift, their interpretations of its significance differ. Bockheim et al. (1989) posited that the Hatherton drift represents the last pulse of thinning from the high-stand represented by the Britannia deposits (later shown by Joy et al. (2014) and confirmed here to be of different ages). Storey et al. (2010), however, interpreted the Hatherton drift to represent the last local advance of Hatherton Glacier, which they dated to

15-19 kyr BP. In making this interpretation, they discarded several younger ages of <3 kyr BP, using the argument that these could have been recently exhumed from the deposit.

We found no clearly defined demarcation between the Britannia I and Hatherton drifts. The Hatherton drift is thick and ice cored nearest the glacier margin, and thins with distance from the glacier, grading into the Britannia I drift. Based on this gradual transition, and on the radiocarbon chronology of King (2017), we interpret the Hatherton drift as simply the youngest part of the recession from the Britannia I limit. There is no indication in the chronologies or the glacial geology of a significant still-stand or re-advance responsible for depositing the Hatherton drift.

The glacial deposits at Diamond Hill are of two main types: stained, isolated erratics resting stably atop weathered gneissic bedrock, and a thicker, much more weathered deposit filling the valley bottom and the high cirque of Diamond Hill. The older deposit often exhibits pitting and deep brown staining. Near the modern margin of Darwin Glacier, we found stained granite erratics perched atop deeply weathered and glacially sculpted gneissic bedrock. While these erratics were more stained than the LGM and Holocene deposits found on Hatherton Glacier, we nonetheless interpret these to be deposited during the last deglaciation, due to the greater degree of weathering of deposits elsewhere around Diamond Hill. We attribute this greater degree of surface oxidation to the climate conditions at lower elevations, which are often inundated in thick coastal fog and exposed to humid upslope winds from October to February (Noonan et al., 2015). We found no distinct limit of deposition of these younger erratics; we found a single young erratic 135 m above the modern glacier margin, and none higher than that. Based on other evidence of LGM ice thickness hundreds of meters above modern at the mouths of TAM outlet glaciers (Todd et al., 2010; Bromley et al., 2012; Spector et al., 2017), we consider this unlikely to be representative of the LGM glacier surface, but rather simply another recessional erratic. Our surface exposure ages

in Section 2.3 show this to be true. Therefore, it seems that Darwin Glacier left no clearly defined deposit of fresh erratics in the accessible areas of Diamond Hill at the LGM, and we rely on the bedrock ^{14}C ages to constrain the maximum ice thickness.

2.3.3 *Chronology of glacial deposits*

2.3.3.1 Dubris and Bibra Valleys

We dated the Britannia II deposit using surface exposure ages of nine glacial erratics sampled from the drift limit Figure 2-2). We found no algae within the Britannia II deposit, except that of former ponds that fringed the Britannia I limit. Our exposure age chronology supports the conclusion of Joy et al. (2014) that the Britannia II deposit is a product of the penultimate glaciation. While Joy et al. gave a mean ^{10}Be age of 126 ± 3.2 kyr BP (n = 5), we find an ^{26}Al age of 136 ± 3 kyr (n = 9; reduced $\chi^2 = 1.35$) (Figure 2-3). Recalculation of Joy et al.'s ages using an updated value of the ^{10}Be production rate yields an age of 138 ± 4 kyr, in close agreement with our ^{26}Al age. Our initial attempt to date the Britannia II limit using ^{10}Be resulted in a widely spread dataset. Although the weighted mean age of 137 kyr agrees with the ^{26}Al ages, these data scatter far beyond their uncertainties ($\sigma = 18$ kyr, $\chi^2/(n-1) = 57.9$). Standard cathodes analyzed in the same accelerator as these samples also scattered widely, leading us to distrust ^{10}Be data from this run. We thus rely of the ^{26}Al data and assign an age of 136 ± 3 kyr BP to this deposit.

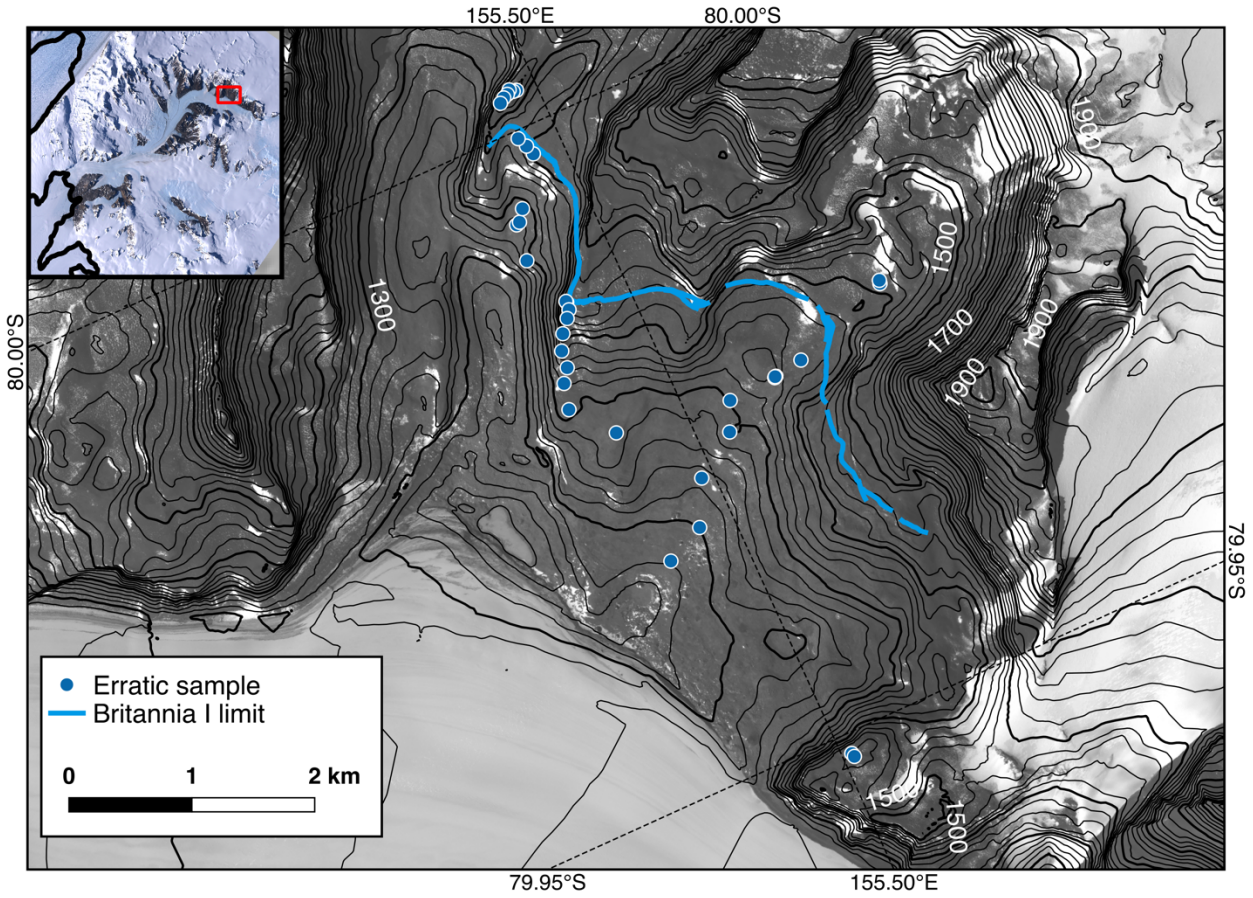

Figure 2-2: Simplified map of Dubris and Bibra Valleys, showing sample locations and elevations shown in 20m contours (100 m contours are in bold). The blue curve represents the Britannia I limit; erratic samples outboard of that limit are taken from the limit of the older Britannia II deposit. Contours and satellite imagery from Land Information New Zealand.

The Britannia I limit across Dubris and Bibra Valleys represents at least 370 m of thickening relative to the present glacier, and dates to 8-10 kyr BP (Figure 2-4). Slight variations in the age of the Britannia I limit between different sites is to be expected, as changes in local meteorology could allow small-scale fluctuations of the ice margin. After 8 kyr BP, the glacier margin began

to retreat steadily towards its present position.

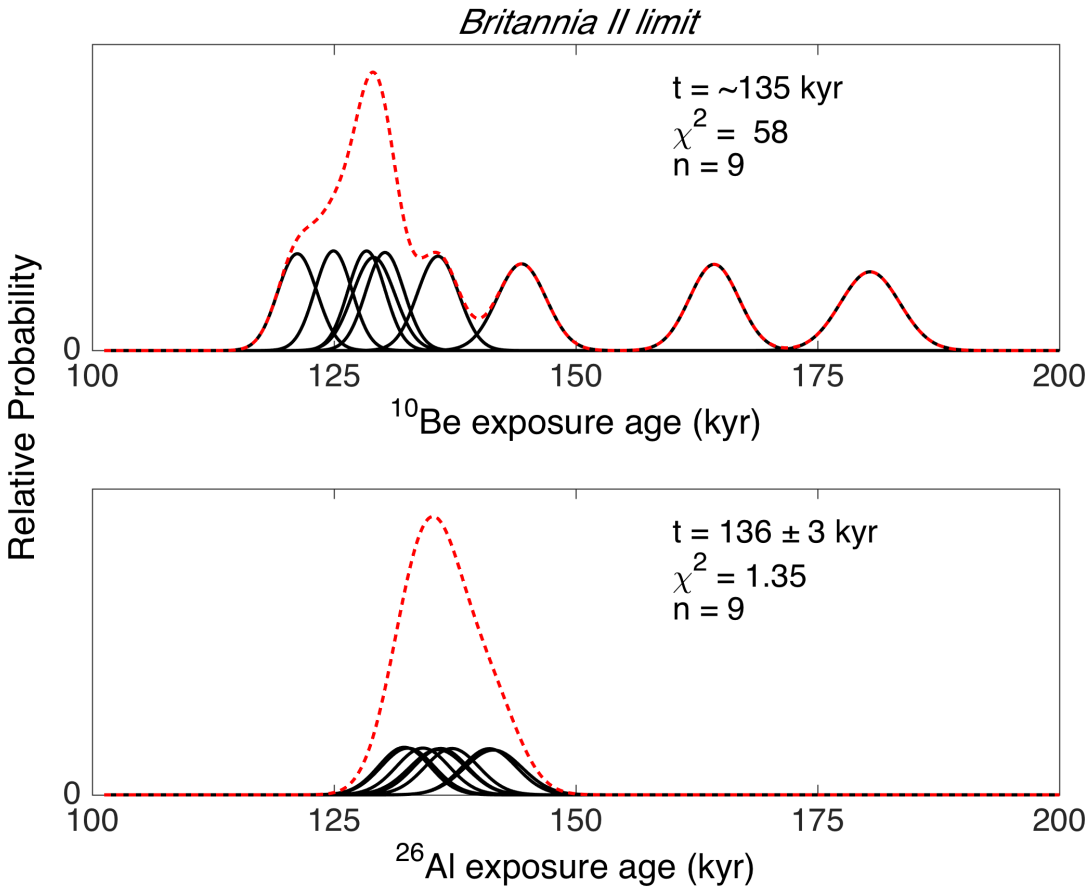

Figure 2-3: Surface exposure ages of erratics in the Britannia II deposit. Black curves are individual ages; red dashed curves are summed probabilities. While our ^{10}Be ages failed to tightly constrain the age of the deposit, ^{26}Al ages cluster tightly around 136 kyr BP, in good agreement with the results of Joy et al. (2014).

Only one exposure age exhibits significant prior exposure to cosmic rays (13-HAT-133-BV; 79 kyr). This sample was the closest to the glacier margin, and thus prevents us from better constraining the last 150 m of glacier thinning using exposure dating.

2.3.3.2 Magnis Valley

The Britannia I limit in Magnis Valley (Figure 2-5) predates the limit at Dubris and Bibra Valleys, with ages spanning 7.8 – 13.9 kyr on the valley walls, and 8.3 – 12.4 kyr on the valley floor (Figure 2-6). A single pre-exposed sample at the drift limit dates to ~32 kyr BP. Two erratics from a recessional deposit on the upglacier valley wall record 120 m of glacier thinning by 5.8 kyr BP. Erratics on the valley floor largely agree with this history, showing 100 m of thinning by 6.1 kyr BP. Two of the erratics in the recessional transect have evidently had prior exposure to cosmic rays.

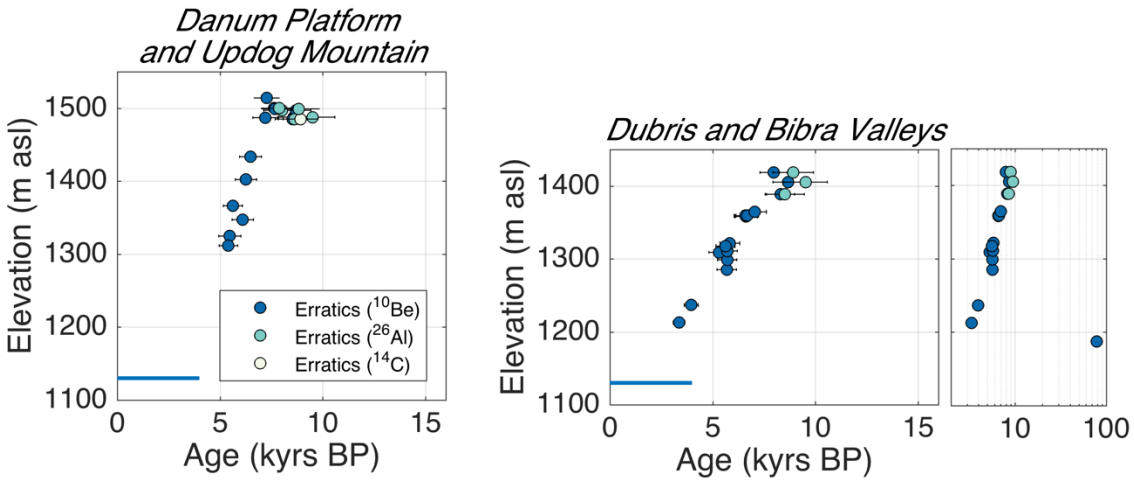

Figure 2-4: Surface exposure ages of glacial erratics from atop bedrock platforms (left panel) and Dubris and Bibra Valleys (middle and right panels), showing a stable margin until 7-8 kyr BP, after which the glacier thinned steadily towards its modern configuration. The rightmost panel shows all surface exposure ages of the Britannia I deposit in Dubris and Bibra Valleys on a logarithmic scale to include samples with significant inherited nuclides.

The algae radiocarbon chronology at Magnis Valley show a poor relationship between age and elevation, with ages adjacent to the modern glacier spanning 1.6 – 8.4 kyr. A cluster of algae samples from the Britannia I limit date to ~8 kyr BP, but ages of samples from the recessional deposit mostly lie between 7.3 and 8.5 kyr BP. Algae samples dating to 10,500 – 13,100 kyr BP

at ~1130 m elevation could conceivably be from the glacier advance, but this is unlikely because they lie within the age range of the LGM limit from the glacial erratics. Based on the lack of internal consistency in the radiocarbon dataset here, and on the lack of exposure ages of erratics close to the ice margin, we are unable to date the time at which the glacier margin stabilized at its present position in Magnis Valley. However, if thinning continued at the same rate of ~5 cm/yr, the glacier would have established its modern margin position ~2 kyr BP, which is in agreement with the time at which the glacier margin stabilized at Lake Wellman.

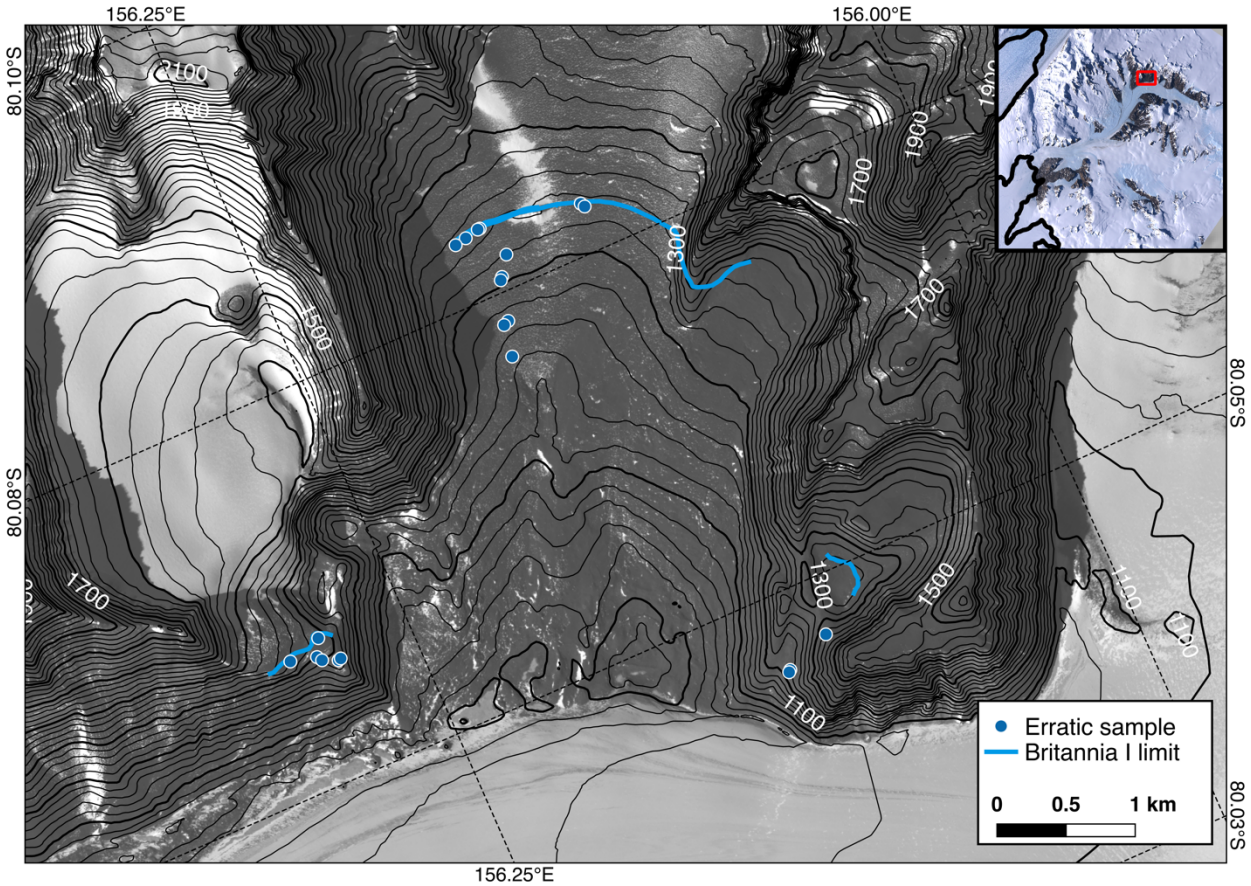

Figure 2-5: Simplified map and sample locations at Magnis Valley. Blue curves indicated the mapped Britannia I (LGM) limit. Ages corresponding to these samples are shown in Figure 2-6.

2.3.3.3 Lake Wellman

Our exposure age chronology at Lake Wellman suffers from numerous pre-exposed erratics, resulting in a wide spread of ages (Figure 2-7; Figure 2-8). However, radiocarbon ages of algae from lakes and ponds show a strong dependence of age on elevation, with a stable maximum position from 13 kyr BP until ~8 kyr BP, followed by steady thinning to modern elevations by the late Holocene. Bockheim et al. (1989) and Storey et al. (2010) were not able to differentiate between the Britannia I and II drifts at Lake Wellman, but King et al. (2017) mapped the Britannia II limit slightly outboard of the Britannia I limit. There were no algae present in the Britannia II drift, and we did not sample it for surface exposure dating.

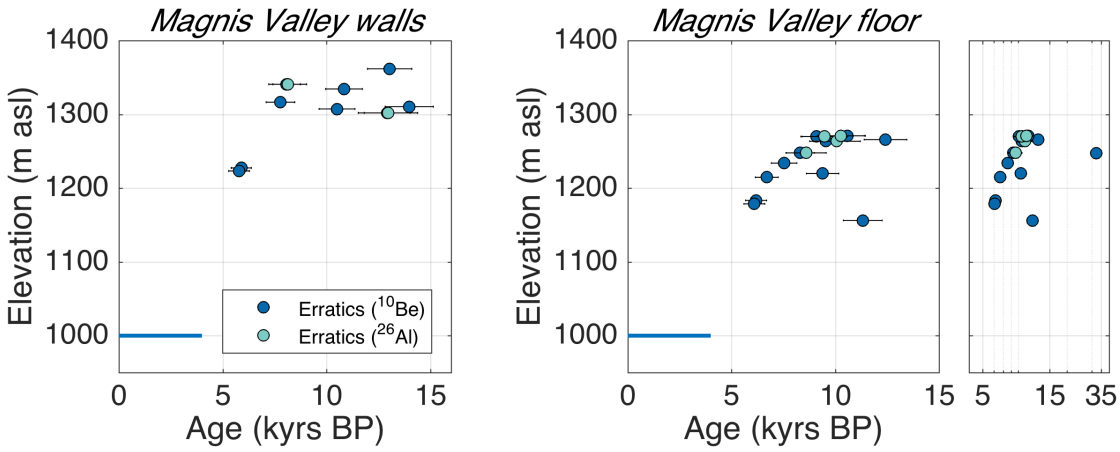

Figure 2-6: Magnis Valley exposure ages. Hatherton Glacier reached its limit in Magnis Valley ~13 kyr BP, and began to retreat 7-8 kyr BP.

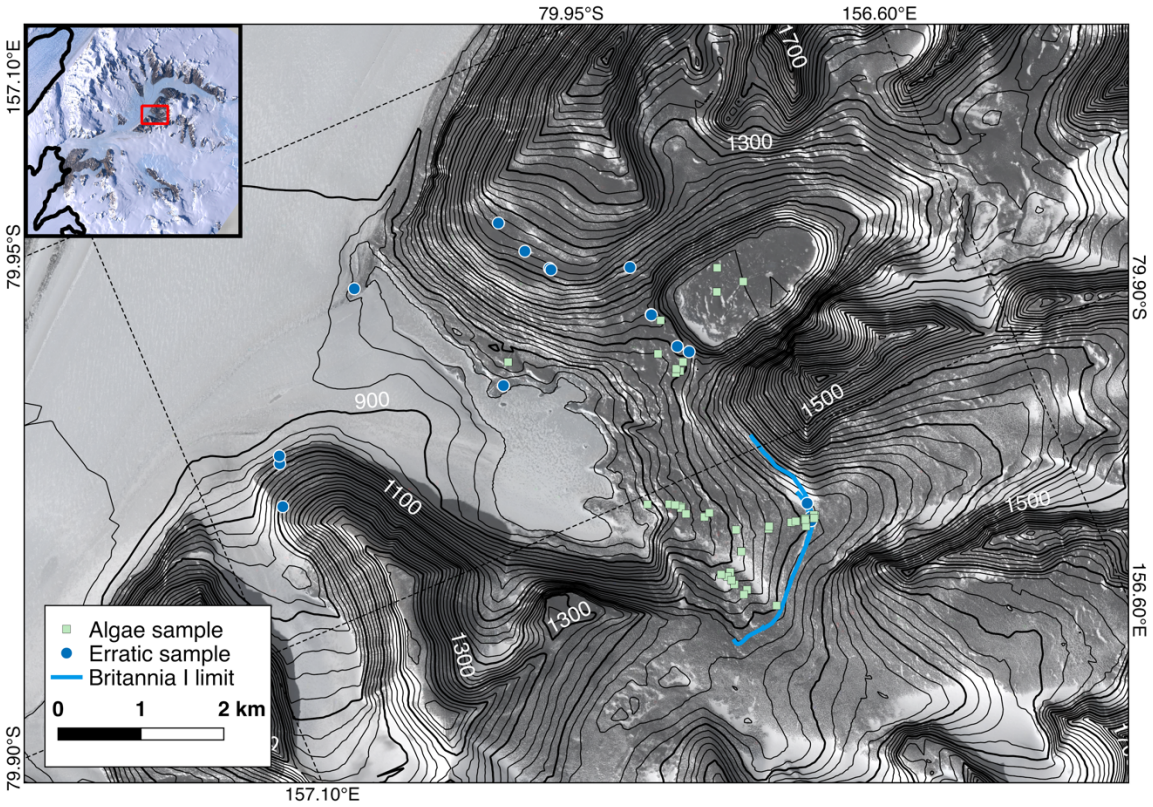

Figure 2-7: Simplified map of Lake Wellman and sample locations. Radiocarbon samples are from King (2017).

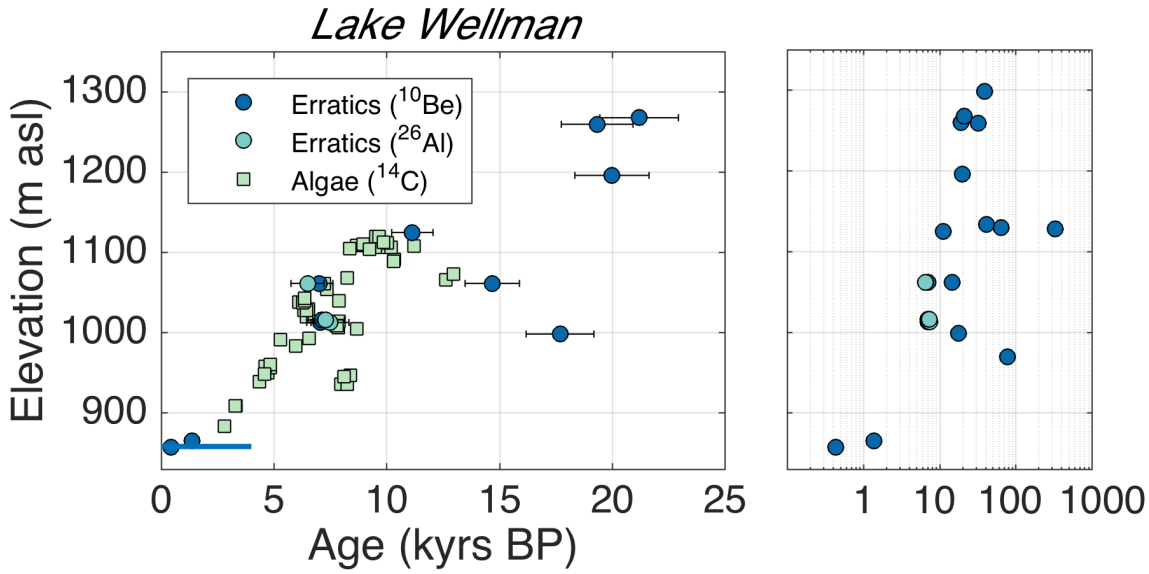

Figure 2-8: Surface exposure ages from Lake Wellman, with algae radiocarbon ages from King (2017). While the algae dataset tightly constrains the fluctuations of Hatherton Glacier, many of the surface exposure ages indicate prior exposure to cosmic rays. Although all samples were from the Britannia I or Hatherton drifts there is only a weak correlation between age and elevation. The righthand panel shows all exposure ages on a logarithmic scale, in order to include all outliers.

2.3.3.4 Brown Hills

The Brown Hills lie adjacent to Diamond Glacier—a distributary lobe of Darwin Glacier—and to the Ross Ice Shelf (Figure 2-9). During glacial periods, Diamond Glacier would very likely have crossed the Brown Hills and connected with the Ross Ice Sheet. However, because the ice-free topography here is several hundred meters above sea level, the ice would have been thin and very quickly cut off from the thick ice sheet during retreat. Therefore, we expect ages from recessional deposits in the Brown Hills to predate the chronologies of Hatherton or Darwin Glaciers.

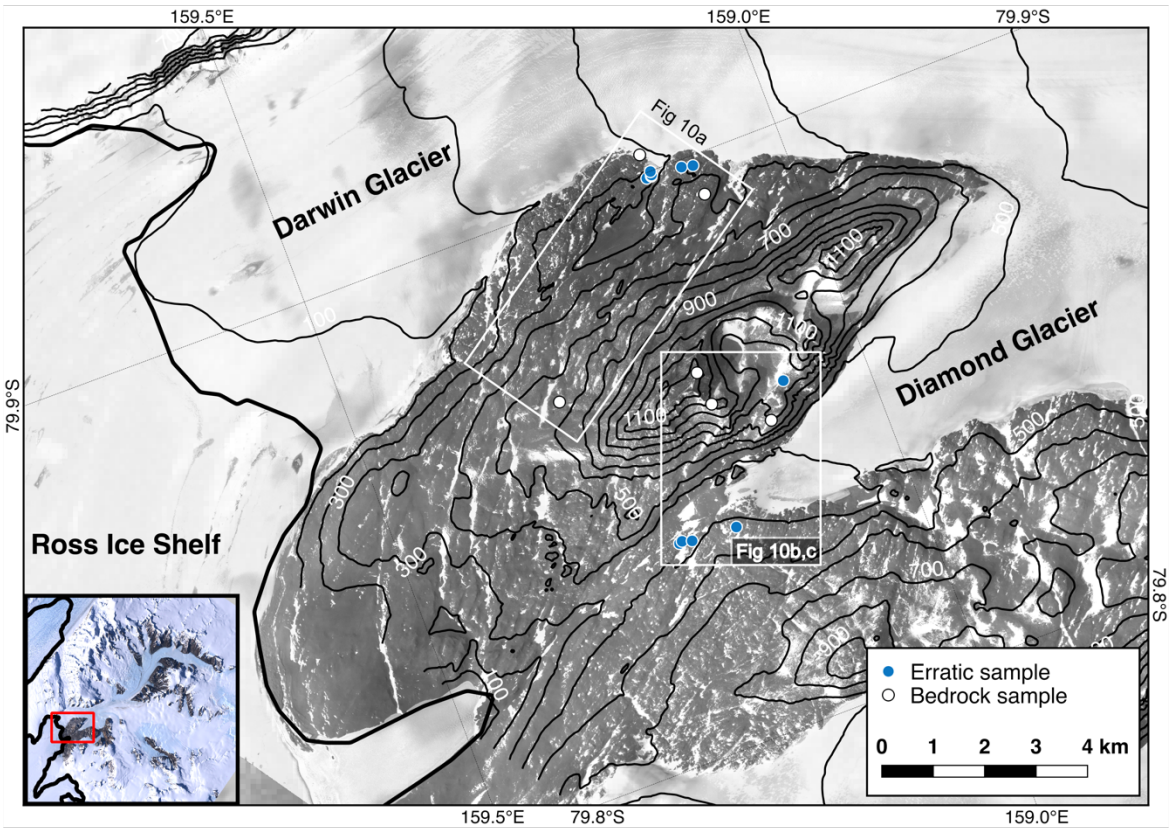

Figure 2-9: Map of Diamond Hill with bedrock and erratics sample locations. The modern grounding-line is shown as bold black line. Boxes indicate how samples are grouped into the panels of Figure 2-10.

We dated five erratics from the Brown Hills, including the Diamond Glacier side of Diamond Hill (Figure 2-10). The highest of these samples was a fresh-looking granite cobble taken from a weathered deposit high on Diamond Hill (877 m asl). While it was unweathered compared with the pre-LGM deposit it was perched on, it yielded a ^{10}Be age of 205 ± 5 kyr, and thus it is either (i) recently exhumed from the older deposit, or (ii) a deposit of the last glaciation, with a high level of inherited ^{10}Be. A single date from this deposit is not a good age constraint; however,

based on the weathering characteristics of the pre-LGM deposit on which the rock sits, we conclude that thick ice covered much of Diamond Hill at least once in the Pleistocene. We did not find deposits of the last glaciation high on Diamond Hill.

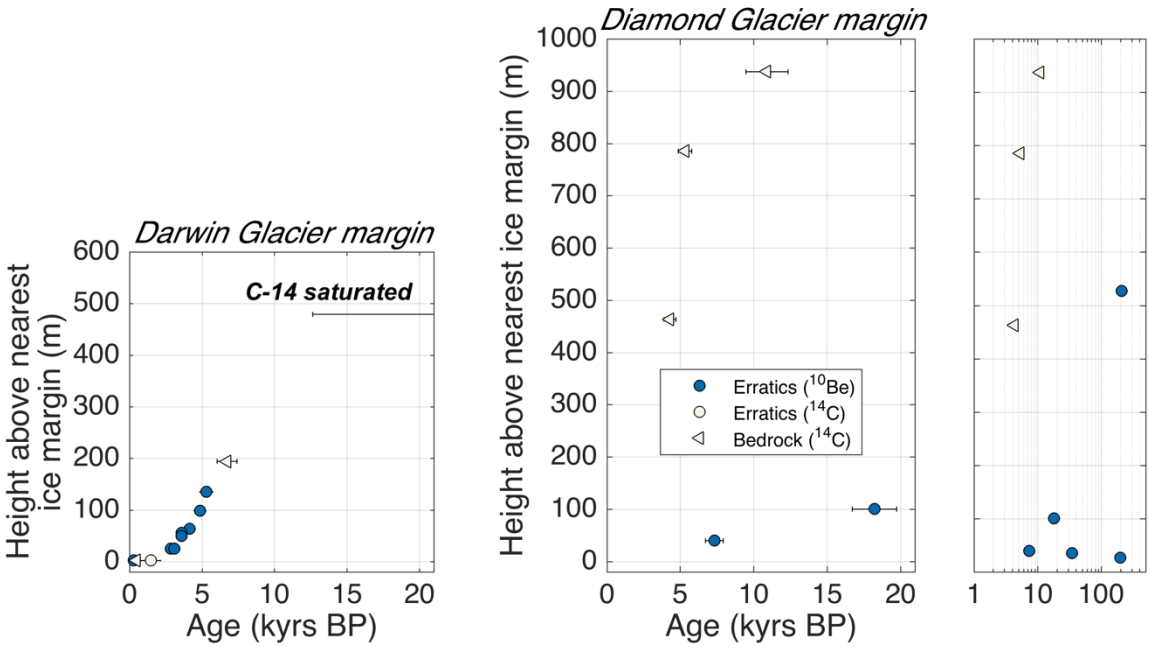

Figure 2-10: Diamond Hill chronology from ^{10}Be and ^{14}C exposure dating. Bedrock ^{14}C ages give a maximum time of last exposure because inherited ^{14}C from exposure before the LGM cannot be quantified. The top of Diamond Hill, >900 m above the modern glacier surface, was covered by ice during the LGM, and was exposed sometime between 11 and 5 kyr BP. However, the ^{14}C-saturated sample ~500 m above the modern glacier shows that the ice surface geometry at the LGM was ≥450 m lower on the down-glacier side of Diamond Hill. Therefore, it is not straightforward to interpret these chronologies without a glacier flow model. This is addressed in Section 3.

The exposure ages of erratics from the Brown Hills also provide only circumstantial constraints on the last glacial advance. One rock was heavily pitted and stained and yielded a ^{10}Be age of 196 ± 5 kyr. Of the remaining three, only one gave a Holocene exposure age (7.1 ± 0.2 kyr; 390 m asl). The other two dated to 33.7 ± 0.9 kyr (385 m asl) and 17.8 ± 0.4 kyr (450 m asl). This

dataset shows no dependence on elevation or distance from the current glacier margin, likely because of inherited ^{10}Be or local scale fluctuations not controlled by regional ice dynamics or climate. However, this does show that ice had retreated from the Brown Hills, and therefore had disconnected from the Ross Ice Shelf/Sheet ≤7 kyr BP.

2.3.3.5 Diamond Hill

The only relatively fresh, unweathered erratics on Diamond Hill were perched on glacially sculpted bedrock domes overlooking Darwin Glacier, ~10 km upglacier from the modern grounding-line (Figure 2-9). There was no clear limit of deposition, but we did not find any geomorphically young erratics higher than 135 m above the modern glacier margin. We dated eight of these erratics (Figure 2-10), which have ^{10}Be ages spanning the latter half of the Holocene, from 5.2 ± 0.2 kyr BP 135 m above the current glacier margin, to 0.3 ± 0.03 kyr BP at the current glacier margin. The rate of thinning appears to have been relatively constant between 5.2 and 3.1 kyr BP, after which it slowed down.

The lack of deposits does not necessarily imply ice-free conditions at the LGM. The ice above this could have been cold-based and debris-free, and thus did not deposit erratics as it retreated from the side of Diamond Hill. The steep terrain and sizeable extent of Diamond Hill prevented us from sampling from all locations, but we did climb to the top of Diamond Hill on the northern (ice-shelf proximal) side, and descended on the western (Brown Hills proximal) side, and we did not find evidence of LGM deposits.

The apparent *in situ* ^{14}C exposure ages do not show a simple relationship between age and elevation (Figure 2-10). On the flank of Diamond Hill nearest Darwin Glacier, our highest bedrock sample (14-HAT-026-DH; 472 masl) gives an apparent exposure age of 6.7 ± 0.7 kyr BP, 200 m

above the modern glacier margin. Bedrock sampled <2 m above the current ice margin (14-HAT-033-DH; 280 masl), and adjacent to the 300-year-old erratic (14-HAT-032-DH) gives an apparent ^{14}C exposure age of 500 ± 200 years BP. These ages confirm and extend the thinning chronology given by the ^{10}Be exposure ages of the nearby erratics. The exposure ages in this transect are too young to record a large early-Holocene deglaciation event, as found at Beardmore and Mackay glaciers (Jones et al., 2015; Spector et al., 2017). However, those glaciers only thinned by tens of meters following a large drawdown of several hundred meters in the early Holocene, whereas Darwin Glacier thinned by 200 m since 6.7 kyr BP. This could be a function of the ice sheet bed topography near the mouths of these glaciers, which is currently poorly known.

About 500m above the glacier margin on the ice shelf side of Diamond Hill, the bedrock is at or near the saturation with respect to ^{14}C (14-HAT-006-DH; 593 masl). This sample was either not covered by ice during the last glaciation, or covered for only a brief period (< 1kyr). The maximum ice thickness at other locations in the Ross Sea lasted for 3-5 kyr (Todd et al., 2010; Hall et al., 2010; Spector et al., 2017), so we take this sample to be an upper bound on the LGM ice surface elevation near the modern grounding-line. This is a surprising result, given that the LGM ice surface at the mouths of other TAM outlet glaciers was often ~700-900 m above the modern ice surface (Todd et al., 2010; Bromley et al., 2010, 2012; Spector et al., 2017). It is especially at odds with both Bockheim et al.'s (1989) estimate of an LGM ice surface 1000 m above present at the mouth of Darwin Glacier, and with Storey et al.'s (2010) assertion that Darwin Glacier did not thicken during the LGM. Anderson et al.'s (2004) estimate of an LGM ice surface 800 m above the modern is closer to the truth, but still an overestimate.

On the summit and opposite flank of Diamond Hill — above Diamond Glacier — *in situ* ^{14}C concentrations are well below saturation, decreasing with elevation from 10.8 ± 1.4 kyr at the

summit of Diamond Hill (1287 masl) to 5.3 ± 0.5 kyr at 1134 masl and 4.3 ± 0.4 kyr at 813 masl. In contrast to the ages from the other side of Diamond Hill, these ages suggest that the summit was completely overtopped by ice for a long period during the last glaciation. Today, Diamond Glacier terminates in a bedrock saddle between Diamond Hill and the Brown Hills below these samples at ~350 masl. While Darwin Glacier had thinned to within 135 m of its modern thickness by ~5.1 kyr BP, these ages may suggest that Diamond Glacier was still at least 785 m thicker than present at this time. The ice covering these samples could also have been part of a separate alpine glacier; however, we found no geomorphological evidence that ice has recently occupied this cirque, and most alpine glaciers in the Ross Sea region retreated during the last glaciation due to decreased precipitation (Denton et al., 1989; Higgins et al., 2000; Jackson et al., 2017). Furthermore, the apparent exposure ages increase with increasing elevation, which is the opposite of what would be expected from a mountain glacier retreating due to an increase in the equilibrium line altitude. The most likely explanation is that glacier ice covered the summit and upglacier flank of Diamond Hill, but did not flow entirely over it. Instead, Diamond Hill was most likely a nunatak at the LGM, with the downglacier flank exposed much like the modern ice configuration of the nearby Roadend Nunatak.

We analyzed cosmogenic ^{26}Al and ^{10}Be in the same bedrock samples in which we measured *in-situ* ^{14}C in order to compare recent glacial fluctuations to the long-term history of glacial-interglacial changes (Figure 2-11). The ^{26}Al and ^{10}Be concentrations of the bedrock transect supports our interpretation from *in-situ* ^{14}C that in general, ice covered the upglacier side of Diamond Hill but not the lee side. The two highest elevation samples (14-HAT-035-DH, 1135 masl; 14-HAT-036-DH, 1297 masl) have only very rarely been covered by ice or snow. The ^{14}C-saturated sample (14-HAT-006-DH; 598 masl) is buried less frequently than the sample above it

in the elevation transect (14-HAT-039-DH; 813 masl), which precludes interpretation by a simple ice sheet thickening and thinning scenario. The lowest elevation sample (14-HAT-033-DH; 280 masl) exhibits clear geomorphic signs of glacial erosion and has thus lost much of its inherited nuclide inventory, making it difficult to interpret in terms of burial and exposure durations. However, it yields apparent ^{10}Be and ^{26}Al exposure ages of 15.8 ± 1.3 kyr and 13.9 ± 1.5 kyr, respectively. Compared to its ^{14}C age of 480 ± 200 yr, this indicates that glacial erosion over the last glacial cycle was insufficient to remove evidence of prior exposure.

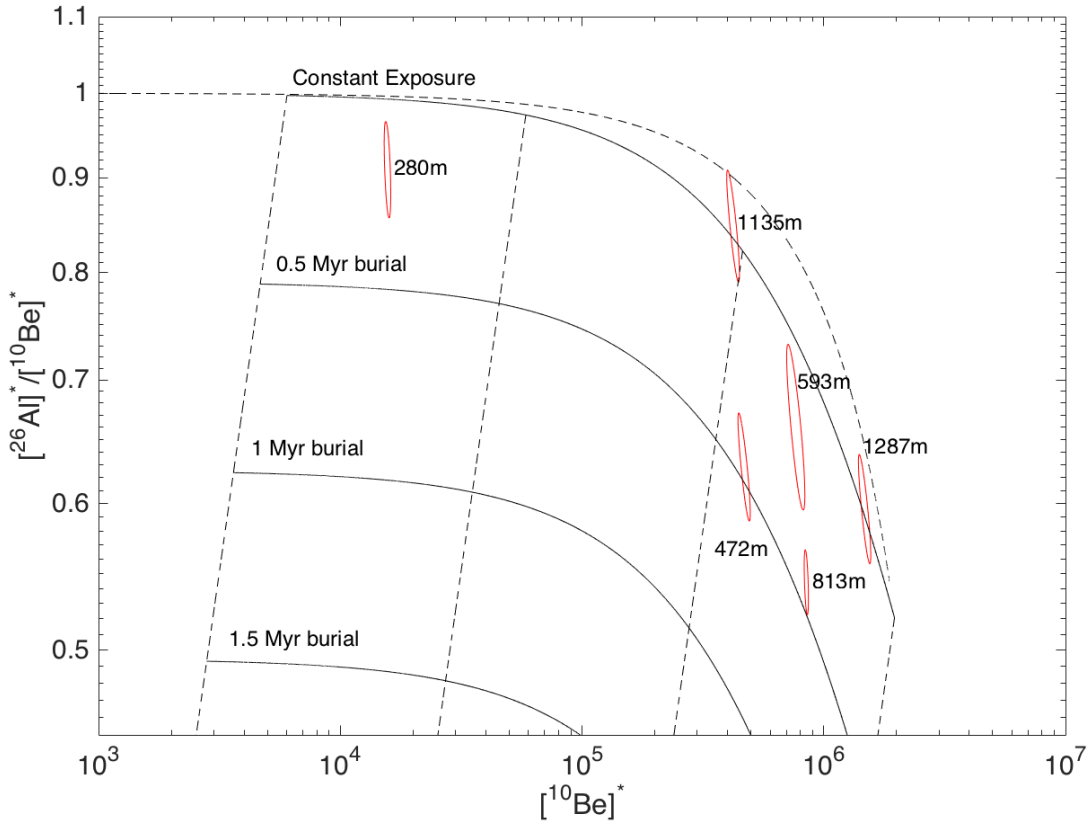

Figure 2-11: Long-term exposure-burial history from ^{26}Al and ^{10}Be measurements of Diamond Hill bedrock. Sample elevation is listed by each measurement ellipse. ^{26}Al and ^{10}Be concentrations have been normalized to the local production rate, which allows us to portray samples from different elevations on the same axes. These measurements show both that the two highest elevation samples (14-HAT-035-DH: 1135 m, and 14-HAT-036-DH: 1287 m) have experienced almost no burial by ice, while all the lower elevation samples have considerable burial signals. Sample 14-HAT-006-DH (593 m) also stands out as having been buried less often than samples both higher and lower in elevation (14-HAT-039-DH: 813 m; 14-HAT-026-DH: 472 m, respectively). Therefore, while unsaturated ^{14}C concentrations in bedrock at the top of Diamond Hill show that the LGM was an uncommonly large glaciation, the ^{14}C-saturated bedrock sample at 593 m elevation reveals that the downglacier side of Diamond Hill is rarely ice-covered. The surprisingly low burial age of the lowest elevation sample (280 m) could be due to erosion prior to the timescale recorded by ^{26}Al, resulting in a higher-than-expected isotope ratio.

Comparison with the *in situ* ^{14}C measurements on the same bedrock samples shows that the mouth of Darwin Glacier was thicker at the LGM than is typical for prior glaciations. The young exposure ages from high on Diamond Hill indicate a significant period of ice cover during the last glaciation, while the paired ^{10}Be and ^{26}Al analyses suggest that ice cover on the summit is a rare occurrence on 100 kyr to Myr timescales. This is consistent with the Britannia II, Danum, and Isca deposits from Hatherton Glacier, which show that older glaciations were larger than the last glaciation (Bockheim et al., 1989; Joy et al., 2014). This could simply reflect different controlling mechanisms on ice thickness during different glaciations (e.g., increased accumulation over the TAM or EAIS vs. thickened ice in the Ross Embayment). Alternatively, long-term shrinkage of the Darwin and Hatherton catchments may have occurred when the Byrd and/or Mulock catchments grew because of their greater efficiency transporting East Antarctic ice (cf. modeling results of Arctic fjord development over Myr timescales; Kessler et al., 2008). This hypothesis is consistent with the observations of pre-LGM (but undated) striations in bedrock near the head of Hatherton Glacier that indicate ice flow into the Hatherton catchment from what is currently the catchment of Byrd Glacier (Bockheim et al., 1989). While future data collection and modeling could shed light on this observation, we currently do not have sufficient data to test this hypothesis.

The fact that the ^{14}C-saturated sample (14-HAT-006-DH; 598 masl) has been buried by ice less frequently that the sample above it (14-HAT-039-DH; 813 masl) supports our interpretation that samples from high on Diamond Hill (>800 masl) are less representative of the fluctuations of the Ross Sea Ice Sheet than the lower-elevation samples. This is likely a result of which side of the mountain the samples were taken from; however, we cannot prove this assertion due to the small number of samples. Ice flowing to the northwest (Diamond Glacier) side of Diamond Hill

during glacial periods was likely fed by ice flowing over Bastion Bluff. Diamond Glacier would have thinned rapidly once this connection was cut off, while Darwin Glacier remained thick.

2.4 NUMERICAL MODELING OF GLACIER FLUCTUATIONS

2.4.1 *Model description*

We use two numerical models to evaluate possible deglaciation scenarios consistent with our geochronological data. We model Darwin and Hatherton Glaciers since the LGM using a 1.5-D shallow ice glacier flow-band model, which solves mass conservation to calculate ice-surface evolution using the finite volume method of Patankar (1980). This model is computationally inexpensive and has the added advantage of a reduced number of otherwise poorly constrained ice-flow parameters and boundary conditions. The model domain starts near Diamond Hill at 10 km upstream from the modern grounding-line where we have geochronological data. We do not model grounding-line evolution, but we are able to use geochronological data to prescribe surface-elevation change at a location that is always upstream of the grounding line over the past 20 kyr.

Ice flow in one dimension is described by the time-evolving mass conversation equation (Cuffey and Paterson, 2010):

$$\frac{\partial H(x)}{\partial t} = -\frac{1}{W(x)}\left(\frac{\partial q(x)}{\partial x}\right) + \dot{b}(x) \tag{2.1}$$

where H(x) is the ice thickness, q(x) is the volumetric ice flux, W(x) is the glacier width, and $\dot{b}(x)$ is the surface mass balance. The total ice velocity (U)is the sum of contributions from internal deformation (U_d) and basal sliding (U_s) taken to be of this form:

$$U = U_d + U_S = f_d H \tau_d^n + f_s \frac{\tau_b^m}{H} \tag{2.2}$$

where f_d is the deformation factor, f_s is the sliding factor, n=3 is the flow-law exponent, $1/3 \leq m \leq 4$ is the sliding exponent, τ_d is the driving stress, and τ_b is the basal shear stress. Cross-sectional area is accounted for at each grid point, and the flux is scaled accordingly compared to a simple rectangle of area HW. The flux of small tributary glaciers contributing to Darwin and Hatherton Glaciers are estimated using a flux gate calculation and we make the assumption that tributary flux contributions are constant through time.

2.4.2 *Model parameters, tuning, and boundary conditions*

Surface mass balance and basal conditions of Darwin and Hatherton glaciers are poorly known. We use the RACMO2.1 5.5-km resolution model of the modern surface mass balance (Lenaerts et al., 2012), as this is the only data product to include the significant surface ablation that is observed. While these ablation areas are not in the same locations observed from satellite imagery, we argue that this is the best choice of surface mass balance because it matches reasonably well the overall flux out of the glacier system (Gillespie et al., 2017). Furthermore, the model is a function of the integral of the surface mass balance and not the specific pattern of accumulation and ablation at any given location.

We tune a steady-state version of the flowband model to estimate poorly constrained ice-flow parameter values by minimizing the mismatch between the modeled and observed modern glacier surface elevation and the modern surface velocity at each model grid point; this is a strategy

applied in related problems (e.g., Golledge et al., 2014). We vary the basal sliding factor (f_s) and the ice-flow deformation factor (f_d) defined at each model grid point within a plausible range of values. The deformation factor and basal sliding parameter vary spatially over the model grid but we assume that the spatial patterns that optimize the fit to modern data do not change over the past 20 kyr; this is an assumption, but there is no information available to constrain a different choice of parameter values in the past. In general, we have limited information available to constrain the values of the sliding and deformation factors, and while our inferred patterns of these parameters generate a surface-elevation profile and surface-velocity profile that match modern values within their uncertainties, it is likely that it is not a unique solution. However, we are using this simple model to constrain the time evolution of the glacier system that is consistent with our geochronological observations, and not to interpret inferred values and patters of controls on ice flow.

The downstream boundary condition for Darwin Glacier is a prescribed surface elevation through time based on our glacial geologic data. The surface elevation at the most downstream grid point of the major tributary Hatherton Glacier is prescribed at each timestep by the value at the adjacent node along the Darwin Glacier flowline where the glaciers intersect. The flux from Hatherton Glacier is added to Darwin Glacier at that node, the surface of Darwin Glacier is recalculated, and the surface elevation at the mouth of Hatherton Glacier is reset to match the updated surface of Darwin Glacier. While the model domains are set up to contain the modern drainages of Darwin and Hatherton Glaciers, these catchment boundaries may have changed in the past. Thus, we evaluate the influence of time-varying flux that enters the domain from the upstream boundary, as required by a flux-balance calculation. We are also able to modulate flux entering the

glacier through the upstream boundary as a way of investigating the role of catchment geometry changes (including ice divide migration) on the evolution of the glacier profiles.

2.4.3 *Model evaluation*

In order to score the model output against our chronologies from each location, we must account for the fact that our geochronology data record the elevation of the glacier margin through time, rather than the glacier centerline that is calculated in the flowband model. Thus, the exposure and radiocarbon ages represent a minimum elevation for the glacier centerline through time. While the glacier centerline generally lies 100 m above its margin today, this would not necessarily have been the case at the LGM. We can determine the possible range of glacier centerline elevations at the LGM by calculating a linear best-fit curve to the LGM deposits in the valley floor (far from the modern glacier) and on the valley walls (close to the modern glacier). By extrapolating this linear fit out to the center of the glacier, we obtain a maximum constraint on the LGM glacier centerline elevation because the glacier should not have a concave-up profile in the transverse direction. We use the elevation of the highest LGM erratics as a minimum constraint for the same reason. In the absence of further constraints, we use the mean of these elevations as the estimated LGM centerline elevation, and the span as the 2-sigma uncertainty. Because the age of the LGM deposit on the valley walls does not necessarily match the age of the corresponding limit on the valley floor, these are slightly time-transgressive estimates. However, we consider this the best estimate possible without the use of a higher-dimensional glacier model that requires additional assumptions. We obtain glacier centerline elevations and 2-sigma uncertainties of 1355 ± 67 m at Lake Wellman, 1402 ± 56 m at Magnis Valley, and 1550 ± 45 m at Dubris-Bibra Valleys.

At Diamond Hill, we lack the clear limit LGM deposits necessary to project samples to a glacier centerline elevation. Instead, we convert the elevations of algae, bedrock, and glacial erratics samples to a height above the nearest ice margin and use that value as constraints for glacier fluctuations and for the experiments discussed in Section 3.4. Likewise, we do not have a reliable means of assigning uncertainty to these elevations, and so we take a conservative approach and ascribe a ± 75 m 2-sigma uncertainty. Each data-point represents a strict minimum elevation for the glacier centerline at the given age, and the surface profile of the lobe entering the valley is unknown. Therefore, we convert the age-elevation transects to a percentage of the total LGM-to-present change. We can then relate the LGM-to-present change to the glacier centerline elevation using the estimate of LGM elevation described above and the measured modern surface elevation.

2.4.4 *Transient experiments*

Our glacial geologic data are equivocal about the magnitude and rate of change from the LGM to present. Data from nearest Darwin Glacier suggest slow and steady thinning of 500 m through the Holocene, while data at the summit of Diamond Hill suggest a ~900 m of rapid thinning ~ 7 kyr BP. We used our glacier flowband model to test how these deglaciation scenarios at the mouth of Darwin Glacier would be reflected in the chronologies from Hatherton Glacier. We also test the alternative hypothesis that 500 m of LGM-to-present thinning comprised a rapid drawdown of 200 m in the early Holocene, consistent with records from other TAM outlet glaciers (Spector et al., 2017), followed by flow and steady thinning recorded in the ages of the erratics. The simulations presented here are tabulated in Table 2-1.

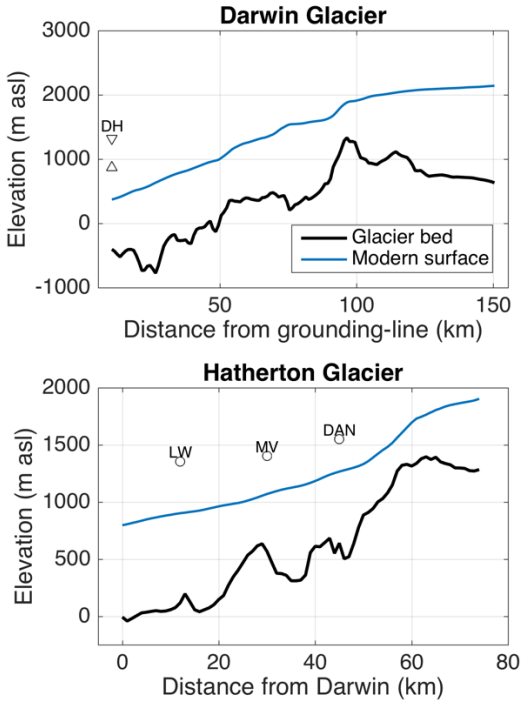

Figure 2-12: Modern bed and surface topography along the centerlines of Darwin and Hatherton Glaciers from Gillespie et al. (2017). Mapping and sample locations and our inferred LGM glacier surface elevation are denoted by circles for Hatherton Glacier (LW – Lake Wellman; MV – Magnis Valley; DAN – Danum Platorm). The triangles above the mouth of Darwin Glacier represent the two possible constraints at Diamond Hill (DH).

Experiment 1: 500-m of gradual thinning at glacier mouth

Modern surface mass balance, constant catchment size

Since we have no constraint on changes in accumulation and ablation patterns through time for the Darwin-Hatherton Glacier System, we first set up a transient run in which the modern surface mass balance pattern is kept constant in time. The glacier surface at the outlet of Darwin Glacier is held at 500 m above the modern surface until 9 kyr BP, and then lowered according to the geochronologic constraints from Diamond Hill (Figure 2-10), using the assumption that the ^{14}C-saturated bedrock sample represents an upper bound on the LGM ice surface of the main trunk of Darwin Glacier. This is based on the interpretation that the Holocene ^{14}C exposure ages higher up

on Diamond Hill represent cover by an ice cap or glacier that drained off of Diamond Hill to feed into the main trunk glacier (see Section 2.3). The results of this experiment are shown in Figure 2-13 (DH_run_1a).

Table 2-1: Inputs for flowband model runs

	Modern SMB	LGM SMB	External Flux Darwin (m^3/yr)	External Flux Hatherton (m^3/yr)
DH_run_1a	RACMO2.1	RACMO2.1	0	0
DH_run_1b	RACMO2.1	60% RACMO2.3	0	0
DH_run_1c	RACMO2.1	RACMO2.3	0	0
DH_run_1d	RACMO2.1	200% RACMO2.3	0	0
DH_run_1l	RACMO2.1	60% RACMO2.3	1.2×10^8	6.4×10^7
DH_run_2a	RACMO2.1	RACMO2.1	0	0
DH_run_2b	RACMO2.1	60% RACMO2.3	0	0
DH_run_2c	RACMO2.1	RACMO2.3	0	0
DH_run_2d	RACMO2.1	200% RACMO2.3	0	0
DH_run_2l	RACMO2.1	60% RACMO2.3	1.2×10^8	6.4×10^7
DH_run_3a	RACMO2.1	RACMO2.1	0	0
DH_run_3c	RACMO2.1	60% RACMO2.1	0	0
DH_run_3i	RACMO2.1	44% RACMO2.1 (scaled to Taylor Dome record)	-1.4×10^8	0

There is essentially no lag time between the application of the elevation-change at the mouth of Darwin and the response of Hatherton Glacier in this scenario. Thus, the onset of thinning at each location along the profile of Hatherton Glacier occurs almost simultaneously with the onset of thinning at Diamond Hill. This is consistent with our chronologies from the valleys alongside Hatherton Glacier, each of which indicates that retreat began ~8-9 kyr BP. However, using the modern surface mass balance at the LGM leads to a thinner modeled Hatherton Glacier than is indicated by the glacial deposits. This discrepancy gets more pronounced further upglacier: at Lake Wellman (close to the confluence of Darwin and Hatherton), the model predicts an LGM ice surface ~75 m below the LGM erratics at the entrance to the valley; at Magnis Valley, the model

underpredicts LGM thickness by ~100 m; at Dubris and Bibra Valleys, the modeled glacier is ~170 m too thin.

There are three possible explanations for the underprediction of LGM ice thickness in this experiment. First, it is possible that the current size of the glacier catchments is smaller than it was during the LGM. Observations of striated bedrock near the head of Hatherton Glacier indicate that at some unknown time in the past, ice likely flowed over into the Hatherton valley from what is now the catchment of Byrd Glacier (Bockheim et al., 1989). Likewise, there are no constraints on the former size of the Darwin Glacier catchment. It is thus entirely possible that at the LGM, more ice fed into the DHGS due to larger catchment size. Second, our assumption of a constant pattern of surface mass balance through time is too simple. The large ablation areas found on both glaciers today are near their likely maximum extent, and a small climate perturbation would decrease their size, leading to a more positive surface mass balance (Brown and Scambos, 2004). However, Hatherton Glacier must have had ablation areas (both wind scouring and surface melt) at its margins during the local LGM in order to provide the meltwater necessary to create the ponds that hosted our algae samples, and in order to deposit erratics in the valleys. Furthermore, accumulation rates tend to increase as the atmosphere warms during a glacial termination; the Taylor Dome ice core record shows a roughly 100% increase in accumulation rate between 12 kyr BP and 0.7 kyr BP (Monnin et al., 2004). The presence of blue ice areas due to scouring by katabatic winds would likely lead to a more complicated change in surface mass balance, but the reduction in snow accumulation during glacial periods would likely have been a common feature throughout the Transantarctic Mountains. Third, our records at the mouth of Darwin Glacier (Diamond Hill) are somewhat equivocal (Figure 2-10). The fact that the algae record at Diamond Hill seems to disagree with the record from glacial erratics, and that the complicated and spatially sparse bedrock ^{14}C

record is difficult to interpret leaves open the possibility that the average LGM ice thickness at Diamond Hill was higher than we have tentatively concluded (see Section 2.3.5). We explore the effects of time-evolving surface mass balance, variable flux into the glacier canyons, and different LGM ice thickness at the mouth of Darwin Glacier in the following model experiments.

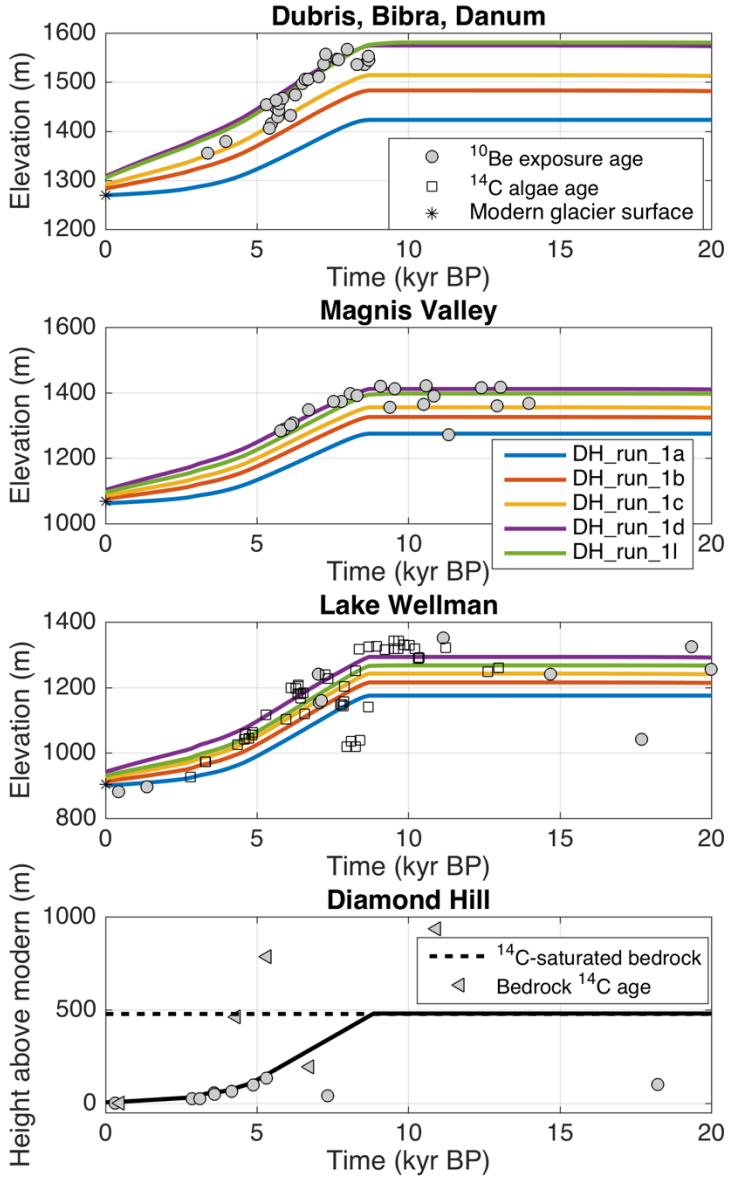

Figure 2-13: Flow-band model results from Experiment 1 (described in Section 3.4). The two best-fitting scenarios require either a larger catchment for both glaciers at the LGM (green curve; DH_run_1l), or an accumulation rate far higher than modern (purple curve; DH_run_1d). The black curve in the Diamond Hill panel represents the prescribed ice surface history at the downstream boundary.

Time-evolving surface mass balance

We first examined the effect of scaling the modern surface mass balance to the normalized accumulation rate history recorded in the Taylor Dome ice core (Steig et al., 2000; Monnin et al., 2004). As expected, this also leads to a modeled Hatherton Glacier that is too thin at the LGM, with 150-250 m of thickening relative to modern. This gives in a very poor fit to all of our glacial geologic data, and can is not a plausible history of the glacier system.

Next, we tried a simpler time-varying surface mass balance pattern in an attempt to determine the magnitude of glacial-interglacial change needed to match the records from Hatherton Glacier using only variations in SMB. The modern surface mass balance is taken from RACMO 2.3. We defined the LGM surface mass balance by multiplying a scaling factor by the RACMO 2.3 surface mass balance, which does not include ablation areas. We use values of 60%, 100%, and 200%. The choice of 60% is made to match the accumulation rate change in the Vostok ice core between the LGM and present (Petit et al., 1999). This is of course a crude estimation, but results in reasonable LGM accumulation rates of 2-10 cm/yr, with no blue ice areas. The surface mass balance is varied linearly in time between the modern and LGM states. After a 5 kyr spin-up to allow the model to equilibrate with LGM climate, the LGM SMB is held constant until 15 kyr, and then varied linearly to the modern SMB.

In this scenario, 60% scaling leads to underprediction of LGM ice thickness by about 100 m at all three Hatherton Glacier sites (DH_run_1b in Figure 2-13). Using a 200% scaling of modern SMB at the LGM leads to excellent agreement between the glacier model and most of the records from Hatherton Glacier (DH_run_1d in Figure 2-13). LGM surface elevations are matched to within

a few tens of meters at all three locations, the timing and rate of thinning agree very well, and the modern surface elevations are reproduced to within 40 m at all three locations.

While 200% scaling results in a reasonable match between the model and surface-exposure age data, it is an unlikely surface mass balance history. This requires LGM accumulation rates of 7-30 cm/yr, compared to ~3 cm/yr accumulation at Taylor Dome during the same time period. The fact that at least some surface ablation had to occur to create ice-marginal ponds means precipitation rates may have been even higher than this. This scenario also requires the overall surface mass balance to decrease during the termination of the glacial period, which is unlikely. Although this scenario fits our data quite well, we search for a more reasonable explanation.

Added flux to account for changing catchment area

As noted above, there are no constraints on the size of the glacier catchments at the LGM. While the modern glacier catchments are kept small by their proximity to Byrd and Mulock Glaciers, they could have been larger at the LGM. Due to the low surface slopes of the EAIS, just a moderate amount of thickening or thinning could drastically increase or decrease drainage area. To account for this uncertainty, we take the simple approach of adding ice flux to the upstream boundary of the Darwin and Hatherton Glacier model domains. A challenge of this approach is to define a time series of flux change across the upstream boundaries. Because this value would have varied in time and would not necessarily have been the same for both glaciers, any solution is likely to be non-unique. However, the goal of this exercise is not to calculate the magnitude of the flux entering the glaciers at the LGM, but rather to determine whether changing catchment areas could be a reasonable means of achieving the LGM ice thickness of Hatherton Glacier.

When additional flux is added only to Hatherton Glacier, the glacier profile tends to steepen, leading to overprediction of ice thickness by >100 m at Dubris-Bibra and Magnis valleys, while ice thickness is still ~75 m too low at Lake Wellman. Conversely, when a proportional amount of flux is added to the upstream boundary of the Darwin Glacier domain, LGM ice thickness is underpredicted at all locations on Hatherton Glacier by 75-100 m, while the head of Darwin Glacier is ~200 m thicker than Bockheim et al. (1989) found at Darwin Nunatak. However, by adding a more modest amount of flux to both Darwin and Hatherton Glaciers, and by using the scaled SMB of 60% modern for the LGM, we achieve a better fit to the LGM limits and retreat histories at all three locations along Hatherton Glacier, without unduly thickening the head of Darwin Glacier (DH_run_11 in Figure 2-13). Given the uncertainties in bed properties, accumulation rate, and tributary fluxes through time we consider this to be a satisfactory fit to the data. If the catchment boundaries stabilized before the grounding-line of Darwin Glacier stopped retreating, this could also explain the slowdown of thinning at Dubris-Bibra Valleys several kyr prior to the slowdown of thinning at Lake Wellman, ~30 km closer to the grounding-line.

We now consider whether the amount of additional incoming flux required to match the LGM limits is a physically reasonable quantity. For the additional 6.4 x 10^7 m^3/yr added to Hatherton and the additional 1.2 x 10^8 m^3/yr added to Darwin and a reasonable LGM accumulation rate of 3 cm/yr over the East Antarctic Plateau, this would require 2,100 km^2 and 4,100 km^2 of additional LGM catchment area for Hatherton and Darwin, respectively. This represents a ~75% increase over the modern catchment area (Gillespie et al., 2017), but only a 5% decrease in the Mulock Glacier catchment or a 0.5% decrease in the Byrd Glacier catchment areas based on the calculations in Stearns (2011). Because this total areal change is roughly equivalent to the reported uncertainty in the Mulock Glacier catchment area, and only about 11% of the uncertainty in the

Byrd Glacier catchment area, we consider this amount of divide migration over a glacial-interglacial cycle to be reasonable.

Experiment 2: Rapid early-Holocene thinning near grounding-line

The LGM limit inferred from ^{14}C-saturated bedrock and the 6.7 kyr-old bedrock exposure age below it are separated by 300 vertical meters. Other records from the western Ross Embayment show a rapid drawdown event 9-8 kyr BP, presumably indicating widespread deglaciation of the region in the early Holocene (Spector et al., 2017). There is no record of such abrupt thinning at sites upglacier, but such an event could have occurred in the data gap between the LGM and 6.7 kyr BP. We explore this possibility by imposing a rapid thinning event of 275 m from 9-8 kyr BP, followed by gradual thinning consistent with the glacial geologic constraints. Surface mass balance and additional flux are the same as the best-fit scenario from Experiment 1 (i.e., 75% larger catchment, SMB varies linearly through time). The results of this experiment are shown Figure 2-14.

The rapid thinning imposed at the mouth of Darwin Glacier propagates upglacier in the model with no significant lag. While the amplitude of the signal decays with distance upglacier, it is still readily detectable in the modeled glacier changes at Dubris-Bibra Valleys. This leads to a much poorer fit to the data than the situation with gradual thinning at the grounding line in Experiment 1. This shows that the records from Hatherton Glacier do not agree with a pulse of rapid thinning at the mouth of Darwin Glacier. This response is different compared to the rapid and dramatic records of thinning at the mouths of other TAM outlet glaciers (Todd et al., 2010; Jones et al., 2015; Spector et al., 2017) and supports our assertion that the DHGS did not respond to the last deglaciation in the same way as other outlet glaciers to the north and south.

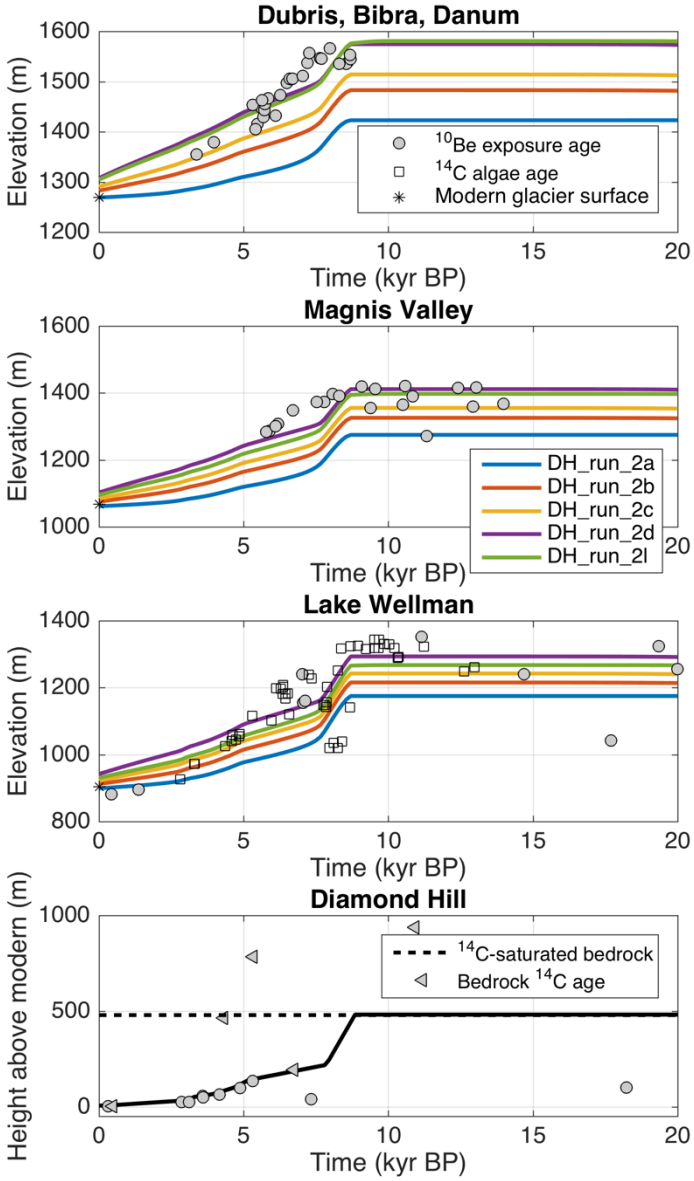

Figure 2-14: Flow-band model results for Experiment 2. All inputs are the same as for Experiment 1, except for the downstream boundary condition, which contains a period of rapid deglaciation 9-8 kyr BP. It is evident that this event would have been recorded in the deposits at Hatherton Glacier, but there is no clear evidence of this in our chronologies. Thus, the case of slow thinning in Experiment 1 provides a better fit to the data.

Experiment 3: 900-m of thinning near the grounding-line in the mid-Holocene

As shown in Figure 2-10, the bedrock high on Diamond Hill has Holocene exposure ages, while a ^{14}C-saturated sample lies hundreds of meters below. While we have argued that the higher-elevation ages are not as representative of the surface of Darwin Glacier as they are of more local ice configuration, we do not have enough data to prove this assertion outright (see Section 2.3.5 for a more thorough discussion). Thus, in this experiment we evaluate a scenario in which a very thick Darwin Glacier covered the top of Diamond Hill at the LGM, and then thinned by ~800 m from 6-4 kyr BP. This thinning history is defined by the bedrock samples in Figure 2-10b. Results are shown in Figure 2-15.

For modern accumulation rates and catchment boundaries, this deglaciation scenario leads to a modeled Hatherton Glacier that is ~160 - 200 m too thick at all locations (DH_run_3a in Figure 2-13). Scaling the accumulation rate to the Taylor Dome record, which is our lowest LGM accumulation rate, produces essentially no change in the glacier profiles, while scaling the RACMO 2.3 SMB by 60% leads to a worse fit due to the lack of ablation zones (DH_run_3c in Fig 13). The fit to Hatherton Glacier LGM ice thickness can be improved by moving the Darwin Glacier catchment boundary ~25 km into the model domain (DH_run_3i in Figure 2-15). There is no geologic evidence for this, but it may not be an unreasonable amount of change, given the enormous catchment areas of Byrd and Mulock glaciers. However, the rapid thinning during deglaciation propagates upglacier, and such thinning is not observed in our records of Hatherton Glacier fluctuations. Thus, the pattern of thinning cannot be matched using simple assumptions about catchment size or surface mass balance, and thus we conclude that this is an unlikely scenario. This supports our earlier conclusion that the elevation transect near the modern margin

of Darwin Glacier at Diamond Hill most closely represents the major ice thickness fluctuations since the LGM.

2.4.5 *Ice sheet model ensemble*

Our flowband model is only applied to the grounded Darwin and Hatherton Glaciers, and thus cannot be used to directly examine the effect of grounding-line distance on the ice thickness of Darwin and Hatherton Gaciers. We use the Pennsylvania State University 3-D ice sheet model (PSUICE) (Pollard and DeConto, 2012a) to examine the retreat ice from Byrd, Darwin-Hatherton, and Mulock glaciers. PSUICE uses a combination of the Shallow Ice and Shallow Shelf approximations (SIA and SSA, respectively) along with a parameterization of grounding-line flux (Schoof, 2007) to allow for full continent-scale simulations on kyr to Myr timescales, as well as an optimized model-parameter set that is tuned to match glacial geologic data from around the continent since 20 kyr BP (Pollard et al., 2016). However, this parameter set was optimized to available constraints for the entire WAIS, and because we are only interested here in the ice sheet in the Ross Sea, that parameter set may not be the most suitable. Therefore, we run the model first at 20-km resolution over the whole continent from 25 kyr BP to present, and use this to establish boundary conditions for an ensemble of 48 nested model simulations at 10 km resolution since 20 kyr BP. While this resolution is likely not sufficient to accurately represent the dynamics of Darwin and Hatherton glaciers, the modern ice discharge from those glaciers (~0.2 Gt/yr at present; Gillespie et al., 2017) is small compared to that from Byrd and Mulock glaciers (~27.5 Gt/yr at present; Stearns, 2011), so it can be neglected for the purposes of large-scale modeling of the Ross Sea Ice Sheet. We are interested in the relationship between ice thickness at the TAM front and the position of the grounding-line, and thus do not need to resolve the individual glaciers. The 10-km resolution was chosen as a trade-off between computing time and the ability to resolve pinning

points that may have a large effect on grounding-line migration. We vary four model parameters over a reasonable set of values determined by the large ensemble analysis of Pollard et al. (2016): basal slipperiness on the modern seafloor, isostatic rebound rate, ice shelf melt sensitivity to ocean temperatures, and a calving rate factor. We also use two different sea-level curves to explore the dependence of the model on time resolution in proxy records (Lisiecki and Raymo, 2005; Spratt and Lisiecki, 2016). Because our results show more gradual and recent deglaciation of the DHGS than at other locations in the TAM, our choice of parameter values is intended to slow down grounding-line retreat relative to the optimized parameter set of Pollard et al. (2016). Parameter values are tabulated in Table 2-2.

Table 2-2: Parameter choices for ice sheet model ensemble

Parameter	Values	Optimal value from Pollard et al. (2016)
Asthenospheric rebound time	1000, 2000 yrs	2000 yrs
Sub-shelf melting factor	0.5, 1	1, 3
Basal sliding coefficient on seafloor	10^{-5}, 10^{-6}, 10^{-7}	10^{-5}
Calving factor	0.7, 1	1
Sea-level curve	Lisiecki and Raymo, 2005; Spratt and Lisiecki, 2016	N.A. (only used LR04)

Scoring the runs against all available geologic data is beyond the scope of this paper. Instead, we focus on the pattern and timing of grounding-line retreat to the mouth of Darwin Glacier. By establishing a relationship between the ice thickness at the mouth of Darwin Glacier and the distance to the grounding-line, we can draw conclusions about grounding-line position based on glacial geologic data. Ideally, we seek a combination of model parameters that enables the grounding-line to slowly approach the mouth of Darwin Glacier, despite the steeply back-

sloping bed topography south of Minna Bluff, while still leading to early Holocene deglaciation of much of the western Ross Embayment (Spector et al., 2017). However, we also recognize that the parameters could vary in space and time, so this optimal solution could be non-unique. Furthermore, higher-order ice physics and adaptive mesh refinement to resolve grounding-line migration may be required to fully capture the processes involved in the retreat but require too much computational expense to be included in an ensemble of model runs over timescales of tens of thousands of years.

Results from our ice sheet model ensemble are shown in Figure 2-16, and we find that no combination of the parameters we explored reproduces the slow and steady drawdown through the Holocene that we observe in the glacial geologic data at Diamond Hill or on Hatherton Glacier. The basal sliding coefficient, the only parameter that strongly effects the thickness of the ice sheet downstream of Darwin Glacier, leads to a difference of ~600 m ice thickness between the fastest sliding value (10^{-5}) and the slowest (10^{-7}). While the ice at the mouth of Darwin Glacier begins thinning ~1 kyr earlier for the faster sliding scenarios, modern ice thickness is achieved by 5-6 kyr BP in all model runs.

While none of the model runs in this ensemble achieve what we consider to be a good fit to our data from Diamond Hill, the three clusters of runs defined by the three basal sliding coefficients display internally consistent qualities that are worth examining in order to better understand the sensitivity of the Ross Sea Ice Sheet near the mouth of Darwin Glacier. Figure 2-16 shows the relationship between ice thickness at the mouth of Darwin Glacier and the distance to the grounding-line. After an initial spin-up period during which the modeled ice sheet reaches a quasi-equilibrium thickness, each group shows a distinct relationship between these two variables. All three groups of models undergo slow, almost linear thinning as the grounding line retreats from

its LGM position to Cape Crozier. Once the grounding-line is upstream of Cape Crozier, ice thinning at the mouth of Darwin Glacier accelerates in the two groups of models with more basal sliding. Another increase in grounding-line retreat rate is noticeable in all three groups after the grounding-line retreats past a Minna Bluff. These two features are apparently important for resisting ice sheet retreat.

Ice thinning at the mouth of Darwin Glacier is less sensitive to grounding-line position when the grounding line retreats into Discovery Deep, the deepest part of the seafloor beneath the Ross Ice Shelf. This is surprising because the rate of grounding-line retreat increases as it reaches the back-sloping edge of Discovery Deep. This suggests that some pulses of retreat at the grounding line of the Ross Ice Sheet may not have left a strong signal of thinning at the mouths of TAM outlet glaciers, requiring a very low surface slope between the mouth of Darwin Glacier and the grounding line, hundreds of km away.

2.5 DISCUSSION

Darwin and Hatherton glaciers continued to adjust to regional deglaciation until ~3 kyr BP, which means that the grounding-line likely did not arrive at its present location until about that time. Darwin and Hatherton Glaciers lie roughly halfway between McMurdo Sound and Beardmore Glacier, which both deglaciated in the early Holocene (Spector et al., 2017), yet the timing of grounding-line arrival at Darwin Glacier is much more recent. This could imply that a large region extending across Byrd, Darwin, Mulock, and Skelton glaciers remained grounded for about 4 kyr after the grounding-line in the central Ross Embayment had retreated further south. It remains an open question how far along the TAM front this grounded ice persisted, and if it comprised a single, grounded ice mass or local piedmont lobes (Lee et al., 2017).

Steady thinning of Hatherton Glacier through the Holocene also supports a later arrival of the grounding line relative to glaciers to the north and south (Hall et al., 2015; Jones et al., 2015; Spector et al., 2017). Thinning at the modeled LGM grounding-line is accompanied by thinning at the mouth of Darwin Glacier, which would have propagated rapidly upglacier and been recorded in deposits alongside Hatherton Glacier. Our model experiments show that ice at the mouth of Darwin Glacier stops thinning once the grounding line stops retreating, although the timing and magnitude of these changes do not necessarily correspond to our data. There is no record of an exceptionally fast period of thinning at Hatherton Glacier, in agreement with our interpretation of the sparse data near the modern grounding line. However, our ice sheet model ensemble analysis suggests that periods of exceptionally fast grounding-line retreat — such as across the Discovery Deep region — would not necessarily correspond to noticeably faster ice thinning rates at the mouth of Darwin Glacier. A two- to four-fold increase in the modeled rate of grounding-line retreat as ice in Discovery Deep goes afloat does not cause faster drawdown at Darwin Glacier for most parameter choices. In the scenarios with the fastest basal sliding, there is an increase in the rate of thinning when the grounding-line retreats into Discovery Deep. However, this lags the change in the grounding-line migration rate and reaches a maximum thinning rate after the grounding line has already slowed. This suggests that the time at which grounding-line retreat starts and stops may be deducible from geologic data, but that there are significant complications in drawing conclusions about even relative rates of grounding-line migration from ice-elevation proxies.

While we are not able to determine the rate of grounding-line retreat, we can make a first-order estimate of the sensitivity of Darwin and Hatherton glaciers to grounding-line position using records from elsewhere in the Ross Sea. The grounding-line retreated past Ross Island >8.6 kyr BP (McKay et al., 2016), and McMurdo Sound became free of grounded ice between 7.5 and 9

kyr BP (Jones et al., 2015; Anderson et al., 2017). This is similar to the time at which Hatherton Glacier began to retreat from its last high-stand (8 – 9 kyr BP), and our glacier modeling suggests Darwin likely began thinning around this same time as well. If this is true, Darwin and Hatherton glaciers may be strongly dependent on the ice configuration near Ross Island. This conflicts with the results from the ice sheet model ensemble that predict high thinning rates at Darwin Glacier even as the grounding-line retreat slows down south of Ross Island, presumably due to increased ice shelf buttressing (Whillans and Merry, 2001). This discrepancy should be addressed with further modeling studies of outlet glacier response to grounding-line retreat and/or more data from near the modern grounding line of Darwin Glacier.

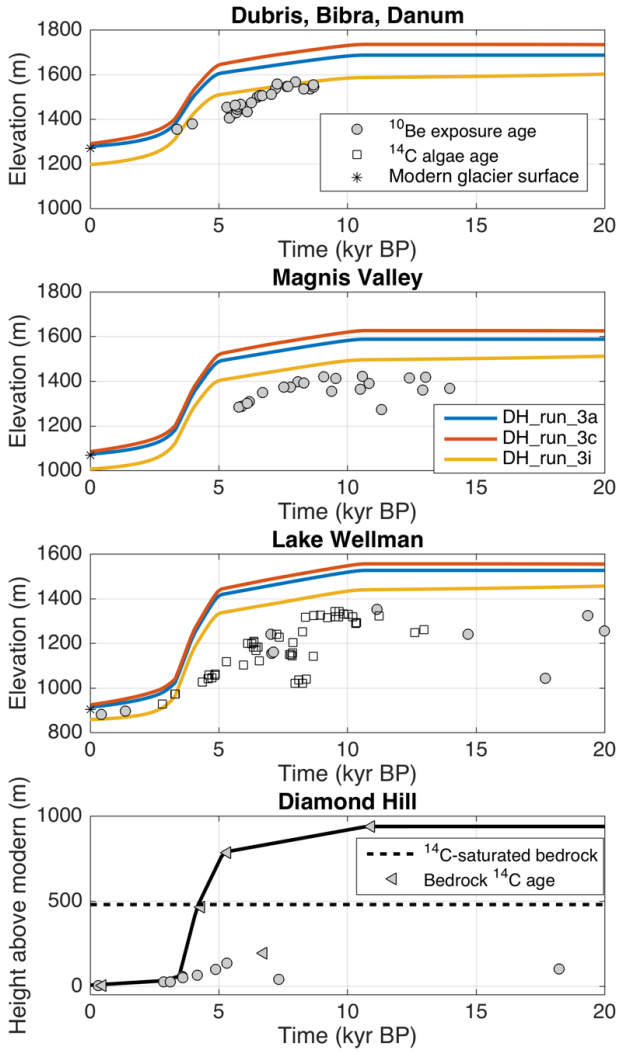

Figure 2-15: Flow-band model results for Experiment 3, in which we assume that the Holocene exposure ages high on Diamond Hill represent thinning of the main trunk of Darwin Glacier. Fitting the LGM thickness of Hatherton Glacier requires a much smaller Darwin Glacier catchment at the LGM, but we cannot fit the shape of the chronologies with any combination of simple assumptions about surface mass balance or catchment area. Thus, we rule out this scenario as unlikely, and conclude that the young exposure ages at high elevation on Diamond Hill reflect more local ice fluctuations.

Darwin and Hatherton Glaciers thinned at rates comparable to Scott Glacier near the modern grounding-line in the southern Ross Embayment (Spector et al., 2017). More rapid thinning of Mackay and Beardmore glaciers could be due to the steeply back-sloping bed topography in the immediate vicinity of the glacier mouths (Jones et al., 2015; Spector et al., 2017). The rapid collapse of grounded ice in and around McMurdo Sound ~7-9 kyr BP (Jones et al., 2015; McKay et al., 2016; Spector et al., 2017) may have been contemporaneous with the onset of thinning at the mouth of Darwin Glacier.

We suggest that the relatively recent and slow deglaciation of the DHGS is likely due to the convergence of Byrd and Mulock Glaciers near the mouth of Darwin Glacier, which led to dynamic ice thickening and lateral drag past Minna Bluff and Cape Crozier. Numerical investigations of grounding-line dynamics have shown that in general convergent flow can counteract the acceleration of dynamic thinning as the grounding line retreats down a reverse bed slope (Gudmundsson, 2013); positive strain rates measured south of Minna Bluff show that convergent flow and compression are causing dynamic thickening of the ice shelf in this region today (Thomas et al., 1984). Whillans and Merry (2001) identified Cape Crozier and Minna Bluff as controlling obstacles to the flow of the Ross Ice Shelf today, and we expect they would have had a similar effect during the last deglaciation. Together, the effects of convergent flow and lateral drag could have created a sheltered embayment that resisted grounding-line retreat for longer than glaciers farther to the south, even given the steeply back-sloping bed topography.

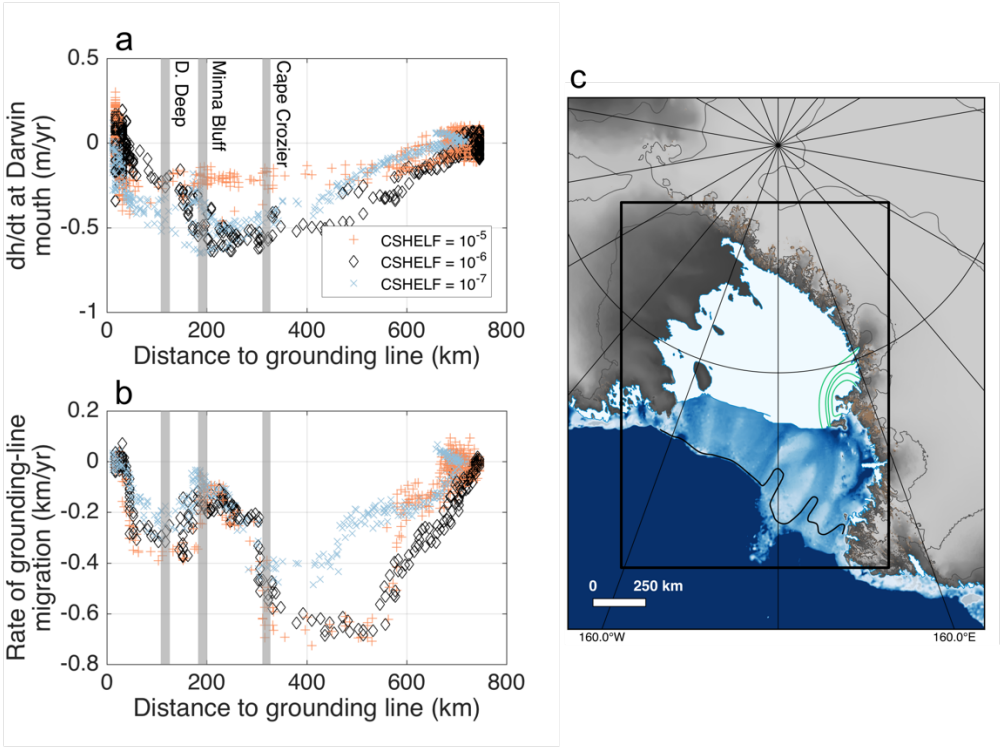

Figure 2-16: Results from the 48-member PSUICE ice-sheet model ensemble. (a) The relationship between rate of ice thickness change at the mouth of Darwin Glacier and the distance to the grounding-line for all ice sheet model runs. The basal sliding parameter (CSHELF) has by far the largest effect of the parameters we explored in the ensemble. Grey bars indicate the locations of the features we hypothesized to affect the rate of grounding-line retreat: Cape Crozier, Minna Bluff, and the Discovery Deep. (b) Grounding-line migration rate as a function of distance to the grounding line from Darwin Glacier. Negative values indicate retreat. Migration rate slows after the ice around Cape Crozer goes afloat, but thinning rates at Darwin Glacier are relatively constant. Ice thinning at the mouth of Darwin Glacier accelerates significantly in all model runs after the grounding-line has retreated past Minna Bluff, indicating that this feature provided a powerfully stabilizing backpressure to the grounded Ross Sea Ice Sheet. Perhaps counterintuitively, the acceleration of grounding-line retreat into the back-sloping Discovery Deep is not always accompanied by increased thinning rates at the mouth of Darwin Glacier. This indicates that there might not be a large thinning signal at the mouth of Darwin Glacier, even for a very rapid pulse of grounding-line retreat. (c) Simplified location map from Figure 2-1, with nested ice sheet model domain shown in the black box.

2.6 CONCLUSIONS

We have dated deposits of the DHGS in order to help constrain the timing and pattern of grounding-line retreat in the Ross Embayment since the Last Glacial Maximum. While the data suggest a later and slower deglaciation than that experienced by glaciers farther south (e.g. Spector et al., 2017), the scarcity of glacial deposits near the modern grounding-line of Darwin Glacier make direct interpretation difficult. We used a 3-D ice sheet model and a 1.5-D glacier flowband model to evaluate possible deglaciation scenarios consistent with our new data, and with assumptions about poorly known boundary conditions. Our key findings are:

- Glacial deposits in ice-free valleys alongside Hatherton Glacier record up to 450 m of thickening relative to present at Lake Wellman, 350 m at Magnis Valley, and 300 m at Dubris Valley. The glacier margin extended several kilometers into each valley during its maximum, and held a steady position for several thousand years before receding slowly and steadily through the Holocene. It did not reach its present thickness until ≤2.8 kyr BP.
- Erratics perched stably on granitic bedrock at Diamond Hill 10 km upstream of the modern grounding-line record 135 m of thinning between 5.1 kyr BP and 300 yr BP.
- Maximum bedrock ^{14}C exposure ages constrain the LGM ice surface near the modern grounding-line of Darwin Glacier to >190m but <500 m above the modern glacier.
- Ice covered the summit of Diamond Hill at the LGM, but did not cover the down-glacier flank closest to the modern Ross Ice Shelf. The summit was exposed ≤11 kyr BP, likely due to loss of ice flow over Bastion Bluff as Darwin Glacier thinned. Subsequent rapid thinning led to eventual detachment from the Ross Sea Ice Sheet.
- Flowband model results show that rapid deglaciation at the mouth of Darwin Glacier ~9 kyr BP predicted by the 3-D ice sheet model are not consistent with our geochronologic

data. Instead, our data are most consistent with slow and steady thinning at the mouth of Darwin Glacier between ~10 kyr BP and ~2 kyr BP, accompanied by a large decrease in catchment area through the Holocene.

- An ensemble of 48 runs using a 3-D ice-sheet model indicates that using glacial geologic data to constrain relative rates of grounding-line retreat is not straightforward. Periods of more rapid grounding-line migration may correspond to relatively constant thinning at outlet glacier mouths. The presence of pinning points such as Cape Crozier reduces the rate of modeled grounding-line retreat, but not the rate of thinning at Darwin Glacier.
- We suggest that the slow thinning of Darwin and Hatherton Glaciers through the Holocene could be the result of convergent flow with Byrd, Mulock, and Skelton glaciers, along with compression due to the flow past Minna Bluff. During the last deglaciation this effect may have acted to resist rapid grounding-line retreat to reach the modern position at these glaciers.

2.7 ACKNOWLEDGEMENTS

This work was supported by U.S. NSF grant 1246110 to JOS and HC, and grant 1246170 to BLH. In-situ ^{14}C measurements were generously funded by awards from the UW Department of Earth and Space Sciences and the Quaternary Research Center. Jan Lanearts and J.M. van Wessem provided RACMO data. Knut Christianson provided access to the Linux cluster used for the ice sheet model ensemble. We also thank the Antarctic Support Contractor, the U.S. Air National Guard, Ken Borek Air, and Petroleum Helicopters Inc. for logistical support.

Chapter 3. STRUCTURE OF CRARY ICE RISE REVEALED BY HF AND UHF RADIO-ECHO SOUNDING

Trevor R. Hillebrand, Howard Conway, Carlos Martin, John Paden, Michelle Koutnik, J. Paul Winberry, L. Jade Cooley, Richard C.A. Hindmarsh

3.1 ABSTRACT

Crary Ice Rise formed as the Ross Ice Shelf re-grounded on a topographic high ~1 kyr BP, but little is known about how it evolved. We present new radio echo sounding data from two ice-penetrating radar systems operating at 7 MHz and 750 MHz center frequencies, respectively. Our data confirm that Crary Ice Rise contains relict shelf ice and reveal complex englacial structures that hold clues to the evolution of the ice rise. We map a bright reflector that records strong deformation in the central plain of the ice rise, and little deformation on the southwest flank. This reflector is frequently coincident with strong diffractors, many of which completely obscure the bed reflection beneath them. We interpret these to be former rifts and/or basal crevasses within the ice shelf that were filled with marine ice. Their contact with the bright reflector suggests that it is caused by saline ice deposited by seawater flooding the permeable firn. Marine ice deposition within rifts could have helped the ice rise incorporate neighboring shelf ice by providing a dynamical link between the grounded ice rise and floating ice.

3.2 INTRODUCTION

Ice rises are locally grounded regions within ice shelves that provide stabilizing backpressure against ice-sheet flow (Matsuoka et al., 2015). Ice rises potentially have a large effect on ice-sheet stability, as model experiments have shown them to cause grounding-line advance in

geometries that would otherwise lead to grounding-line retreat (Goldberg et al., 2009). The importance of including ice rises in ice-sheet models has recently been emphasized by the inference of a widespread late-Holocene re-advance of the grounding-line to its current position in both the Ross and Weddell Sea sectors, driven by isostatic rebound (Kingslake et al., 2018). Because ice rises generally rest on bathymetric highs beneath the ice shelf, these would have been the first features on which the ice shelf grounded during such a re-advance at the end of deglaciation. However, many Antarctic ice rises are smaller than the resolution of continent-scale ice-sheet models, and are thus difficult to incorporate into simulations, even though they have a strong influence on ice flow. Therefore, without better parameterizations of ice-rise dynamics, estimates of past and future ice-sheet retreat based on long-term (100 kyr to Myr) continent-scale model investigations could poorly reconstruct past behavior and poorly predict future ice-sheet retreat.

Crary Ice Rise is a peninsula of grounded ice at the mouth of Whillans Ice Stream in West Antarctica (Figure 3-1), surrounded by the Ross Ice Shelf. Temperature profiles measured through Crary Ice Rise have revealed that it likely grounded ~1 kyr BP (Bindschadler et al., 1990), either as the result of isostatic rebound (Kingslake et al., 2018) or by increased discharge from the Siple Coast ice streams establishing contact with the seafloor (Bindschadler, 1993). The ice rise currently provides approximately half of the resistance to the flow of Whillans Ice Stream (MacAyeal et al., 1987), but streaklines on the surface of the Ross Ice Shelf show a history of complex coupling between the ice rise and the ice shelf (Fahnestock et al., 2000). While the Siple Coast ice streams have stagnated and reactivated multiple times over the last thousand years (Catania et al., 2012), the formation of Crary Ice Rise has been generally characterized as only a two-stage event (Bindschadler, 1993). Regional scale models have included the ice rise, but as a

static feature that does not dynamically evolve (Hulbe and Fahnestock, 2004; 2007). To better understand how the formation of Crary Ice Rise affected the Ross Ice Shelf and West Antarctic ice streams, we investigate possible processes and the sequence of events that contributed to the regrounding of the ice rise.

In this paper, we present new radio-echo sounding data that reveal new information about the history of the ice rise. We map englacial structures, bed topography, and internal reflectors across the ice rise in an effort to understand its evolution and present-day dynamics. The sequence of events recorded in the ice involves large stress gradients, ice fracture, and marine ice deposition — all of these are processes that defy simple modeling. Our results add to the literature on the englacial structure and evolution of Antarctic ice rises, which contribute necessary boundary conditions, validation criteria, and development of parameterizations for numerical models.

3.3 ICE-PENETRATING RADAR SURVEYS

3.3.1 *HF and UHF radar systems*

We used two ground-based ice-penetrating radar systems in order to map the internal structure of Crary Ice Rise. For wide-range radio-echo sounding, we used the University of Washington high frequency (HF) mono-pulse ice-penetrating radar operated at 7 MHz with a wavelength of 24m in glacier ice. Vertical resolution is equivalent to a quarter-wavelength, or 6 m. This radar system has been used widely in ground-based mapping of ice streams and ice rises across the Siple Coast of Antarctica (e.g., Conway et al., 2002; Ng and Conway, 2004; Catania et al., 2010). At this frequency, internal reflections are primarily caused by changes in electrical conductivity due to changes in the impurity content of snow through time (Fujita et al., 1999). The

portability and robustness of this system allowed for reconnaissance-style mapping of the entire ice rise.

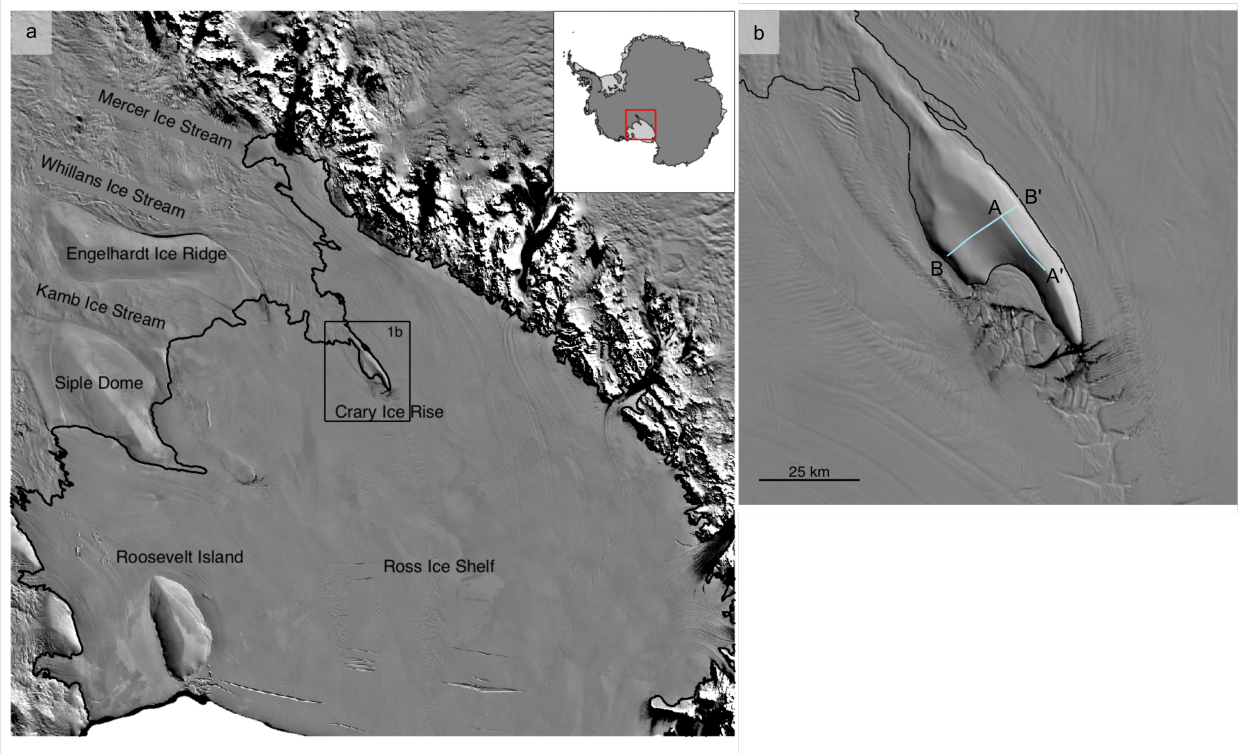

Figure 3-1 Location of Crary Ice Rise in the Ross Embayment of Antarctica. The tracks of the two main radar surveys are shown in 1b. Figure generated using the Antarctic Mapping Toolbox for MATLAB (Greene et al., 2017).

The ultra-wideband ultra-high-frequency (UHF; 600-900 MHz – center-frequency 750 Mhz) pulsed-chirp radar from the Center for the Remote Sensing of Ice Sheets (CReSIS) provided detailed bed topography and internal stratigraphy (e.g., Lewis et al., 2015). The 600-900 MHz range is divided into 16 sub-bands with some overlap; 16 1-μs pulses are repeated at 50 kHz, and the 16 antennae are switched between transitting and receiving modes (Rodriguez-Morales et al., 2014). The wavelength in glacier ice is ~22 cm. The 1μs pulse duration caused signal saturation of the upper layers, but enabled us to image deep layers and the ice-bed interface. However, the

higher frequency of this system makes it more sensitive to scattering of the signal due to impurities in the ice relative to the 7MHz system, and thus some deep layers are less visible than in the HF data. As seen in Figure 3-2, however, the bed reflection is very strong almost everywhere in our data when not blocked by englacial structures. This system is heavier and more susceptible to damage in this terrain than our HF radar. Due to widespread ~0.5m high sastrugi and constant drifting snow conditions endangering the radar, we used this system to investigate target areas in great detail, but we avoided using it far from camp except under particularly good conditions. Data were migrated using a Fourier transform method (Stolt, 1978) and the standard CReSIS processing tools.

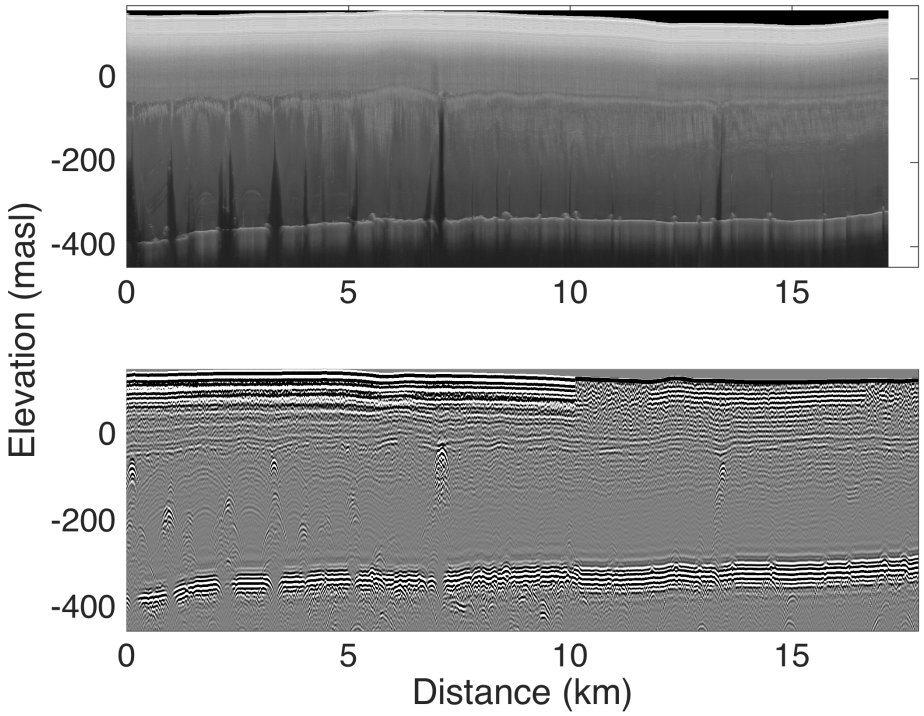

Figure 3-2: Transect A-A' along the axis of the main ridge of the ice rise, with the 750 MHz CReSIS radar shown in the top panel and the UW 7MHz radar shown in the bottom panel. Data have been corrected for surface topography. The most notable features are the strong bed reflection in both radars, the strong diffractors that often block out the bed echo, and the layer at ~200 m depth at which many of the diffractors originate.

3.3.2 *Radar survey results*

3.3.2.1 Radar profile A-A' along main ridge axis

The A-A' survey down the axis of the main ridge of the ice rise (Figure 3-1) reveals a strongly reflecting layer at ~200 m depth that is nearly continuous in all data except where punctuated by diffractors (Figure 3-2); hereafter this reflector is referred to as "Layer A". This layer is apparent in both the 750 MHz and the 7 MHz datasets. In the 7MHz data, internal reflection horizons are detectable below Layer A. Detection of internal reflections is inconsistent in the 750 MHz. The loss of internal reflectors below Layer A often coincides with an increase in the local dip angle of that reflector, and thus is likely an effect of the sensitivity of UHF systems to dipping reflectors (Holschuh et al., 2014).

The bed echo is often missing beneath strong diffractors that originate from Layer A. Three of the four strong diffractors that intersect the layer in A-A' block the bed echo. Numerous other strong diffractors that also block the bed echo occur lower in the ice column. The internal reflecting horizons warp downwards towards these diffractors, forming arcs with amplitudes of up to ~40-50 m (Figure 3-2). Such intense and localized drawdown of internal reflection horizons is most likely caused by basal melting (Catania et al., 2006), which likely occurred while this ice was contained in the Ross Ice Shelf. The strong diffractors and bed echo loss in the trough between these arcs leads us to hypothesize that basal melting caused flexure of the ice shelf, leading to concentrated extensional stresses and basal crevassing above melt channels (Vaughan et al., 2012). Marine is the only material we know of that is likely to both exist within the ice-rise ice and completely absorb the transmitted energy. We thus hypothesize that the strong diffractors within the ice at Crary Ice Rise are the result of marine ice formation in former basal crevasses or rifts in the Ross Ice Shelf, a process that has been documented in modern rifts (Khazendar and Jenkins,

2003), and could act to strengthen ice shelves (Rignot and MacAyeal, 1998). This is represented schematically in Figure 3-3.

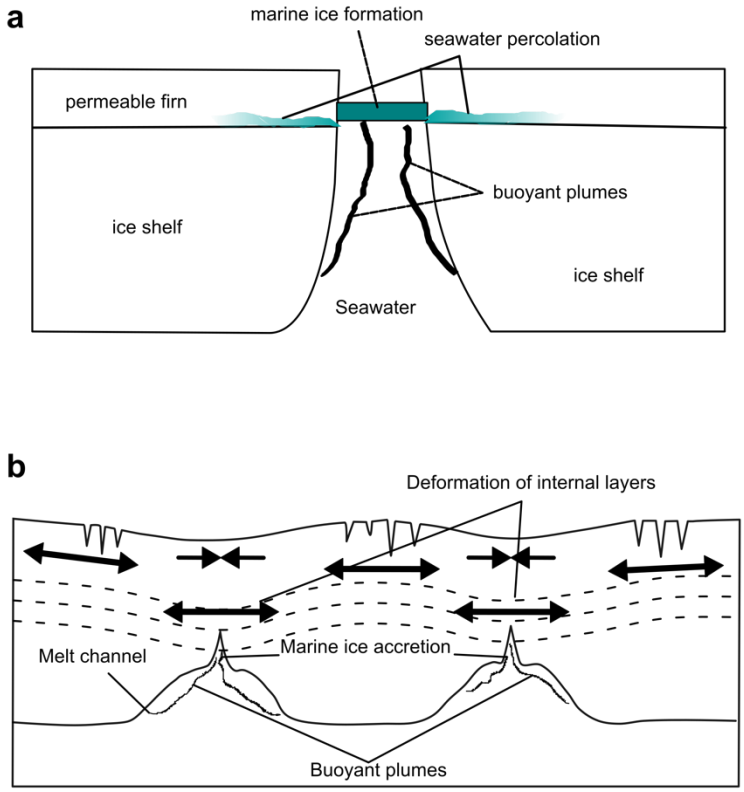

Figure 3-3: Schematics of the hypothesized processes responsible for the structures observed in our radar surveys. (a) Ice shelf rift filling with marine ice (modified from Khazendar and Jenkins, 2003), and seawater percolating into the firn column where it lies below sea level. (b) Basal melt channels in an ice shelf causing flexure and crevassing (modified from Vaughan et al., 2012). Black arrows show direction and relative magnitudes of deviatoric stresses. Marine ice may have been deposited in basal crevasses caused by the stress pattern.

3.3.2.2 Radar profile B-B' across the ice rise

The B-B' profile across the ice rise reveals four separate zones of ice rise structure, which will here be referred to as zones B1 through B4 (Figure 3-4). Zone B1 — from 0 to 5 km along B-B'— crosses the lower NE ridge of the ice rise, which is located above the shallowest portion of the bed. Layer A cannot be distinguished from the rest of the ice column in this zone. Point

diffractors are found ~100 m off the bed, but they generally do not occlude the bed echo in this zone. A single strong diffractor in this zone occurs at a depth of ~100 m.

Zone B2 — from 5 to ~12 km along B-B' — is a zone of disturbed ice, with diffractors extending up to 300m above the bed that obscure the bed echo. Layer A is sometimes found in this zone, but is often discontinuous and strongly deformed. Small-scale internal reflectors are generally not detectable in the CReSIS data for ~100 m above Layer A in this zone. However, a second, shallower reflector occurs consistently 50-100 m above Layer A and is detected by both systems. Conformal, meteoric ice layers can be identified at the top of the ice column. The ice rise bed in Zone B2 is only partially visible in our data, but it seems to be rougher than in Zone B1. This could be due sediment being squeezed up into basal crevasses, or simply to the pre-existing bed topography. The bed in Zone B2 generally slopes downward towards the crest of the main ice rise divide.

Zone B3 — from 12 to 17 km along B-B', including the crest of the main ridge — is characterized by a stronger expression of Layer A that is less deformed than in Zone B2. Relatively uniform internal reflectors overlay Layer A in Zone B3. The shallower bright reflector is not observed above Layer A. The lowest 100 m of the ice column in Zone B3 exhibits structures spaced at roughly regular 1-km intervals. These enigmatic reflectors dip ~10° downwards towards the main crest of the ice rise and intersect the bed. Like in Zone B1, the crest of the main ice rise divide occurs over a sloping bed. The diffractor at the divide observed in the 7MHz data is a reflection from a seismic shot hole that we drilled.

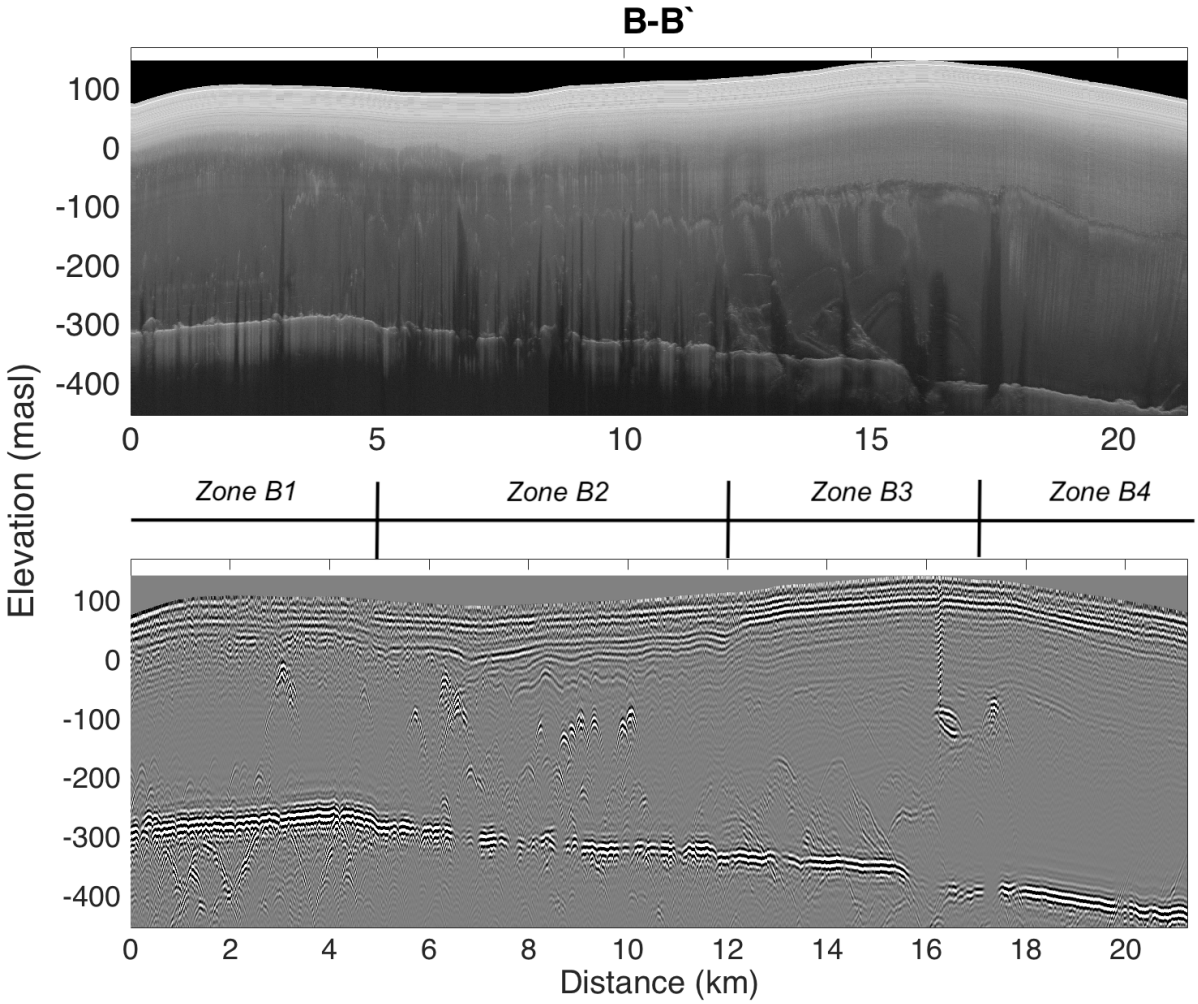

Figure 3-4: Results of the B-B' survey, with the CReSIS 750 MHz radar (top panel) and the UW 7 MHz radar (bottom panel). The survey reveals four distinct structural zones of the ice rise, referred to as B1 to B4 in the text. Compared with zones B2 & B3, the englacial stratigraphy in upper 200m of zones B3 & B4 is relatively undisturbed.

In Zone B4 — from 17 to 22 km along B-B' — Layer A is present and mostly free of diffractors. The ice column in this section is generally undisturbed, and the meteoric ice column above Layer A is 30-60 m thicker than in Zone B3. This zone is notable for the relatively

undisturbed nature of the ice. While there is one strong diffractor that blocks out the bed echo at ~17.5 km along B-B', the remainder of Zone B4 is relatively homogeneous.

The lines we surveyed parallel to B-B' show the same general features as B-B' (Figure 3-5). Most striking in these profiles is the relatively high amount of basal crevassing and deformation on the central plain of the ice rise compared to the SE flank of the main ridge (Zone B4). The obscured bed reflection beneath the diffractors and steeply dipping deep reflectors is a characteristic feature in Zone B3. The largest of all echo-free areas is found near the tip of the ice rise, where the bed reflection and all returns below Layer A are missing for > 1km along our profile (bottom panel in Figure 3-5). None of these profiles shows evidence of a Raymond bump beneath the ice divide (Raymond, 1983), likely because the ice rise is still too young.

A linear feature visible in the 125-m resolution MODIS imagery (Haran et al., 2014) intersects the modern grounding-line near the rifted zone of the ice rise, and trends parallel with the main ridge crest (shown in Figure 3-1 and Figure 3-5). This lineation manifests as a break in slope in the References Elevation Map of Antarctica (REMA) DEM (Howat et al., 2019) and broadly coincides spatially with (i) a down-warping trend of the bright reflector, (ii) a large increase in the amount of spatially high-frequency deformation of the reflector, (iii) a very strong diffractor that completely obscures the bed reflection for >1 km, and (iv) a number of inclined features in the ice beneath Layer A.

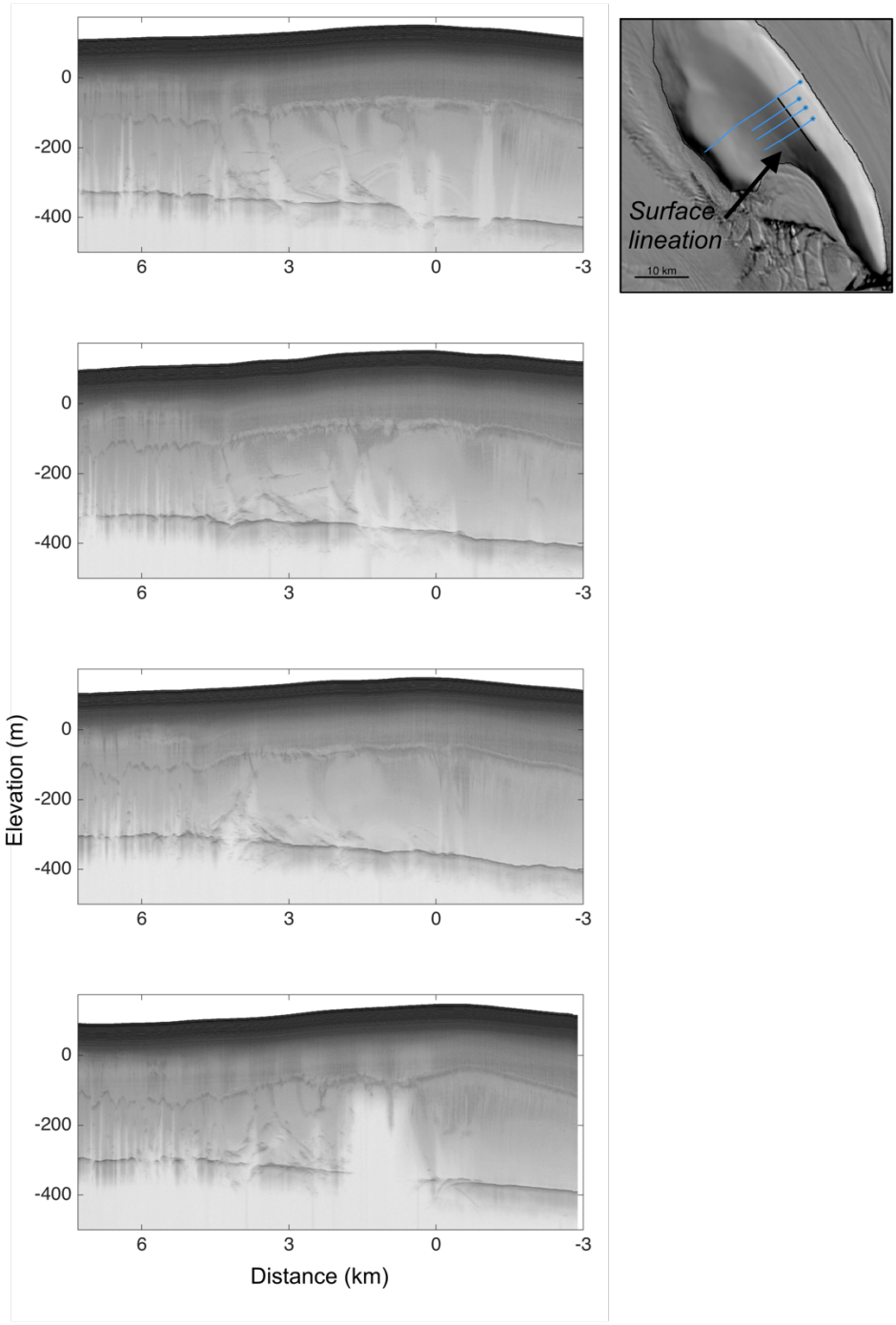

Figure 3-5: 750 MHz CReSIS radar profiles across the main ridge of the ice rise, showing the evolution of the enigmatic basal reflectors and the marine ice-filled rifts on the inner flank of the ice rise. Top to bottom profiles correspond to top to bottom tracks on the map. Distance on horizontal axis is relative to the A-A' profile, shown in black on the map, with negative distances corresponding to the shelf-proximal (southwest) side of the main ridge, marked by asterisks on the map.

3.3.2.3 Material filling basal crevasses

The bed reflection appears depressed beneath many of the hyperbolae within the ice column. This suggests that the diffractor is associated with a change in permittivity, which causes a change in the wave speed and thus a change in travel time to the bed. Figure 3-6 shows an isolated hyperbola within the ice column, and the associated depression in the bed reflection beneath. It is possible to use the magnitude of the increased travel time beneath the diffractor to estimate the relative permittivity of the material in the ice column beneath it. Assuming the difference in actual ice thickness is very small compared to the average ice thickness over the span of the depression, we can formulate the distance to the bed as $z_b = \frac{t_b}{\sqrt{\varepsilon_i}}$, where t_b is the two-way travel time of the EM wave to the bed, and ε_i is the relative permittivity of glacier ice (~3.2 at 7 MHz). This distance is equivalent to the distance travelled by the wave that passes through the diffractor and the ice column beneath: $z_b = \frac{t_d}{\sqrt{\varepsilon_i}} + \frac{t_c - t_d}{\sqrt{\varepsilon_c}}$, where, t_d is the two-way travel time to the diffractor, t_c is the two-way travel time to the bed beneath the diffractor, and ε_c is the permittivity of the ice column beneath the diffractor. Setting these two expressions equal to each other and solving for the permittivity beneath the diffractor, we obtain $\varepsilon_c = \varepsilon_i \left(\frac{t_c - t_d}{t_b - t_d}\right)^2$.

For the configuration shown in Figure 3-6 (i.e., ε_i = 3.2, t_b = 4.3 μs, t_d = 1.80 μs, and t_c = 4.35 μs), this results in a value of ε_c = 3.3, which is between that of glacier ice and marine ice. Thus, the origin of the hyperbola can likely be attributed to a former basal crevasse in the ice shelf that partially filled with marine ice before creeping shut.

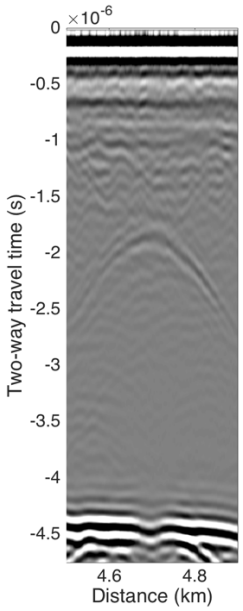

Figure 3-6: Diffractor and dip in bed reflection from profile B-B' (Figure 3-4).

3.3.2.4 Ice thickness and Bed Topography

We have compiled our radar data from the 7 MHz and 750 MHz systems into comprehensive maps of ice thickness and bed topography across the ice rise (Figure 3-7). We use the ice thickness and bed topography to compute the height of the ice surface above floatation. The main ridge of the ice rise is ~100 m above floatation thickness; the central plain is 50-60 m above floatation; and the shallow ridge is ~75 m above floatation. By contrast, the neck of the ice rise where it connects to Whillans Ice Plain is ~20-30 m above floatation.

In Figure 3-7d, we compare our measured ice thickness with the Bedmap2 compilation (Fretwell et al., 2013). The Bedmap2 product across Crary Ice Rise only includes data from five profiles from airborne surveys in the 1980s (Shabtaie and Bentley, 1987). The root mean square misfit between our data and the Bedmap2 product is 42 m, while the ice thickness in the Bedmap2 product is on average too thin by 12 ± 40 m (2 ± 8% ice thickness; 1σ). Errors near the connection

of the ice rise to Whillans Ice Plane are relatively low, while Bedmap2 reports ice thicknesses in the central plain that are more than 50 m too high, and on the main ridge that are ≥ 50 m too low. The maximum error in the Bedmap2 data within our surveyed area is 28%.

3.3.2.5 Deformation of Layer A

The abrupt transition in stratigraphy beneath Layer A (Figure 3-2; Figure 3-4) suggests that it represents a period when dynamical conditions changed on the ice rise. We mapped the layer across the ice rise in the 750 MHz data using the picking software from the CReSIS MATLAB toolbox, modified to pick internal stratigraphy. Because the depth of Layer A is sometimes difficult to define due to scattering within the ice column, we picked the top of the layer. Layer A is more easily detected in the 750 MHz data than in the 7MHz, so for now we exclude that dataset. A map of the depth to this layer is shown in Figure 3-8.

The depth to Layer A is strongly heterogeneous across the ice rise and it is not significantly correlated with either bed topography (r =0.003) or surface topography (r = -0.17). Because the deeper portion of Crary Ice Rise is likely former shelf ice, we do not expect a strong correlation between the depth of the layer and the bed or with the present surface topography, partly because of the irregular topography at the base of ice shelves (Gourmelen et al., 2017) and also post-grounding processes and accumulation. The large undulations in the structure of Layer A compared with the bed and surface topography of the ice rise indicate that multiple stages and/or processes were likely involved in the evolution and deformation of the layer. A single ice dynamical mechanism (e.g., vertical shear, longitudinal compression, basal sliding, etc.) is unlikely to produce low relief in one area and high relief in another. Indeed, Crary Ice Rise has undergone major changes over the last ~1000 years, including at least two separate episodes of

ice-shelf grounding and the transition from a sliding to a frozen bed (Bindschadler et al., 1990; Hulbe and Fahnestock, 2007).

We use proper orthogonal decomposition (POD) to deconstruct the layer into a series of additive surfaces. POD reduces high-dimensional data into a series of low dimensional basis functions, known as modes. Each mode explains a certain percentage of the variance of the dataset. POD is widely used to understand high-dimensional dynamic systems, such as fluid flow, when the underlying equations are not known (e.g., Chatterjee, 2000). Each mode does not necessarily have a physical significance, but rather reflects the requirements and definition of the POD as well the underlying dynamics of the system (Monahan et al., 2009), and so attribution of a single process to each mode should be avoided. However, given some *a priori* knowledge of the possible dynamics of the system, and caution in interpreting the mechanistic significance of each mode, the POD is a powerful tool for revealing the structures in a dataset. Here we use it primarily to detrend the data and to compute the amount of variance contained in that trend.

Results of the POD indicate that 68% of the variance in the geometry of the bright reflector is explained by a single mode that describes a (spatially) low-frequency surface (Figure 3-8). The remaining 32% of the variance is due to the sum of higher-order modes, none of which individually explain more than 2.5% of the total variance. The sum of the first 17 modes explains 95% of the variance. Because the first mode contains much more of the variance than any other mode, we accept that the layer is best described by the sum of a slowly varying surface (mode 1) and a rapidly varying surface (the other modes).

While each mode does not necessarily hold its own physical significance, interpreting the reflector as the sum of a low-frequency surface and a high-frequency surface is reasonable. Assuming the layer is isochronous and was initially almost flat when it was deposited, we can seek

a physical explanation for each style of deformation. Physical mechanisms that would produce low-frequency spatial variations include divide flow and ice shelf flow. Possible mechanisms for high-frequency spatial variations are found in the vicinity of the ice rise today, including, (i) local ice shelf sliding over topographic highs (ice rumples), (ii) uplift and/or tilting of rift-bounded bergs, (iii) intense and localized basal melting, (iv) lateral shearing at the ice rise boundary, (v) compression upstream of grounded ice, and (vi) acceleration and flotation at the grounding-line. The fact that the slowly varying surface contains 68% of the variance in the layer geometry indicates an overall control of relatively simple ice flow processes on the shape of Layer A. The high-frequency surface is likely the combined product of many of these processes, which may have taken place before, after, or concurrent with the broader-scale deformation represented by the low-frequency surface.

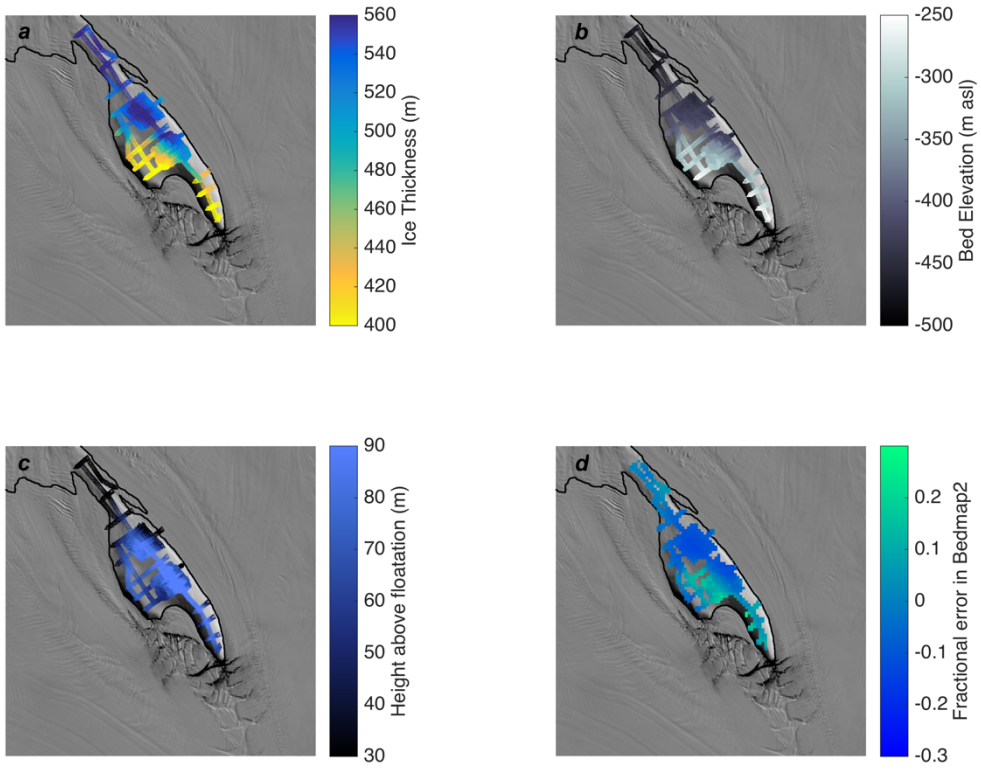

Figure 3-7: Ice thickness (a), bed elevation (b), height above floatation (c), and fractional error in Bedmap2 (d) from our combined 7MHz and 750 MHz radar surveys. For comparison with Bedmap2 data (d), our picks were re-gridded into the 1 km Bedmap2 grid and averaged within grid cells. Imagery and grounding line (black) from MODIS Mosaic of Antarctica (Haran et al., 2014), plotted using software from (Greene et al., 2017). The Bedmap2 ice thickness is on average 12 ± 40 m (1σ) thinner than our measured ice thickness. Root Mean Square error in Bedmap2 is 42 m.

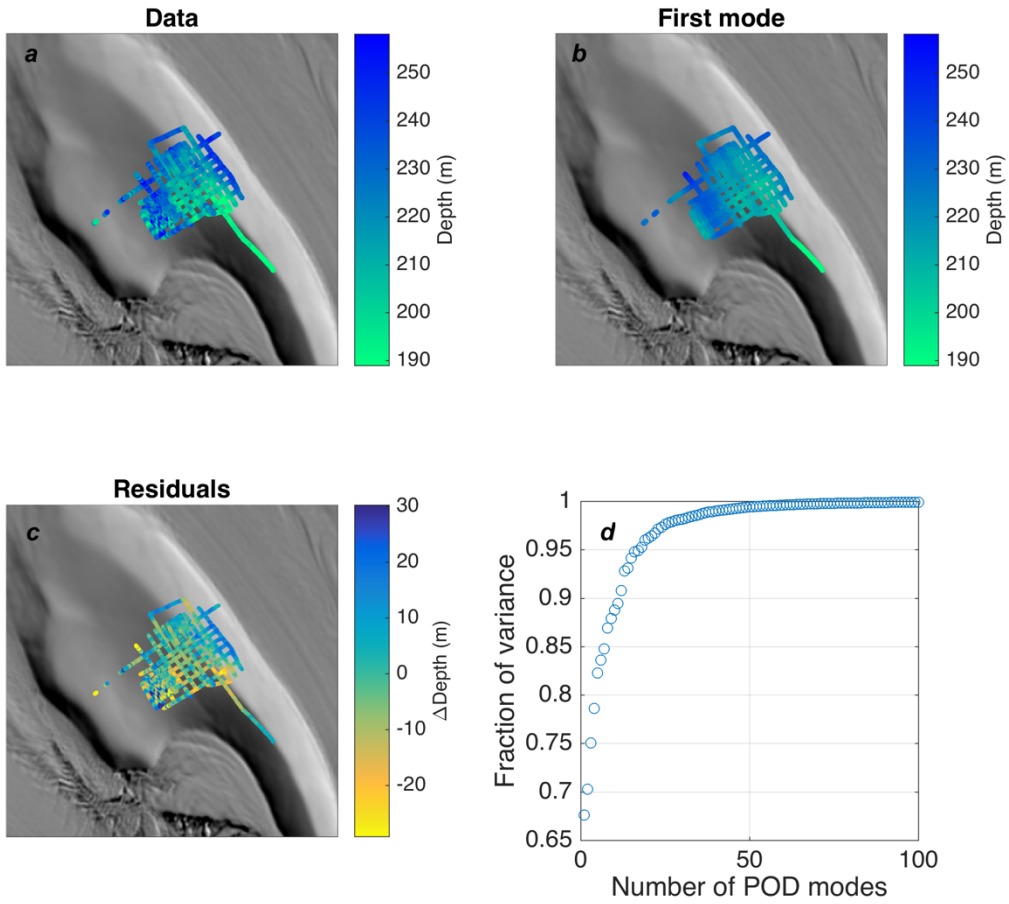

Figure 3-8. The bright reflector can be modeled as the sum of two surfaces with different spatial frequencies. a: Depth to the bright reflector, mapped in the 750 MHz CReSIS radar data. b: Single-mode representation of the bright reflector as a slowly varying surface, containing 68% of the variance in the mapped layer depth. c: The residuals between the data and the first mode of the proper orthogonal decomposition (data minus model). Note the high-frequency and high-amplitude deviations from the slowly varying surface in the central plain of the ice rise. d: Cumulative fraction of the variance in the Layer A depth contained in POD modes. The first mode contains 68% of the variance, while the sum of the first 20 modes contains ~95% of the variance.

3.4 WAVEFORM MODELING

We use the open-source waveform modeling software gprMax (Warren et al., 2016) to test hypotheses for the origins of the englacial and basal reflections we observe across Crary Ice Rise. gprMax solves Maxwell's equations in two or three dimensions using the Finite-Difference Time Domain method. We model our 7MHzwaveforms in 2D. The ultra-high frequencies of the 750MHz system requires high model resolution, which for now is computationally impractical for such large model domains. Dielectric properties used in the following experiments are shown in Table 3-1.

We test two hypotheses for the strong diffractors that block out the bed echo. Because these often originate at Layer A, we consider it possible that these represent either (Hypothesis 1; H1) pockets of brine trapped within glacier ice, or (Hypothesis 2; H2) accreted marine ice in former basal crevasses or rifts. To test H1, we need to estimate the dielectric properties of isolated brine pocket; studies of brine percolation layers have been conducted in places where the brine is still actively entering an ice shelf (e.g., Campbell et al., 2017; Grima et al., 2016), or recharging from groundwater into the englacial system (Badgeley et al., 2017). Thus, here we model two brine pockets, 3m and 10 m thick, and both 10-m wide, which could have formed from a dense firn layer in which pore spaces were filled by isolated pockets of seawater. We obtain an effective dielectric constant of 6.85 using the Looyenga mixing formula (Looyenga, 1965) for glacier ice with 15% seawater by volume. This is a maximum estimate (Thomas, 1975), but we use it because we are seeking a plausible explanation for the loss of the bed echo. We assume that the brine is composed of a series of non-connected spheres, and thus that changes in bulk conductivity from glacier ice are negligible (Lux, 1993). This assumption should be tested with more rigorous modeling and laboratory experiments. We do not have constraints on the thickness

of the layer. It would be possible to estimate the layer-thickness using the power drop across it, but given the given the uncertainties in the dielectric properties this is not justified.

To test H2, we model wave propagation through a column of marine ice, which is our preferred hypothesis because of the down-warping of internal reflectors towards the diffractors (e.g., in Figure 3-2). Because marine ice fills fractures from the top down, we model three different heights (10 m, 100m, and 150m) of marine ice columns extending downward from the same point 150 m off the bed. Model results are shown in Figure 3-9 and Figure 3-10, for whole-domain echograms and comparison of the bed reflection beneath the diffractors, respectively. The differences between the effect of marine ice columns and brine pockets on the radar return can be seen in the bed return. Because the brine pockets have a much higher permittivity than marine ice, the bed reflection is noticeably delayed beneath the 10m-thick brine pocket, but not beneath the 10m-thick marine ice column. The 100m- and 150m-thick marine ice columns cause a strongly attenuated bed return, representing a decrease of 50-60% relative to the amplitude of the bed reflection away from the diffractor. This strong decrease in the amplitude of the bed return is consistent with our observations, and thus we conclude that the strong diffractors are caused by marine ice that filled basal crevasses and rifts.

We also seek an explanation for the dipping reflectors in Zone B3. The simplest hypothesis is that these are caused by shearing of the same marine ice-filled crevasses shown in Figure 3-9 and Figure 3-10. An alternate hypothesis is that these are areas with bands of debris-rich ice, such as those found on the surface near the north-western edge of the ice rise (Gaylord and Robertson, 1975). We model both scenarios for marine ice- and debris-filled crevasses dipping at 10°, using a relative permittivity of 3.1 and a conductivity of 8.0×10^{-5} S m^{-1} for debris-rich ice with 15% sand (Christianson et al., 2016). The results of this experiment are shown in Figure 3-11. Both

scenarios fit the observations reasonably well, and result in a dipping reflector that does not strongly diminish the bed echo, with a faint hyperbola originating at the intersection of the dipping feature with the bed. Based on model results, both of these are equally likely possibilities. However, we see no reason to invoke a new mechanism for these features, and thus we interpret them as marine ice-filled crevasses that have been sheared by ice flow.

Finally, we investigate the total loss of bed echo for hundreds of meters beneath strong diffractors, like that at 7.5 km in profile A-A'. Because the narrow marine ice column in Figure 3-9 results in a 50-70% reduction in the bed reflection amplitude, it is reasonable to hypothesize that a rift totally filled with marine ice could completely block out the bed echo. We model this scenario in Figure 3-12, using both a triangle and a rectangle of marine ice of the dimensions defined by the strong diffractor at 7.5 km in profile A-A': 300 m high, 700 m wide. The modeled rift reproduces the down-warping and complete attenuation of the bed echo in the center, as well as the hyperbola originating at the triple-junction between bed, glacier ice, and marine ice. While this is a significant amount of marine ice, it is reasonable by comparison with the thick packages of marine ice accreted to the bases of modern ice shelves. For instance, a single continuous band of marine ice 200 m thick extends 200 km downstream of a promontory in the Amery Ice Shelf (Craven et al., 2009), and a 50-350 m thick marine ice layer is continuous for hundreds of km beneath the Ronne Ice Shelf (Thyssen et al., 1993).

Table 3-1: Dielectric properties of the different materials used in waveform modeling. Values are from Christianson et al. (2016) for a 5 MHz radar.

Material	Relative permittivity	Conductivity (S m^{-1})
Glacier ice	3.2	7.0×10^{-5}
Marine ice	3.4	5.7×10^{-4}
Debris-rich ice (15% sand)	3.1	8.0×10^{-5}
Frozen till (40% groundwater ice)	2.9	3.4×10^{-4}
Unfrozen bedrock	12	0.0048
Seawater	77	2.9

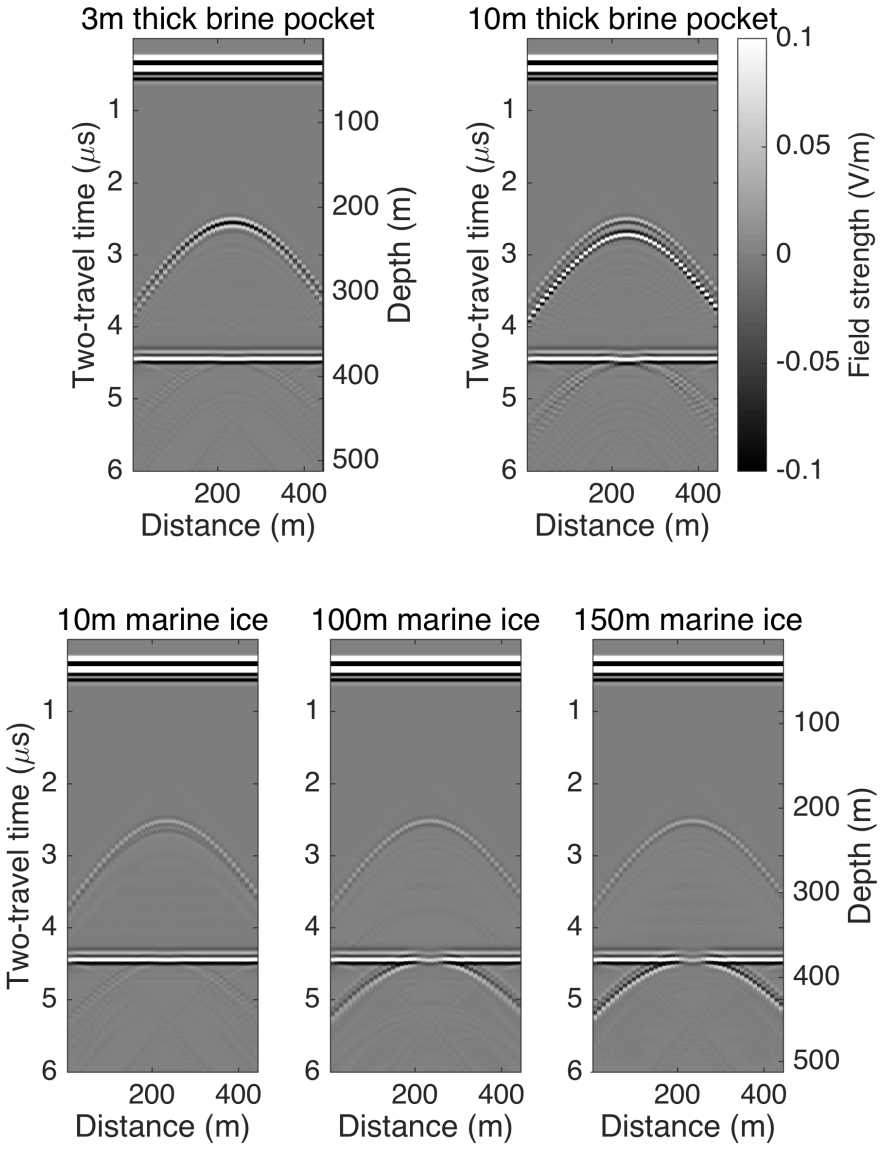

Figure 3-9: Waveform model results from simulations using gprMax, comparing the radar signature of a 10 m-wide pocket of brine-soaked ice (15% brine by volume) 3 m and 10 m thick (top row) with columns of marine ice 10 m, 100 m, and 150 m high. The 150 m-high marine ice column is in contact with the bed. In all cases the top interface is 150m above the bed. Notably, the brine pocket does create a dip in the bed reflection, due to its higher permittivity and lower wave speed. However, it does not produce a noticeably dimmer bed return, unlike the marine ice crevasses, under which the amplitude of the bed reflection is decreased by ~70% compared to the rest of the bed.

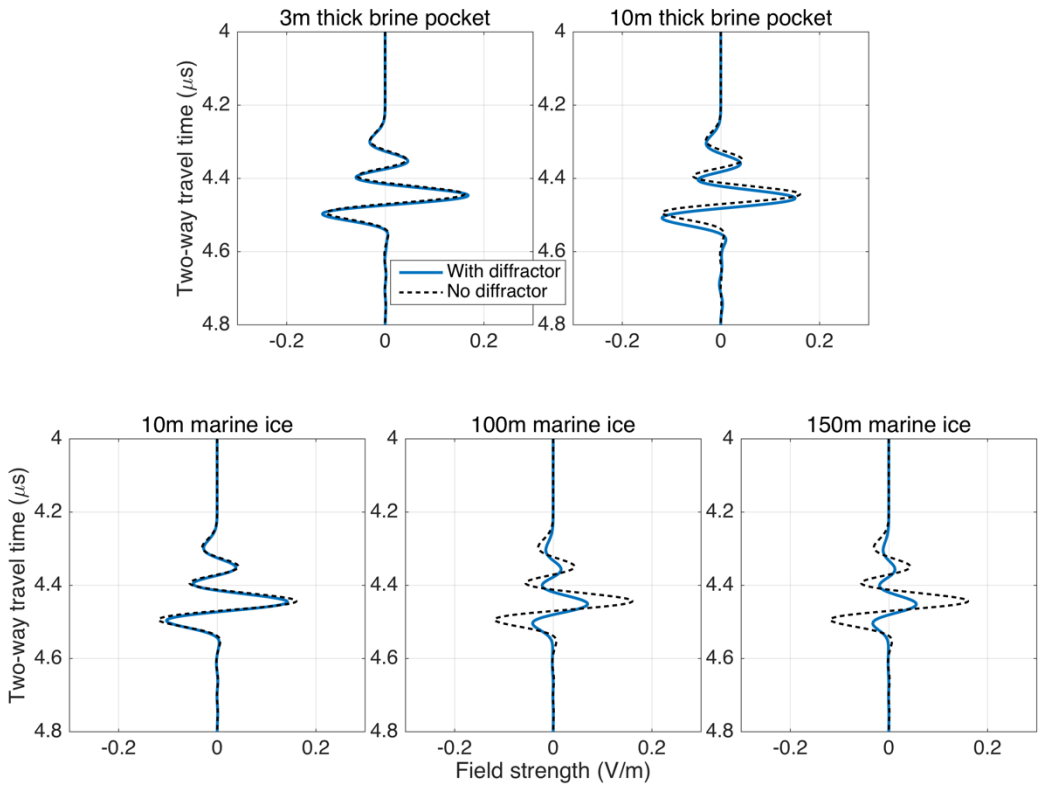

Figure 3-10: Modeled 7 MHz radar returns from the bed beneath the diffractor (blue) for each of the scenarios depicted in Figure 3-8. Dashed black curves show the bed reflection for a control run without a diffractor. The bed echo beneath the 10m-thick brine pocket is delayed because the high permittivity (low wave speed), and there is a ~20% decrease in the amplitude of the reflection. The bed reflections beneath the taller marine ice columns are diminished by 50-70%, with no strong delay of the bed return.

3.5 Discussion

3.5.1 *Origin of the bright reflector (Layer A)*

We can make inferences about the origin of Layer A based on the fact that Layer A is a strong reflector compared to other internal reflection horizons, but dim compared to the bed reflection and the diffraction hyperbolae. Marine sediments and rock fragments recovered from

beneath the ice, along with temperatures measured at the ice-bed interface suggest the basal material is frozen till (Bindschadler et al., 1990; Scherer, 1988). Frozen tills likely have a wide array of dielectric constants based on ice content, further complicated here by the fact that these sediments were saturated with seawater before freezing. The salinity of the ice that would be formed by freezing of these sediments is not known, and thus it is difficult to compute a dielectric constant. However, a frozen till with 40% groundwater by volume has a relative permittivity ε =2.9 (Christianson et al., 2016). Thus, because the reflection from Layer A is weaker than from the bed, its relative permittivity is likely within about 10% of that of glacier ice (ε_i =3.2).

We interpret the Layer A to be a chemically distinct layer caused by flooding of the firn layer with seawater during the ice-shelf flow stage. The coincidence of the layer with the strong diffractors caused by former basal crevasses or rifts filled with marine ice supports this interpretation. The basal crevasses that were high enough to reach the firn-ice transition allowed horizontal percolation of seawater through the firn. Horizontally extensive brine layers are well-documented in ice shelves, including the Ross and adjacent McMurdo ice shelves (Dubrovin, 1960; Clough, 1973; Thomas, 1975; Neal, 1979; Campbell et al., 2017). In some cases, the brine layer reflects or absorbs the transmitted power completely and precludes mapping of the ice-shelf base. In other cases, the brine layer does not completely attenuate the signal, likely due to the brine freezing in pockets rather than as a continuous layer. Spatial variations in firn-layer permeability — and thus in the connectivity of the brine layer — could be the reason why Campbell et al. (2017) were able to image the base of the McMurdo ice shelf through some parts of the active brine layer and not others.

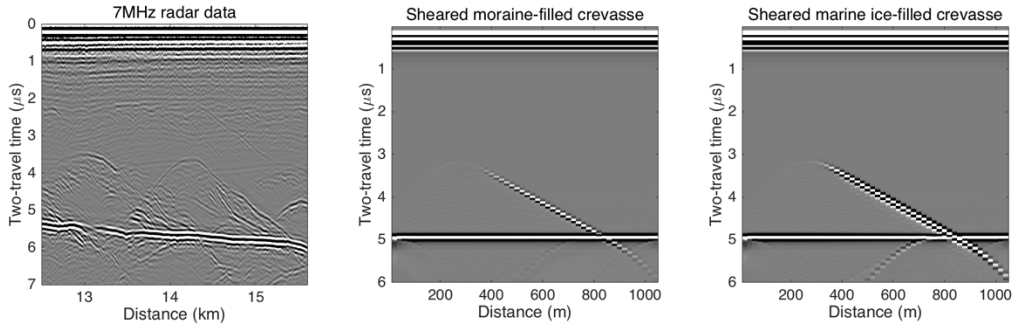

Figure 3-11: Hypothesized sheared basal crevasses in profile B-B' (Figure 3-3) compared to the results of the gprMax model. Here we have modeled the crevasses as filled with basal moraine (center panel), and marine ice (right panel). Based on our modeling, we cannot distinguish between crevasses that may contain basal moraine material and those that contain marine ice, unless the timing of the bed return is changed significantly by the decrease (basal moraine) or increase (marine ice) in permittivity relative to glacier ice.

3.5.2 *Marine ice deposition in former ice shelf factures*

Our RES surveys reveal that Crary Ice Rise contains abundant marine ice, which presumably accreted within rifts and basal crevasses in the Ross Ice Shelf. The tops of ice shelf rifts fill with snow, sea ice, and icebergs, while marine ice accretion within rifts occurs from the top downwards as melting of the rift walls drives convection (Khazendar and Jenkins, 2003). The freezing-point dependence on pressure causes supercooled water to refreeze at shallower depths (Lewis and Perkin, 1986). The down-warping of internal reflectors towards the marine ice columns in our radar profiles suggests that significant melt occurred in the same vertical column as marine ice accretion. In some cases, this may have been along the lower portions of rift walls, as in the model of Khazendar and Jenkins (2003). However, our data show many instances where marine ice deep in the ice column is overlain by continuous reflectors below Layer A (e.g., at 5 km in Figure 3-2). These must be due to accretion of marine ice within basal crevasses that did not penetrate the whole ice thickness, rather than in rifts. Because these features are also accompanied

by downward deformation of the reflectors above them, the fractures may have been caused by large deviatoric stresses at the apex of melt channels in the base of the ice shelf (Vaughan et al., 2012).

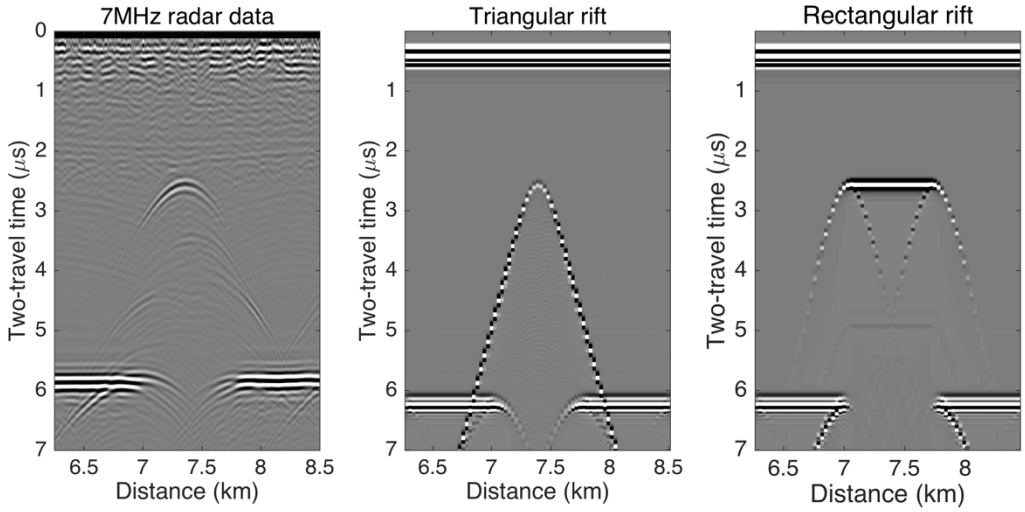

Figure 3-12: Hypothesized former ice shelf rift healed by marine ice accretion. 7MHz radar data are shown on the left, with 2D gprMax model output using an idealized geometry shown in middle (triangular rift) and righthand (rectangular rift) panels. The triangular model better reproduces the main characteristics of the radargram, including the dimming and dipping of the bed echo due to attenuation and the slower wavespeed in marine ice, the hyperbola originating at the top of the rift, and the hyperbola originating at the base of the rift where it contacts the ice sheet bed. However, the model shows strong returns from the crevasse walls, which are not seen in the data. The true geometry could be more complex. The rectangular rift in the righthand panel is inconsistent with the data because of the twin hyperbola originating at the top corners.

Thick layers of marine ice accrete at the bottom of ice shelves, with maximum thicknesses of up to 190 m beneath the Amery, 140 m beneath the Filchner, and 350 m beneath the Ronne (Fricker et al., 2001). However, accreted marine ice is <10 m thick at the base of the modern Ross Ice Shelf (Neal, 1979; Zotikov et al., 1980), and we do not detect a continuous basal layer in our data. Stripes of marine ice accreted in former basal crevasses have been documented in icebergs calved from the Amery Ice Shelf in East Antarctica (Warren et al., 1993; 2019). The marine ice in

these icebergs was found to be rich in organic matter and iron, indicating active biology beneath the ice shelf. The ancient marine ice within Crary Ice Rise could thus hold clues to biological conditions below the Ross Ice Shelf a millennium ago.

The marine ice that formed in ancient rifts and basal crevasses at Crary Ice Rise may have played an active role in the evolution of the ice rise by binding the grounded ice to the ruptured shelf. Marine-ice accretion within rifts can bind together either side of the rupture, which strengthens and consolidates the ice shelf (Rignot and MacAyeal, 1998). The role of marine ice in strengthening ice shelves has been documented at the Brunt/Stancolm-Wills and Larsen C ice shelves (Khazendar et al., 2009; Holland et al., 2009; Jansen et al., 2013). Marine ice in rifts has likely prevented the Larsen C ice shelf from disintegrating in the same fashion as the Larsen B (Kulessa et al., 2014). At Crary Ice Rise, it would have connected the grounded ice rise with the ice shelf across shear and rift zones without inducing more fracturing (Jansen et al., 2013). Marine ice binding the ice shelf to the ice rise could have prevented rift propagation, protecting the integrity of the ice shelf (Larour et al., 2004). This could have prevented the overturning of rift-bounded blocks that would have further damaged the ice shelf, though it is apparent from the exposure of sediment-rich ice (presumably formerly basal ice) on the surface that some block overturning has occurred near the ice rise (Gaylord and Robertson, 1975).

3.5.3 *Evolution of Crary ice Rise*

The structure of Crary Ice Rise revealed by our radio echo sounding is consistent with close coupling between the ice rise and the Siple Coast ice streams. Here we describe the evolution of the ice rise in the context of ice stream fluctuations presented by Catania et al. (2012). Prior to the formation of the ice rise, the Whillans Ice Stream grounding line upstream of the ice rise, and the Ross Ice Shelf extended over what is now Crary Ice Rise. Prior to 1 kyr BP, the ice shelf grounded

over Crary Ice Rise and began to freeze to the bed, producing a shear margin between grounded and floating ice in what is now the central plain of the ice rise. This increased buttressing against Whillans and Mercer Ice Streams, which could have contributed to eventual stagnation of the Whillans Ice Stream about ~860 yr BP. The streaming ice at the boundary of Crary Ice Rise consequently slowed and froze to the bed, allowing the deactivated shear margin to be buried by conformable layers of meteoric ice. At this point the grounding line of Whillans Ice Stream was still far upstream of Crary Ice Rise. When Whillans Ice Stream reactivated ~450 yr BP, the grounding-line advanced to join up with Crary Ice Rise, forming the Whillans Ice Plain.

The surface lineation in the MODIS imagery resembles others on the Siple Coast that are taken as demarcations between ice of different origins (Catania et al., 2005). Radar profiles across a similar lineation on the flank of Engelhardt Ice Ridge suggest that the ice there was once afloat, or nearly so (Catania et al., 2006). Thus, it is possible that the surface lineation is an expression of a former grounding line. The increase in the spatial density of marine ice-filled crevasses downslope of the lineation supports this hypothesis (Figure 3-5). This would imply that the ice shelf grounded over the deep southwestern ridge first (as proposed by Bindschadler et al., 1990), and afterwards the stress regime in the ice that remained floating would have changed considerably. This would have superimposed a new basal crevasse pattern over the existing pattern, which is a likely explanation for the high spatial density and irregularity of the basal crevasses in the central plain of the ice rise. However, the ice in this area is only 50-60 m above floatation (Figure 3-7). Assuming no major isostatic changes in the bed or changes in local sea level over the past millennium, this represents 400-500 years of accumulation at the estimated local rate of 12 cm/yr ice equivalent (Bindschadler et al., 1989). This timescale is slightly younger than the grounding event at the shallow northeastern ridge ~600 years ago calculated from

modeling of borehole temperature profiles (Bindschadler et al., 1990). However, because of the uncertainty in the modeled age, the surface mass balance, and ice velocity and strain rates through time, we cannot distinguish which direction the grounding line migrated across the ice rise during the second grounding event. Because the bed topography is highest under the shallow ridge, it seems likely that the ice shelf grounded there before contacting the bed in the central plain of the ice rise. But there are no discernible clues in the englacial stratigraphy to inform about this process.

Height above floatation could be a good indication of the timing at which the ice re-grounded in these areas. A straightforward series of events based on this reasoning would be: (1) the ice shelf grounds at the main ridge, (2) the ice shelf freezes to the shallower ridge, causing (3) the central plain to stagnate and ground. Finally, (4) the increased buttressing from the grounding of Crary Ice Rise causes the Siple Coast grounding line to advance, creating the neck between the Whillans Ice Plain and Crary Ice Rise. Of course, many factors could complicate this interpretation, but this sequence of events is consistent with our observations.

Bindschadler et al. (1990) were unable to match one of their measured temperature profiles with their model without assuming the persistence of liquid water at the bed after the grounding event. The large volume of marine ice within the ice shelf that we have found here could be another explanation. An ice shelf with a large amount of recently frozen marine ice will be warmer throughout the region penetrated by these basal crevasses. Because marine ice seems to have been accreted up to several hundred meters from the bed at Crary Ice Rise, a thick region of basal ice may have been warmer than the steady-state ice shelf profile used as an initial condition for the temperature modeling by Bindschadler et al. (1990).

3.6 CONCLUSIONS

We have mapped englacial structures and bed topography across Crary Ice Rise using two ice-penetrating radar systems operated at 7 MHz and 750 MHz center frequencies, respectively. We mapped a bright reflector that is present at ~200 m depth across parts of the ice rise. The origin of this bright reflector remains uncertain, but it is possible that it is caused by seawater that percolated horizontally into the firn column during ice shelf flow. Strong diffractors frequently originate at this layer, many of which attenuate radar waves and completely mask the bed reflection. Waveform modeling confirms that basal crevasses filled with frozen marine ice extending hundreds of meters above the bed are consistent with the features detected in our radar data.

We have confirmed that Crary Ice Rise formed as the Ross Ice Shelf grounded over a bathymetric high. This is consistent with the histories inferred by Bindschadler et al. (1990), Fahnestock et al. (2000), and Hulbe & Fahnestock (2004; 2007). Marine ice formation within rifts may have acted as a binding agent (Khazendar et al., 2009) to increase dynamic coupling between the ice rise and the surrounding shelf. This could have linked the evolution of the ice rise, ice shelf, and the ice streams in the Ross Embayment.

3.7 ACKNOWLEDGEMENTS

This work was supported by U.S. NSF grant 1443356 to HC and MRK, and grant 1443552 to JPW. We thank Maurice Conway for assistance in the field. We also thank Antarctic Support Contract, the U.S. Air National Guard, and Ken Borek Air for logistical support. The 750MHz radar was provided by the Center for Remote Sensing of Ice Sheets (CRESIS) and UNVACO provided GPS equipment. This work has benefited from discussions with the University of

Washington Glaciology Group — especially Ed Waddington, Knut Christianson, John Stone, and Nick Holschuh — and additional discussion with Joseph MacGregor, Jonathan Kingslake, and Martin Wearing.

Chapter 4. WEST ANTARCTIC ICE SHEET FLUCTUATIONS DURING PLEISTOCENE INTERGLACIALS

Trevor Hillebrand, Perry Spector, John Stone, David Pollard, Joel Gombiner

4.1 ABSTRACT

Cosmogenic nuclide concentrations in the first deep subglacial bedrock core taken from beneath the West Antarctic Ice Sheet at the Pirrit Hills reveal that local ice has not thinned ≥ 150 m relative to present for at least the last 2 million years. This result is potentially a significant constraint on minimum ice sheet volume during the Pleistocene epoch, but its significance for the whole ice sheet must be examined with an ice flow model. We present a large ensemble of 270 separate ice sheet model runs of West Antarctica that simulate the three strongest interglacials of the Pleistocene using 90 different parameter combinations. We find that all parameter combinations predict significant exposure of the subglacial bedrock core during at least one interglacial period, which is inconsistent with the long burial history inferred from nuclide measurements. Continuous burial of the core requires that the large ice shelves do not fully collapse during interglacial periods in the model. This single point measurement is consistent with multiple modeling frameworks that predict 0 to 3 m of West Antarctic Ice Sheet contribution to interglacial sea level rise, provided the Filchner-Ronne Ice Shelf remains stable.

4.2 INTRODUCTION

The West Antarctic Ice Sheet (WAIS) could drastically retreat under future climate warming scenarios, leading to up to 1 m of global mean sea level rise by 2100 (DeConto and Pollard, 2016). However, the West Antarctic contribution to past sea level fluctuations is poorly

constrained (Dutton et al., 2015). Recent analyses of bedrock recovered from a depth of 150 m beneath the modern WAIS at the Pirrit Hills (Figure 4-1, Figure 4-2) preclude exposure of the site during past interglacial periods for at least the last 2 Myr (Stone et al., 2017). We model the WAIS through three "super-interglacial" periods that are likely candidates for ice sheet collapse and possible analogues for future climates: Marine Isotope Stages (MIS) 31, 11, and 5e. We take a large ensemble modeling approach to this problem, as few direct constraints on WAIS volume and geometry exist for these periods.

The results from the subglacial RB-2 core at the Pirrit Hills suggest that the WAIS could be less sensitive to interglacial climates than previously suggested (cf. Scherer et al., 1998; Pollard and DeConto, 2009; DeConto et al., 2012). However, point measurements of ice thickness history are currently too sparse to rule out grounding-line retreat into marine basins. The fundamental challenge presented by such geological measurements are that areas most directly affected by marine ice sheet collapse would either be (a) under water during interglacial periods, and thus show no cosmogenic or optical evidence of exposure, or (b) be eroded by thick, warm-based ice. Thus, it is necessary to sample rock in locations above sea-level where the ice sheet would have thinned during WAIS collapse, but where the ice sheet has likely been cold-based and non-erosive for at least the entire Pleistocene (Spector et al., 2018). The goal of this paper is to establish the relationship between ice thickness at the Pirrit Hills and the stability of marine basins of West Antarctica. We seek to understand what can be stated with confidence on the scale of the WAIS from such high-precision, low spatial resolution measurements.

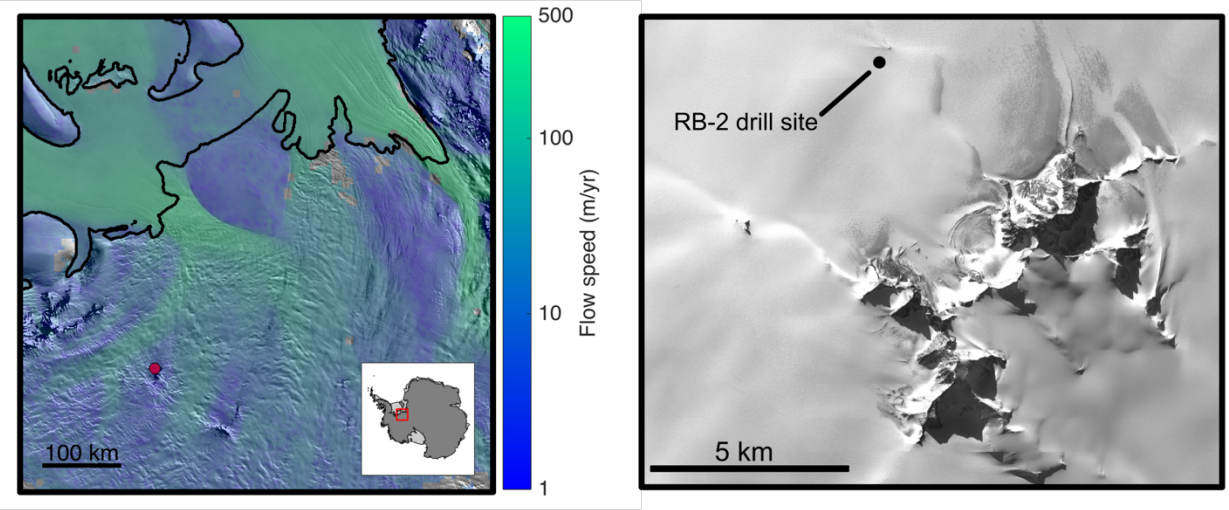

Figure 4-1: (a) Location of the Pirrit Hills (red dot) in the Weddell Sea Sector of Antarctica. Ice flow speed from (Rignot et al., 2011); grounding line is shown as a thick black curve. Plotted using Antarctic Mapping Tools for Matlab (Greene et al., 2017b). (b) Closeup of the white box in (a). WorldView image (copyright DigitalGlobe, Inc.) of the Pirrit Hills, after Spector et al. (2018). The RB-2 drill site is several km from the main massif of the Pirrit Hills, on the subglacial flank of Hater Nunatak.

Below we briefly review the paleoclimate evidence for ice sheet collapse during each of the interglacial periods examined here. Table 4-1 summarizes the main characteristics of each period.

4.2.1 *MIS 31*

MIS 31 (1.08 – 1.06 Myr BP) may have been among the longest and warmest of the Pleistocene (DeConto et al., 2012), but climate and ice-sheet behavior are poorly characterized. Low $\delta^{18}O$ values in the LR04 benthic record (Lisiecki and Raymo, 2005) and the very strong insolation maxima (Laskar et al., 2004) suggest it is a prime candidate for collapse of the WAIS due to warm ocean temperatures, but few of studies have aimed to resolve this period in the Antarctic. Eustatic sea level during MIS 31 is essentially unconstrainted, and the model few

estimates that exist range from changes of 0 – 20 m relative to present (Bintanja and Van de Wal, 2008; Raymo et al., 2006). There are no geologic constraints on these model estimates due to poor preservation and challenges in radiometric dating of sea-level indicators prior to MIS 11 (~400 kyr BP) (Siddall et al., 2007). Marine geologic evidence from the Antarctic margin suggests surface waters 3-5 °C warmer than present, with little to no summer sea ice in the Ross Embayment and a smaller-than-present or absent Ross Ice Shelf (Scherer et al., 2008; McKay et al., 2012). Ice sheet modeling using parameterized climate has simulated large-scale collapse of the WAIS during MIS 31, with an open seaway connecting the Ross, Amundsen, and Weddell Seas through the center of West Antarctica (DeConto et al., 2012).

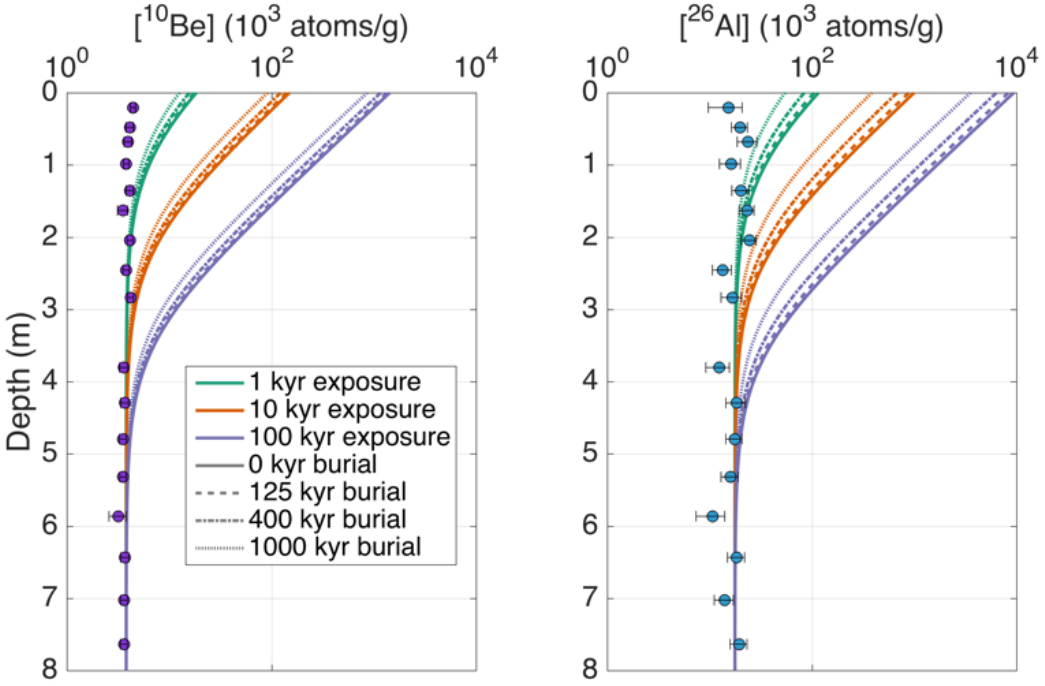

Figure 4-2: Cosmogenic nuclide concentrations in the RB-2 drill core (data points), with modeled exposure and burial histories for comparison. The measured concentrations rule out even 1 kyr of exposure followed by 1 Myr of burial. The vertical profiles are consistent with millions of years of slow accumulation due to muon capture beneath ~200 m of ice.

4.2.2 *MIS 11*

Benthic $\delta^{18}O$ values and climate models suggest a prolonged period of minimal continental ice cover during MIS 11 (~410 kyr BP) when insolation values were very close to those calculated for the late Holocene and the future (5 kyr BP – 60 kyr AP) (Loutre and Berger, 2003; Laskar et al., 2004; Lisiecki and Raymo, 2005). This 28 kyr-long period is the longest interglacial of the past 800 kyr (EPICA Community Members, 2004), and peak eustatic sea level may have been 6-13 m higher than present day (Raymo and Mitrovica, 2012), of which 4.5-6 m may have come from the Greenland Ice Sheet (Reyes et al., 2014). This leaves the contribution of the WAIS to MIS 11 sea level poorly constrained. Antarctic temperatures inferred from ice cores were 2-3 °C warmer than present (Jouzel et al., 2007). However, marine sediments from the Ross Embayment suggest that the Ross Ice Shelf was at least as large as present during this period (McKay et al., 2012).

4.2.3 *MIS 5e*

Global mean sea level was 6-9 m higher during MIS 5e (~125 kyr BP) (Dutton and Lambeck, 2012; Dutton et al., 2015), with 0.6 – 3.5 m sourced from the Greenland Ice Sheet (NEEM community Members et al., 2013; Stone et al., 2013). These estimates require almost complete deglaciation of the marine basins of West Antarctica, but there is to-date no definitive evidence from Antarctica that the MIS 5e WAIS was smaller than the modern. There is evidence that the Ross Ice Shelf was close to its modern size or larger during MIS 5e (McKay et al., 2012). Antarctic and Arctic surface temperatures were 4-5°C and 4-8°C warmer than preindustrial, respectively (Capron et al., 2014), while global mean temperatures were ≤ 1°C warmer (Dutton et al., 2015). Results from multiple ice sheet models suggest that an ocean temperature increase of 2-3°C could have led to complete deglaciation of the marine basins of West Antarctica (DeConto and Pollard, 2016; Sutter et al., 2016). However, ocean temperatures during MIS 5e are highly

uncertain: modeled sea surface temperatures are generally close to modern, while proxy data suggest warming of 3.9 ± 2.8 °C relative to modern (Capron et al., 2014). Thus, while the sea level record suggests WAIS collapse during MIS5e, it is unknown whether the ocean was warm enough to cause substantial retreat of the WAIS relative to present.

Table 4-1: Summary of the main characteristics of three interglacial periods examined in our model ensemble.

Interglacial	**Time range**	**pCO_2 (ppmv)**	**Eustatic sea level above modern (m)**
MIS 31	1.08 – 1.06 Ma (DeConto et al., 2012)	~300 (Hönisch et al., 2009)	Unconstrained; model estimates range from 0 to 20 (Bintanja and Van de Wal, 2008; Raymo et al., 2006)
MIS 11	424–395 ka (Raymo and Mitrovica, 2012)	286 (Lüthi et al., 2008)	6-13 m (Raymo and Mitrovica, 2012)
MIS 5e	130-115 ka (NEEM community Members et al., 2013)	287 (Lüthi et al., 2008)	6-9 m (Dutton et al., 2015)

4.3 METHODS

Here we approach the problem of past WAIS deglaciations using a large ensemble of ice sheet model runs, similar to that of Pollard et al. (2016). We explore the sensitivity of the WAIS to unknown glaciological parameters as prescribed in the ice-sheet model by varying their values over as wide a range as can be reasonably justified. However, unlike the work of Pollard et al. (2016), we lack constraints on ice-sheet geometry for the time periods examined. Furthermore, because we focus on times that the ice sheet may have been smaller than present, all evidence of such geometries either lies beneath the modern ice sheet, or must be inferred from indirect evidence

such as sea level fingerprinting (Hay et al., 2014), ice core records, geochemical tracers, and marine stratigraphy (McKay et al., 2012).

We use the hybrid Pennsylvania State University (PSU) ice sheet-ice shelf model to simulate the Antarctic Ice Sheet. The model uses scaled equations for ice sheet and ice shelf flow in three dimensions, along with offline climate and ocean forcings that allow for long-term transient runs (Pollard and DeConto, 2012a). Coupled ice sheet model forcing using global or regional climate models (GCMs; RCMs) is reserved for future work due to computational expense. Basal sliding coefficients are determined by a simple inverse method that minimizes the misfit to modern ice thicknesses and velocities (Pollard and DeConto, 2012b); these values vary in space but are held constant through time. Because the basal sliding estimation only works for the portions of the ice sheet that are currently in contact with the ice sheet bed, we must prescribe this parameter on the continental shelves to be applied when the ice sheet advances during glacial periods (David Pollard et al., 2016). In reality, this value is unlikely to be constant in time or space, but the simplest assumption given the lack of constraints is to hold it constant.

As in previous work (Gomez et al., 2013; Pollard et al., 2016), ocean temperatures are from a 20 kyr BP-to-present run of the National Center for Atmospheric Research Community Climate System Model version 3 (NCAR CCSM3) coupled atmosphere-ocean general circulation model (Liu et al., 2009). Modeled ocean temperatures are mapped linearly onto the contemporaneous LR04 $\delta^{18}O$ value and are applied as forcing to the ice sheet model based on the $\delta^{18}O$ value at each timestep. We use the modeled temperature at 400 m depth, in order to account for the incursion of Circumpolar Deep Water beneath ice shelves, which is responsible for most sub-ice shelf melt (Hellmer et al., 2012). We acknowledge that this could over-estimate ice shelf melt, as the base of the ice shelf is not always 400 m below sea level. Ice shelf melt is calculated using a quadratic

function of the difference between the ocean temperature and the pressure-melting point at the bottom of the ice shelf (Holland et al., 2008).

Sea level, surface temperature, and accumulation are treated as described in Pollard and DeConto (2012b), and are summarized here. Eustatic sea level is taken to be proportional to the benthic oxygen isotope stack of (Lisiecki and Raymo, 2005), with modern $\delta^{18}O$ values corresponding to modern sea level and Last Glacial Maximum $\delta^{18}O$ values set to -125 m relative to present (Pollard and DeConto, 2012a). An updated sea-level curve exists (Spratt and Lisiecki, 2016), but does not include MIS 31, and so we use the LR04 stack for consistency between our model runs. Modern surface temperatures and accumulation rates are taken from the ALBMAP compilation (Le Brocq et al., 2010) and prescribed to change over time using climate variations based on the LR04 stack and insolation from Laskar et al. (2004).

We first ran the model over the last 1.2 Myr at a coarse resolution of 40 km for the whole Antarctic continent (i.e., both East and West Antarctic Ice Sheets) using the optimized ice-sheet model parameter set from Pollard et al. (2016), which covered only the last deglaciation. We then used this run to initialize 40-km resolution runs over the time-periods in question for each combination of model parameters, with a 100-200 kyr spin-up period to avoid effects of hysteresis from the default run. These runs establish initial conditions and time-varying boundary conditions (velocity, temperature, bed topography, ice thickness) for subsequent nested simulations at 20-km resolution over a domain that includes the entire WAIS, as well as the Ross and Filchner-Ronne ice shelves and a part of the EAIS (model domain shown in Figure 4-4). While the 40 km resolution provides a crude representation of ice dynamics, it only affects ice entering the WAIS domain from the EAIS, which is much less dynamic than West Antarctic ice because it is grounded above sea

level. We include the entire WAIS grounding-line in our nested domain to avoid numerical instabilities arising from the low-resolution model at the boundaries.

We vary five parameters in order to gauge the sensitivity of the ice sheet at the Pirrit Hills to deglaciation of marine basins, in the absence of sufficient physical or proxy constraints. Justifications of parameter choices are given below, and the parameters and their values are listed in Table 4-2.

Table 4-2: Parameter values chosen for the large ensemble. All combinations were used, with the exception of combining zero and non-zero values of CLIFFV and CALVL, which have been shown to have little effect when included separately (Pollard et al., 2015).

Parameter Name	**Explanation**	**Values**
TAU	Lithospheric rebound timescale (yrs)	1,500; 3,000
OCFAC	Sub-shelf melt factor	0.5; 1; 2
CRHSHELF	Basal traction on continental shelf	4, 5, 6
CLIFFV	Maximum cliff backwasting velocity (km/yr)	0, 3, 10
CALVL	Ice shelf hydrofracture coefficient	0, 50, 100

4.3.1 *Lithospheric rebound timescale*

In the absence of a 3D earth model, we apply an elastic response e-folding timescale to treat isostatic adjustment due to changing ice loads. The elastic response timescale of the lithosphere does not significantly affect the behavior of a model ensemble of the last deglaciation of the WAIS (Pollard et al., 2016); however, that analysis did not involve the ice cliff failure or ice shelf hydrofracture mechanisms (Pollard et al., 2015) that are included here. It is possible that the timescale of rebound could have a nonlinear relationship with these mechanisms — re-grounding of an ice shelf on a bathymetric high could prevent the process of hydrofracturing from

entirely removing an ice shelf and invoking the marine ice cliff failure mechanism. We choose glacial isostasy rebound timescales of 1.5 and 3 kyr because these received approximately equal scores in the large ensemble analysis of Pollard et al. (2016).

4.3.2 *Sub-shelf melt factor*

Ocean-driven melt beneath ice shelves is a complex process that cannot be explicitly modeled in long-term ice sheet model runs due to computational limitations. However, ice sheet model results have been shown to be strongly dependent on melt beneath ice shelves (DeConto et al., 2012; DeConto and Pollard, 2016). Proxy-based ocean temperature reconstructions have high uncertainties and data sparsely sample space and time (Capron et al., 2014). While models supply better resolution, they tend to produce lower sea surface temperatures than do proxy reconstructions. We explore this uncertainty by changing the ice sheet model's sensitivity to ocean temperature, rather than by adjusting the temperature field. We use 50%, 100%, and 200% of the optimized value for melt response to ocean temperature. The PSU ice sheet model parameterizes sub-shelf melt differently for different sectors of the ice sheet in order to match modern grounding-line positions and ice shelf geometries (Pollard and DeConto, 2012a). The variation in melt sensitivities that we impose is independent of sector, but is often less important than these sectoral biases. Future work should explore different scaling for different ice sheet sectors.

4.3.3 *Basal sliding coefficients on continental shelf*

Basal sliding coefficients vary by several orders of magnitude over the spatial extent of the grounded WAIS (Pollard and DeConto, 2012b); however, there is no way to solve for this value where the ice sheet is not currently grounded. While this likely varies in space and time on the continental shelves as well, we assign a uniform value over these areas due to lack of any

constraints or defensible parameterization (e.g., as a function of sediment depth, elevation, etc). We vary the basal sliding coefficient over three orders of magnitude, centered on the best-fit value found by Pollard et al. (2016) for the last deglaciation.

4.3.4 *Maximum cliff backwasting velocity*

The ice cliff failure mechanism has been invoked to explain sea-level high-stands requiring large contributions from the EAIS, such as the mid-Pliocene (Pollard et al., 2015). There is currently no consensus on proper parameterizations for this phenomenon. The existence of a positive feedback resulting from ice cliff failure (i.e., a marine ice cliff instability) has been questioned, due to the lack of observational constraints and the poor constraints on past sea level (Raymo et al., 2018; Edwards et al., 2019). In light of these uncertainties, we impose a simple speed limit on cliff backwasting, following DeConto and Pollard (2016). We choose values of 0 km/yr (no cliff failure mechanism), 3 km/yr, and 10 km/yr, based on observations of cliff failure in Greenland (Joughin et al., 2012). We include cliff failure as an end-member scenario, but in this work we cannot address how it should be properly parameterized.

4.3.5 *Ice shelf hydrofracture coefficient*

Water-filled surface crevasses can hydrofracture through ice shelves, causing them to disintegrate rapidly (Scambos et al., 2009). This in turn quickly reduces the stabilizing buttressing force on grounded ice upstream, causing acceleration and grounding-line retreat (Rignot et al., 2004). In our model formulation, the increase in crevasse depth due to hydrofracture is a quadratic function of surface meltwater availability (Pollard et al., 2015). Because the proper parameterization for this process is unknown, we choose three different coefficients of 0, 50, and

100 to scale the square of water availability. Hydrofracture and cliff failure are impactful when combined, but do not significantly alter results when either is excluded (Pollard et al., 2015); thus, to limit the size of the ensemble, we do not run simulations in which only one process is included.

4.4 RESULTS

4.4.1 *Pirrit Hills ice thickness and ice sheet volume*

Our model results suggest that ice thickness around the Pirrit Hills is a good predictor of the total WAIS volume above floatation (i.e., potential sea level contribution) for all three interglacial periods that we modeled (median r^2 = 0.7 - 0.75) (Figure 4-3). All ensemble members predict retreat from glacial to interglacial ice sheet configurations during the modeled time periods, with a significant spread in predicted ice sheet volume changes for each given interglacial. The shapes of the Pirrit Hills ice thickness timeseries closely follow the shape of total WAIS volume timeseries, with a few notable exceptions. During MIS 11, the Weddell Sector of the ice sheet does not retreat in a small subset of runs with fast rebound timescales and a rigid seafloor. In these runs, the Pirrit Hills ice thickness is not strongly correlated with total ice sheet volume. During MIS 31, another group of runs show only moderate retreat in the Amundsen, while the Weddell and Ross sectors retreat strongly in all simulations. In these simulations, there is very little indication of this discrepancy in the simulated Pirrit Hills ice thickness. This illustrates the strong dependence of Pirrit Hills ice thickness on the position of the grounding line downstream in the Weddell Sector.

In all interglacials, the majority of simulations show ice around the Pirrit Hills thinning well below the amount required to expose the surface of the RB-2 core site (Figure 4-3). While some allowance should be made for the coarse resolution of the ice sheet model relative to the scale of Pirrit Hills, we assume regional ice thickness strongly controls the local ice thickness around the RB-2 drill site. It is unclear whether the appropriate comparison should be between the

modeled modern ice thickness from the optimized parameter set (David Pollard et al., 2016), or the Bedmap2 ice thickness (Fretwell et al., 2013). Thus, we compare against both of these products, re-gridded onto our model grid and bilinearly interpolated to the RB-2 site. Most model runs predict sufficient ice sheet thinning around the Pirrit Hills to uncover the core site during all three interglacials relative to Bedmap2 ice thickness, while comparison with the modeled modern ice thickness leaves the bedrock surface covered for almost all of MIS 11. Thus, we interpret this to mean that the model unequivocally predicts exposure of the RB-2 core during MIS 31 and MIS 5e, while modeled exposure during MIS 11 is undetermined. This amount of exposure (>10 kyr per interglacial) would be readily detected in the nuclide profile if it had occurred (compare with orange curves in Figure 4-2).

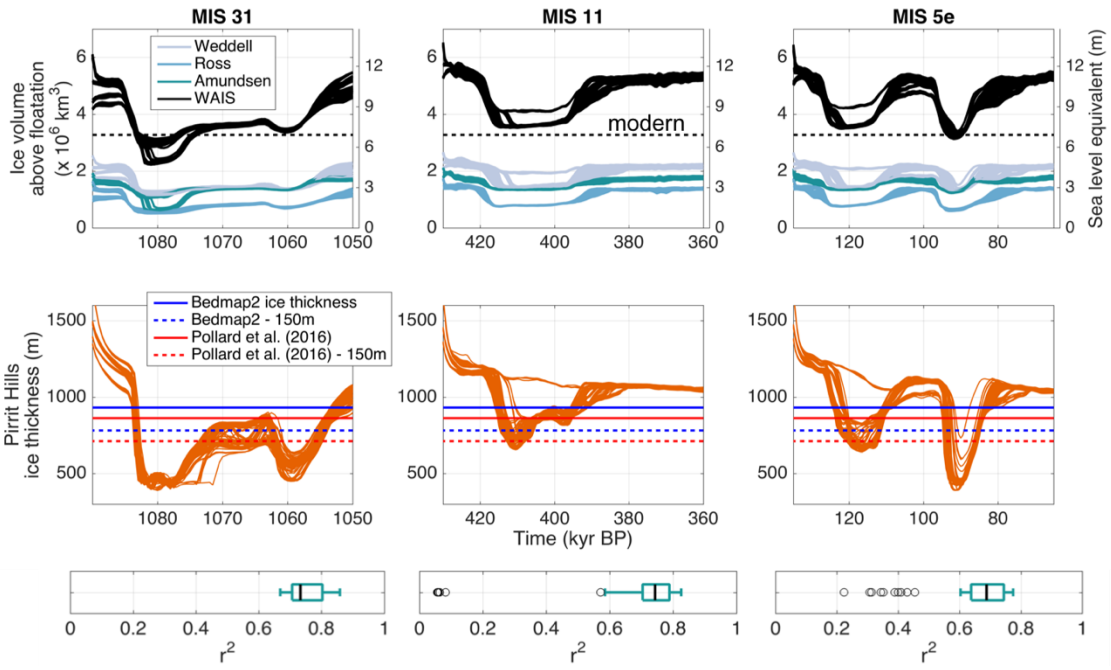

Figure 4-3. Top Row: Ice sheet volume above floatation (and sea level equivalent) for all model runs, separated into the whole model domain and individual sectors defined by static modern boundaries. Middle Row: Pirrit Hills ice thickness in all model runs, by bilinear interpolation of nearest model nodes. Because the Pirrit Hills themselves are not resolved by the ice sheet model grid, we down-sample Bedmap2 ice thickness to the average ice thickness within 5km of the nearest model grid points to calculate modern ice thickness (blue curve). The modeled modern ice thickness by bilinear interpolation from the optimized parameter set of Pollard et al. (2016) is shown in blue. The dashed curves correspond to 150 m of thinning at the RB-2 Pirrit Hills bedrock core site, which is precluded by the cosmogenic nuclide data. Therefore, the modeled large-scale ice sheet drawdown during MIS 31 and MIS 5e contradict the RB-2 core, while many simulations of the MIS 11 interglacial are consistent with the RB-2 core data. Bottom Row: Boxplots of the 90 r^2 values by comparing ice thickness at the Pirrit Hills and WAIS volume above flotation for each interglacial period. Black lines represent the median r2 value for the 90 runs; boxes represent upper and lower quartiles; whiskers show 1.5x the interquartile range; black circles denote outliers. Pirrit Hills ice thickness generally represents around 70% of the variance in total WAIS volume above floatation.

4.4.2 *Minimum ice sheet configurations and ice shelf melt*

Figure 4-4 shows a composite of all 90 ice-sheet model runs for each interglacial in terms of median ice thickness and grounding-line position at the time of minimum ice sheet volume. These median-minimum configurations are significantly smaller than present but do not lead to a full deglaciation of the marine basins. The modeled Ross and Filchner-Ronne ice shelves collapse during MIS 31 and MIS 5e, but they stay intact during MIS 11. As a consequence, the grounded ice sheets during MIS 31 and MIS 5e are much smaller than during MIS 11. The MIS 11 configuration is similar to the modern ice sheet. Based on the results in Figure 4-3 this is likely the dominant control on whether or not the surface of the RB-2 core site is exposed in a given modeled interglacial. The reduction in ice shelf buttressing causes substantial grounding-line retreat, often to within tens of km of the Pirrit Hills.

Two basic behaviors of ice sheet and shelf changes are apparent in the ensemble (Figure 4-5). MIS 11 exhibits a simple trade-off between the ice shelf and grounded ice, with a nearly net-zero rate of change in total ice-covered area (black curve in middle row of Figure 4-5). During the termination of the previous glacial period, the grounding line retreats and the ice shelf grows as a result. The growth of large ice shelves buttresses the grounded ice upstream, and prevents a runaway retreat. The minimum ice sheet volume is thus very close to the modern. MIS 31 and MIS 5e exhibit more complex behavior, in which grounded and floating ice retreat at the same time. As a result of the loss of buttressing, the grounding line retreats further into the interior of the WAIS. Ice shelf regrowth precedes the advance of grounded ice at the end of the interglacial period, consistent with ice-shelf buttressing controlling ice-sheet volume.

Increasing ocean temperatures during interglacial periods drive ice shelf loss in the ensemble (bottom row of Figure 4-5). High levels of average ocean melt of ~2 m/yr sustained for

~5 kyr around West Antarctica consistently cause rapid retreat of grounded and floating ice. The extreme 5-6 m/yr of average ice shelf melt in MIS 31 leads to the lowest ice sheet volumes of the three interglacials, with total collapse of the WAIS for a handful of parameter combinations. The effect of high ocean temperatures and thus high melt rates on ice sheet stability is a common element among different models of WAIS collapse (e.g., Feldmann and Levermann, 2015; DeConto and Pollard, 2016; Sutter et al., 2016).

The model runs that include full WAIS collapse in MIS 31 require a very strong combination of destabilizing parameter values. Collapse only occurs for a doubling of melt sensitivity to ocean temperatures, a long (3 kyr) rebound timescale, active hydrofracture and cliff failure, and a resistant ice sheet bed over the modern seafloor. The resistant bed causes very thick ice to build up on the continental shelves, leading to increased isostatic depression that drives the bed further below sea level. When retreat initiates, the increased ice thickness below sea level causes more rapid marine ice sheet retreat due to the strong dependence of grounding-line flux on ice thickness (Schoof, 2007). The long isostasy timescale ensures that the bed is not able to rebound quickly enough to provide any effective stability. High oceanic melt rates and hydrofracture do not allow ice shelves to grow and buttress the grounded ice, which allows the ice cliff failure mechanism to rapidly remove ice from the grounded margin. The hydrofracture coefficient and maximum cliff retreat rate must be non-zero but need not be large to cause WAIS collapse in the ensemble.

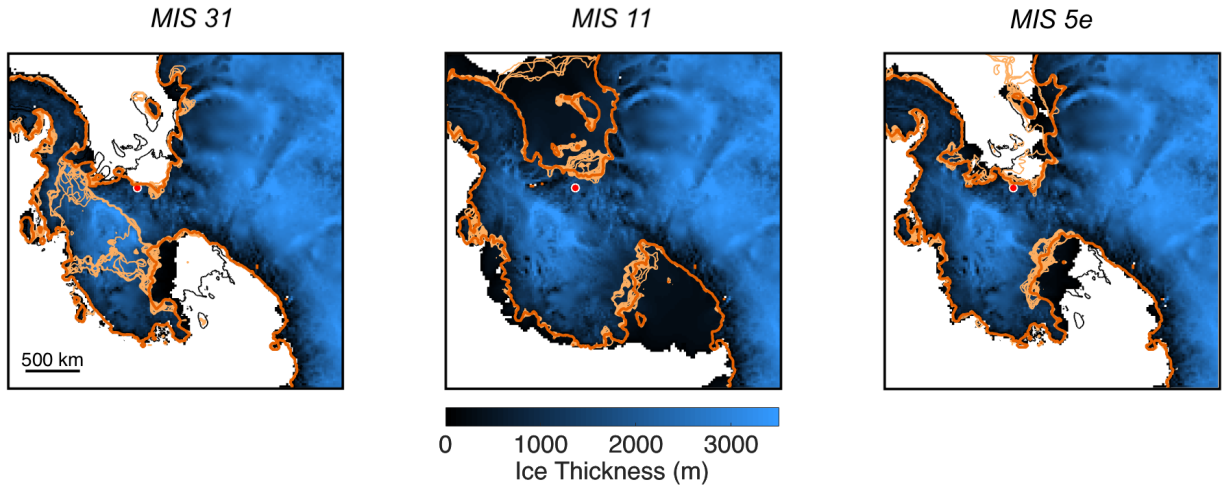

Figure 4-4: Median of minimum volume ice sheet configurations from all 90 ensemble members. The location of the Pirrit Hills is denoted by the red dot. The median minimum grounding line is shown by the heavy dark orange curve. All modeled minimum grounding lines are shown by the light orange curves. The black curve shows the modern grounding line from Fretwell et al. (2013), plotted using the code provided by Greene et al. (2017).

4.4.3 *Controls on Pirrit Hills ice thickness*

The ice thickness at the Pirrit Hills is an excellent predictor of the volume of the Weddell Sector, a good predictor of the volume of the Ross Sector, and a fair to poor predictor of the volume of the Amundsen Sector (Figure 4-6). Pirrit Hills ice thickness consistently predicts >80% of the variance in the volume of the Weddell Sector over all three interglacial periods. The skill in predicting the volume of the Ross and Amundsen sectors varies between interglacial periods. In general, modeled ice thickness at the Pirrit Hills predicts 60 – 80% of the variance in Ross Sector volume above floatation, and 40 – 70% in the Amundsen. The correlation is positive between Pirrit Hills ice thickness and ice sheet (or sector) volume in all cases. Thus, it is likely that major collapse of the WAIS or of any sector would result in a thinning signal at the Pirrit Hills, although retreat limited to the Amundsen sector would be least likely to be detected in the RB-2 core.

Ice thickness fluctuations at the Pirrit Hills are correlated with different mechanisms during the different interglacial periods we examined (Figure 4-6). During MIS 31, the mean and minimum distances to the grounding line in the Ross and Weddell sectors predict most of the variance in ice thickness at the Pirrit Hills, while the Amundsen grounding line position is very weakly correlated with Pirrit Hills ice thickness. During MIS 11, the area and volume of temperate basal ice predict more of the variance in Pirrit Hills ice thickness than does grounding-line position, likely because the grounding line never retreats rapidly in this interglacial. Most power in these fields occurs within the Weddell and Amundsen sectors. In the Ross sector, the volume of temperate ice generally predicts 0 - 10% of the variance in the Pirrit Hills ice thickness, but the area of temperate ice predicts ~50% of the variance. This indicates some control by well-lubricated ice streams, whose flow speed is more strongly dependent on the temperature at the bed than within the ice column (Raymond, 2000).

Ice shelf size is not strongly correlated with ice thickness at the Pirrit Hills because ice shelves generally do not form during the warmer deglaciations. MIS 11 is the only period during which ice shelf volume or area are good predictors for Pirrit Hills ice thickness. This is dominated by the Filchner-Ronne Ice Shelf in the Weddell Sector; the Ross and Amundsen sectors are merely fair predictors during this period, though still better than during MIS 31 or MIS 5e. The calving flux also becomes an important predictor during MIS 11, presumably because of its control on ice shelf size. However, this obscures a strong threshold behavior of ice sheet dynamics in response to ice shelf collapse. During MIS 31 and MIS 5e, the large ice shelves either do not form or collapse rapidly early in the deglaciation (Figure 4-5).

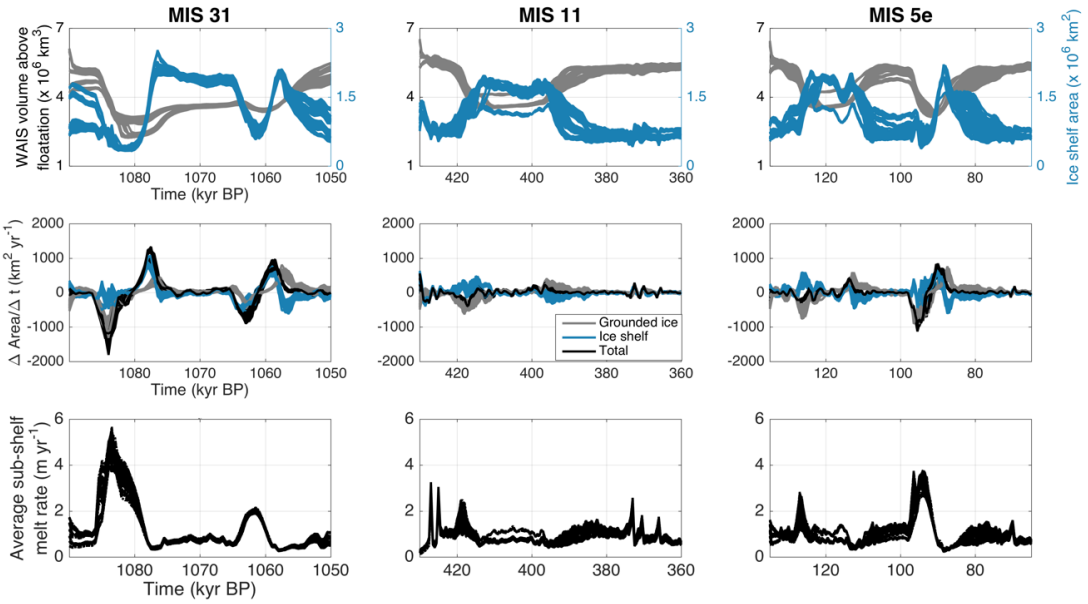

Figure 4-5: Top row: Time-series of grounded ice volume for the WAIS (grey curves) and ice shelf area (blue curves). MIS 11 is the only of the three interglacial periods that exhibits a simple relationship between ice shelf area and grounded ice volume above floatation. Middle row: Time derivative of grounded (grey), ice shelf (blue), and total (black) area for each interglacial period. The total dA/dt during MIS 11 sums to close to zero at each time, while the total magnitude of dA/dt for MIS 31 and MIS 5e is often larger than for grounded or floating ice. This is because the changes are not equal and opposite, revealing a more complicated relationship than for MIS 11. The nearly net-zero change in area during MIS 11 reflects that grounding-line migration traded grounded ice for floating ice at close to a one-to-one ratio. Bottom row: Average sub-shelf melt around the WAIS. High average melt rates of >3 m/yr sustained for several thousand years are needed to cause loss of the ice shelves and large-scale interglacial ice sheet retreat relative to present.

4.5 Discussion

Few ice sheet models are capable of simulating a complete deglaciation of the marine basins of West Antarctica because of the large spatial scales (1000s of km) and long timescales

(1000s of years) involved. Most long-term modeling studies of WAIS fluctuations have been performed with the PSU ice sheet model (Pollard and DeConto, 2009; DeConto and Pollard, 2016; Tigchelaar et al., 2018) or the Potsdam Parallel Ice Sheet Model (PISM; eg., Feldmann and Levermann, 2015; Golledge et al., 2017). These hybrid models have the advantage of being computationally efficient through simplified shallow ice and shallow shelf approximations for ice sheet and ice shelf flow, respectively. The migration of the grounding-line is calculated using the simple 1-D parameterization of flux across the ice sheet grounding-line (Schoof, 2007). These simplifications enable coarse resolution across the grounding line, which greatly reduces the computational expense involved in resolving the grounding line at fine resolution using an adaptive mesh. While this simplification reduces accuracy relative to higher-order models with an adaptive mesh (e.g., Reese et al., 2018), they are necessary in order to simulate continental ice sheets over long timescales. Fully resolved grounding-line position and grounding-line evolution are impracticable for paleoclimate ice sheet applications.

Because of the simplifications and uncertainties inherent in our modeling approach, it is necessary to compare our model results to other models of WAIS fluctuations. Here we compare our results against several long-term models the WAIS:

1. An ocean melt-driven future collapse predicted by Feldmann and Levermann (2015) using PISM (hereafter “PISM collapse”)
2. An 800-kyr simulation driven by the LOVE-CLIM climate model (Goosse et al., 2010) using the PSU ice sheet model (hereafter PSU-LOVE; Tigchelaar et al., 2018).

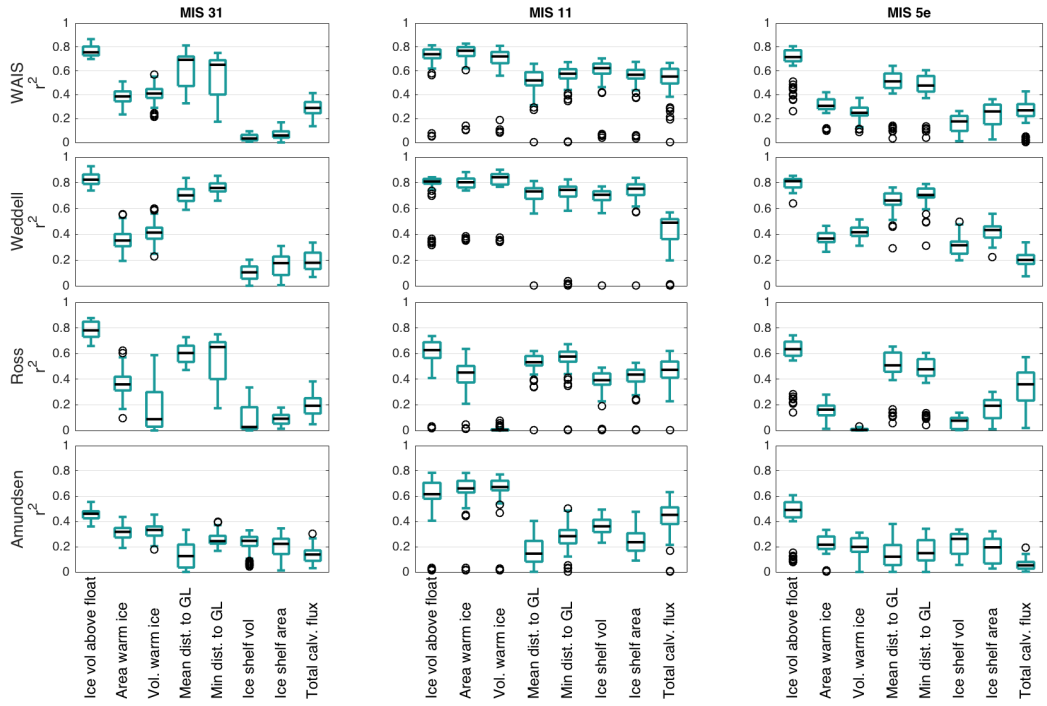

Figure 4-6: Coefficients of determination (r^2, where r is Pearson's correlation coefficient) between ice thickness at the Pirrit Hills and the variables labeled on the horizontal axis. Rows correspond to sectors of the ice sheet, and columns are the interglacial periods over which the model was run. Only variables whose total (i.e., over all three time periods, for the whole WAIS) upper quartile values are greater than 0.45 are shown. Ice thickness at the Pirrit Hills is an excellent predictor (r^2 ~0.8) of the volume of the ice sheet above floatation, both for the Weddell sector and for the whole WAIS. It is an adequate predictor of the volume of the Ross sector, and a relatively poor predictor for the Amundsen Sector.

While these simulations do not overlap with all of our modeled interglacials, the important issue is to compare the response of Pirrit Hills ice thickness to ice sheet changes between different models with different forcings.

The PISM collapse model is run at 5 km resolution and is forced by the Finite Element Sea Ice-Ocean Model (FESOM; Timmermann and Hellmer, 2013) that calculates ice shelf melt. The

melt rates predicted by FESOM closely match observed values of ice shelf melting in the Weddell and Ross Sectors, but melt rates are underestimated in the Amundsen sector. The authors scale modeled melt rates in the Amundsen sector to match the modern values as a perturbation to the model. When modern melt rates are sustained for 60 years and longer, the model predicts full dynamic collapse of the marine basins in West Antarctica. In the 60-year perturbation experiment, a seaway connects the Weddell and Amundsen seas within 6000 model years. This seaway reaches the Ross Sea after 15000 model years. The model lacks an isostatic component, and surface mass balance and temperature are held at modern values reported by Le Brocq et al. (2010). A timeseries of this collapse and the modeled ice thickness changes around the Pirrit Hills are shown in Figure 4-7.

There is no close analogue for this style of ice sheet collapse in our model ensemble. The large Filchner-Ronne and Ross ice shelves remain intact through the PISM collapse because there is no perturbation to the melt rates in the Weddell and Ross Sectors. This results in ice thickness changes at the Pirrit Hills of ~30 m, which is nowhere near enough to expose the RB-2 core above the ice sheet surface. This highlights the sensitivity of ice thickness around the Pirrit Hills to the presence of the Filchner-Ronne ice shelf, even when the marine basins of central West Antarctica are free of grounded ice. None of our MIS 31 scenarios that result in a full WAIS collapse leave the Ross or Filchner-Ronne ice shelves intact. The loss of these ice shelves is a prerequisite for the initiation of the marine ice cliff collapse mechanism in our model, which leads to the deglaciation of central West Antarctica from full glacial conditions in <4 kyr.

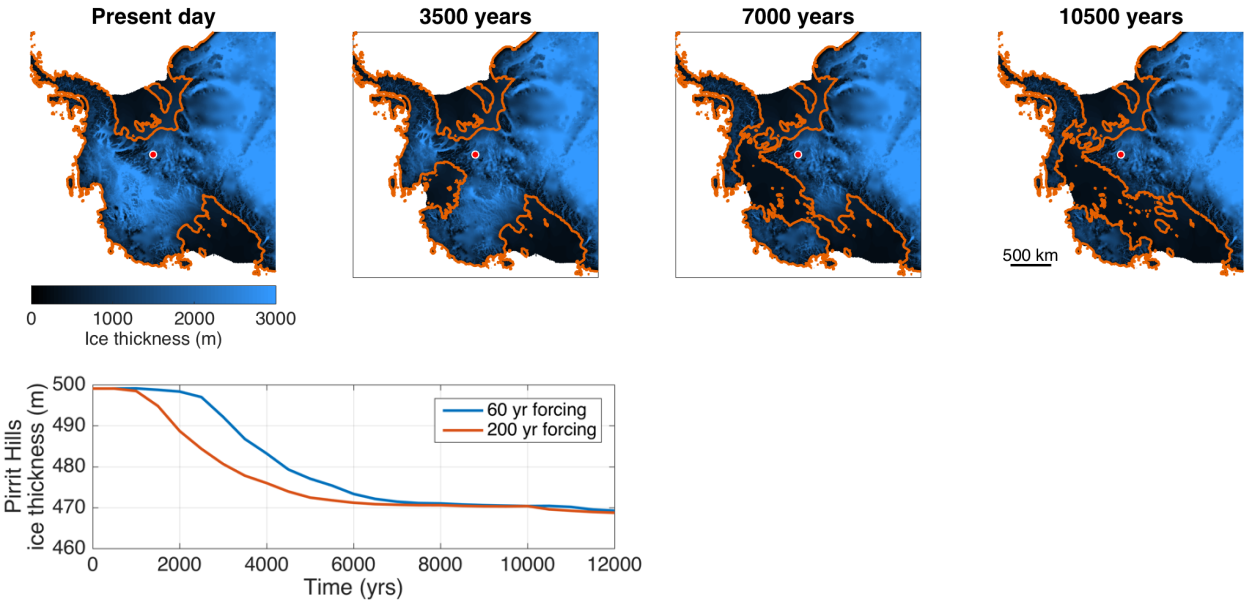

Figure 4-7: Results from the PISM collapse model, modified from Feldmann and Levermann (2015). Ice thickness around the Pirrit Hills only decreases by ~30m, while the ice sheet contributes >3m to global mean sea level. The preservation of the ice shelves in this simulation keeps the Weddell Sea grounding line from retreating, which is a very strong predictor of Pirrit Hills ice thickness in our ensemble.

Our model ensemble is forced by a simpler ocean climatology than that which forces the PISM collapse. However, with the exception of the 20-200 year perturbation in melt rates, both the oceanic and atmospheric boundary conditions are held constant in the PISM collapse experiment. In our model ensemble, melt rates and precipitation change with time, which could provide extra stability to the ice sheet through increased precipitation. At least one study has found that increasing precipitation can delay but not prevent collapse in the Amundsen Sector (Joughin et al., 2014). However, increased precipitation during interglacials in conjunction with isostatic rebound due to the removal of the ice load are important buffers against significant grounding-line retreat. The very low mantle viscosity and rapid isostatic rebound beneath the Amundsen Sector could greatly increase the stability of the ice sheet (Barletta et al., 2018; Larour et al., 2019).

Because the retreating grounding line of the Amundsen Sector takes ~3 kyr to reach the continental interior in the PISM simulation, it is possible that if isostatic adjustment was included in the model it would greatly delay or potentially prevent deglaciation of the marine-based WAIS. We ran a set of experiments (not shown) covering all combinations of melt sensitivity and basal to determine whether a very long isostatic timescale of 100 kyr could lead to WAIS collapse without hydrofracture and cliff failure. We found that our modeled ice sheet is quite insensitive to the rebound timescale when cliff failure and hydrofracture are not included in the model, and the WAIS never fully collapses in these experiments. This should not be taken as a direct comparison with the PISM collapse model because of the different resolutions, initial and boundary conditions, and ocean forcings. However, this confirms that the fundamental difference between our results and the PISM collapse results is not due to isostatic considerations.

The control PSU-LOVE simulation does not predict collapse of the WAIS during the past 800 kyr. Because the ice sheet model is forced by a coupled ocean-atmosphere model, the ocean and atmosphere forcings are not as synchronous as in our ensemble that scales all forcings relative to the LR04 stack. Therefore, minimum ice sheet configurations during MIS 11 and MIS 5e look much like the modern ice sheet (Figure 4-8). The authors amplified the ocean forcing to find the threshold of WAIS collapse, which only occurs with a 5-fold amplification of the modeled sea-surface temperature anomaly at 55°S. This causes complete deglaciation of the marine basins of West Antarctica during MIS 11, but only a slightly smaller ice sheet during MIS 5e. During the simulated MIS 11 collapse, the Pirrit Hills lie essentially at the grounding line.

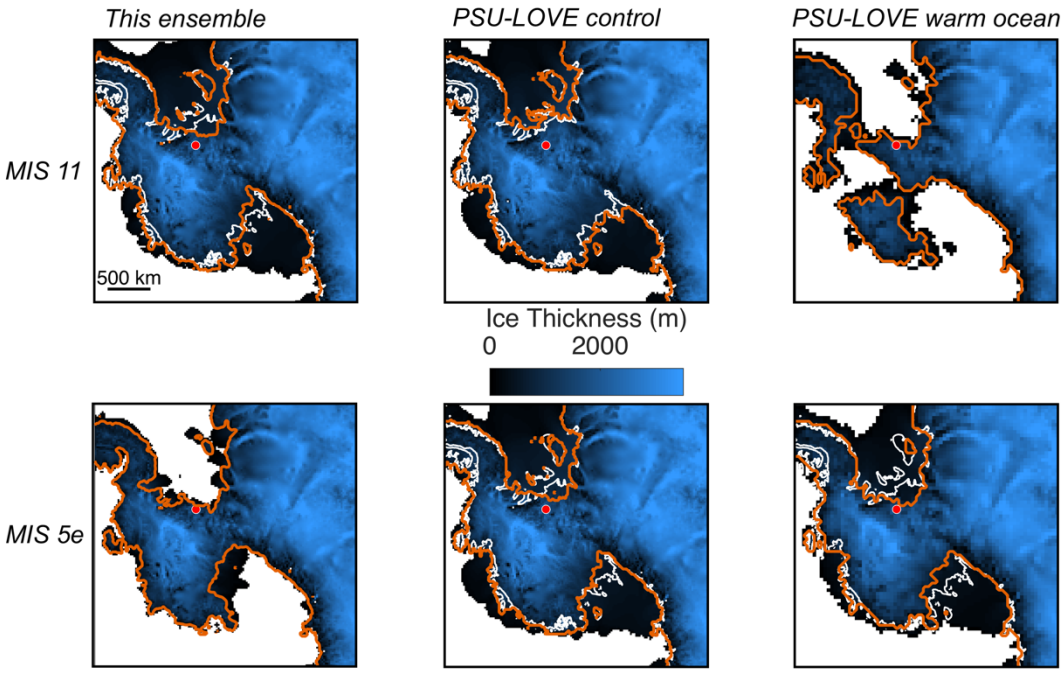

Figure 4-8: Comparison of results from this ensemble (left-hand column) with the experiments of Tigchelaar et al. (2018) for MIS 11 (top row) and MIS 5e (bottom row). Modern grounding line is shown in white where appropriate, while minimum modeled grounding line is shown in orange. The results from this ensemble are the median of ice thicknesses at the time of minimum ice volume, as in Figure 4-4. The 20-km control experiment from Tigchelaar et al. (2018) (middle column) does not cause an ice sheet collapse, and most interglacials are similar to the modern ice sheet. Five-fold amplification of a warm ocean anomaly is required in the PSU-LOVE experiments to cause WAIS collapse at 40-km resolution (right-hand column).

Pirrit Hills ice thickness closely corresponds to ice sheet volume in the PSU-LOVE experiment (Figure 4-9). Their model does not uncover the RB-2 core site during either interglacial in the control run. During the run with amplified ocean forcing, however, the core site is at or near the ice sheet surface for ~10 kyr during MIS 11. This corresponds to a period of sustained average sub-shelf melt of ~4 m/yr around the WAIS. During MIS 5e, the average ice shelf melt due to

amplified ocean forcing never exceeds 2 m/yr, and only leads to modest thinning at the Pirrit Hills relative to modern. The Filchner-Ronne ice shelf remains intact during MIS 5e in the warm ocean experiment, but collapses during MIS 11. This is consistent with our assertion that the ice thickness at the Pirrit Hills is most dependent on the presence of the Filchner-Ronne Ice Shelf.

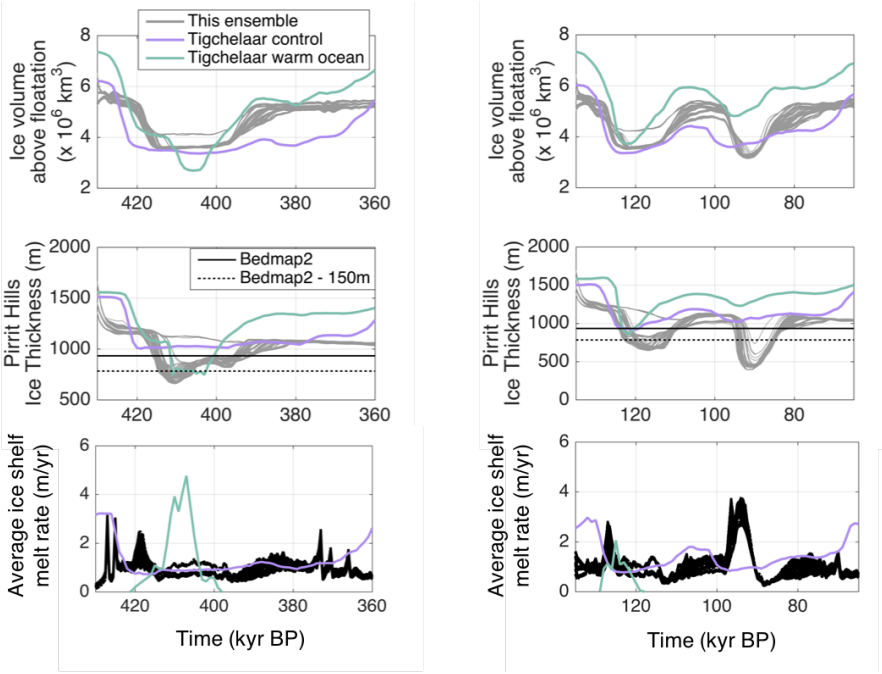

Figure 4-9: Ice sheet volumes, Pirrit Hills Ice thickness, and ice shelf melt rates for MIS 11(left-hand column) and MIS 5e (right-hand column) from the PSU-LOVE experiment and this ensemble. The ice sheet in the PSU-LOVE experiment only collapses with a five-fold increase in the ocean forcing. This collapse would likely expose the RB-2 core at the ice sheet surface.

4.6 CONCLUSIONS

Cosmogenic nuclide concentrations in a subglacial bedrock core from the Pirrit Hills show that the ice sheet has not thinned ≥ 150 m relative to present in at least the last 2 Myr. We have run a large ice-sheet model ensemble consisting of 90 parameter combinations over three of the strongest interglacials of the latter half of the Pleistocene to assess the relationship between

the ice thickness at the Pirrit Hills and the rest of the West Antarctic Ice Sheet. Below we summarize our key findings:

- Our modeling results in large ice sheet drawdowns during Marine Isotope Stages 31 and 5e relative to present conditions. The modeled MIS 11 ice sheet is similar to present day. Only a small group of these simulations predict a full collapse of the marine basins of West Antarctica, and this case occurs only during MIS 31. These simulations use a simple $\delta^{18}O$-based scaling of ocean climatology from a 20-kyr atmosphere-ocean GCM, but generally agree with recent 800 kyr GCM-driven model results that do not predict full WAIS collapse (Tigchelaar et al., 2018).
- Grounded ice sheet volume exhibits a nonlinear relationship with lithospheric flexure response times, ocean melt, basal traction, ice shelf hydrofracture, and ice cliff failure. We find that high basal traction, slow lithospheric rebound, elevated ice shelf melt, and some degree of ice shelf hydrofracture and ice cliff collapse are required in our model to cause collapse of the marine basins in West Antarctica for the given type and range of model forcing.
- Our modeling predicts large ice sheet drawdowns of ≥ 150 m around the Pirrit Hills and long periods of exposure of the RB-2 core site. The model ensemble runs are thus inconsistent with the extremely low nuclide concentrations in the bedrock core.
- Continuous ice cover at Pirrit Hills consistent with the nuclide measurements in the RB-2 core requires the persistence of the Filchner-Ronne ice shelf during warm interglacial periods. Average sub-ice shelf melt rates of >2 m/yr sustained for ~5 kyr are found to destroy the shelf during the modeled interglacial periods.

- Our data cannot exclude an ice sheet collapse like that modeled by Feldmann and Levermann (2015), in which retreat of the Amundsen sector deglaciates the marine basins of central West Antarctica without retreat of the grounding line in the Weddell Sector.
- Future recovery and analysis of more subglacial bedrock cores from sites throughout West Antarctica are required to determine the minimum size of the ice sheet during the Pleistocene.

4.7 ACKNOWLEDGEMENTS

This work was supported by U.S. NSF grant 1341728 to JOS. We thank the U.S. Air National Guard, the US Ice Drilling Design and Operations (IDDO) and the Antarctic Support Contract – especially Project Manager Leslie Blank, for logistical support at the Pirrit Hills. We also thank Anders Levermann, Johannes Feldmann, Michelle Tigchelaar, and Johannes Sutter for providing model output. Knut Christianson provided access to the Linux cluster used for the model ensemble, and the modeling presented here could not have been accomplished without the expertise, patience, and tireless diligence of University of Washington Earth and Space Sciences IT personnel Ed Mulligan and Nathan Briley. The University of Washington glaciology group provided invaluable feedback on early versions of this work.

BIBLIOGRAPHY

Anderson, B.M., Hindmarsh, R.C.A., Lawson, W.J., 2004. A modelling study of the response of Hatherton Glacier to Ross Ice Sheet grounding line retreat. Global and Planetary Change 42, 143–153. https://doi.org/10.1016/j.gloplacha.2003.11.006

Anderson, J.B., Conway, H., Bart, P.J., Witus, A.E., Greenwood, S.L., McKay, R.M., Hall, B.L., Ackert, R.P., Licht, K., Jakobsson, M., Stone, J.O., 2014. Ross Sea paleo-ice sheet drainage and deglacial history during and since the LGM. Quaternary Science Reviews, Reconstruction of Antarctic Ice Sheet Deglaciation (RAISED) 100, 31–54. https://doi.org/10.1016/j.quascirev.2013.08.020

Anderson, J.T.H., Wilson, G.S., Fink, D., Lilly, K., Levy, R.H., Townsend, D., 2017. Reconciling marine and terrestrial evidence for post LGM ice sheet retreat in southern McMurdo Sound, Antarctica. Quaternary Science Reviews 157, 1–13. https://doi.org/10.1016/j.quascirev.2016.12.007

Arthern, R.J., Winebrenner, D.P., Vaughan, D.G., 2006. Antarctic snow accumulation mapped using polarization of 4.3-cm wavelength microwave emission. Journal of Geophysical Research: Atmospheres 111. https://doi.org/10.1029/2004JD005667

Badgeley, J.A., Pettit, E.C., Carr, C.G., Tulaczyk, S., Mikucki, J.A., Lyons, W.B., Team, M.S., 2017. An englacial hydrologic system of brine within a cold glacier: Blood Falls, McMurdo Dry Valleys, Antarctica. Journal of Glaciology 63, 387–400. https://doi.org/10.1017/jog.2017.16

Balco, G., Todd, C., Huybers, K., Campbell, S., Vermeulen, M., Hegland, M., Goehring, B.M., Hillebrand, T.R., 2016. Cosmogenic-nuclide exposure ages from the Pensacola Mountains adjacent to the Foundation Ice Stream, Antarctica. Am J Sci 316, 542–577. https://doi.org/10.2475/06.2016.02

Bamber, J.L., Riva, R.E.M., Vermeersen, B.L.A., LeBrocq, A.M., 2009. Reassessment of the Potential Sea-Level Rise from a Collapse of the West Antarctic Ice Sheet. Science 324, 901–903. https://doi.org/10.1126/science.1169335

Barletta, V.R., Bevis, M., Smith, B.E., Wilson, T., Brown, A., Bordoni, A., Willis, M., Khan, S.A., Rovira-Navarro, M., Dalziel, I., Smalley, R., Kendrick, E., Konfal, S., Caccamise, D.J., Aster, R.C., Nyblade, A., Wiens, D.A., 2018. Observed rapid bedrock uplift in Amundsen Sea Embayment promotes ice-sheet stability. Science 360, 1335–1339. https://doi.org/10.1126/science.aao1447

Baroni, C., Hall, B.L., 2004. A new Holocene relative sea-level curve for Terra Nova Bay, Victoria Land, Antarctica. Journal of Quaternary Science 19, 377–396. https://doi.org/10.1002/jqs.825

Bindschadler, R., 1993. Siple Coast Project research of Crary Ice Rise and the mouths of Ice Streams B and C, West Antarctica: review and new perspectives. Journal of Glaciology 39, 538–552.

Bindschadler, R.A., Roberts, E.P., Iken, A., 1990. Age of Crary Ice Rise, Antarctica, determined from temperature-depth profiles. Ann. Glaciol 14, 13–16.

Bindschadler, R.A., Roberts, E.P., Macayeal, D.R., 1989. Distribution of net mass balance in the vicinity of Crary Ice Rise, Antarctica. J. Glaciol 35, 370–377.

Bintanja, R., 1999. On the glaciological, meteorological, and climatological significance of Antarctic blue ice areas. Rev. Geophys. 37, 337–359. https://doi.org/10.1029/1999RG900007

Bintanja, R., Van de Wal, R.S.W., 2008. North American ice-sheet dynamics and the onset of 100,000-year glacial cycles. Nature 454, 869.

Bockheim, J.G., Wilson, S.C., Denton, G.H., Andersen, B.G., Stuiver, M., 1989. Late Quaternary ice-surface fluctuations of Hatherton Glacier, Transantarctic Mountains. Quaternary Research 31, 229–254.

Bromley, G.R.M., Hall, B.L., Stone, J.O., Conway, H., 2012. Late Pleistocene evolution of Scott Glacier, southern Transantarctic Mountains: implications for the Antarctic contribution to deglacial sea level. Quaternary Science Reviews 50, 1–13. https://doi.org/10.1016/j.quascirev.2012.06.010

Bromley, G.R.M., Hall, B.L., Stone, J.O., Conway, H., Todd, C.E., 2010. Late Cenozoic deposits at Reedy Glacier, Transantarctic Mountains: implications for former thickness of the West Antarctic Ice Sheet. Quaternary Science Reviews 29, 384–398. https://doi.org/10.1016/j.quascirev.2009.07.001

Brown, I.C., Scambos, T.A., 2004. Satellite monitoring of blue-ice extent near Byrd Glacier, Antarctica. Annals of Glaciology 39, 223–230. https://doi.org/10.3189/172756404781813871

Campbell, S., Courville, Z., Sinclair, S., Wilner, J., 2017. Brine, englacial structure and basal properties near the terminus of McMurdo Ice Shelf, Antarctica. Annals of Glaciology 1–11.

Capron, E., Govin, A., Stone, E.J., Masson-Delmotte, V., Mulitza, S., Otto-Bliesner, B., Rasmussen, T.L., Sime, L.C., Waelbroeck, C., Wolff, E.W., 2014. Temporal and spatial structure of multi-millennial temperature changes at high latitudes during the Last Interglacial. Quaternary Science Reviews 103, 116–133. https://doi.org/10.1016/j.quascirev.2014.08.018

Catania, G., Hulbe, C., Conway, H., 2010. Grounding-line basal melt rates determined using radar-derived internal stratigraphy. Journal of Glaciology 56, 545–554. https://doi.org/10.3189/002214310792447842

Catania, G., Hulbe, C., Conway, H., Scambos, T.A., Raymond, C.F., 2012. Variability in the mass flux of the Ross ice streams, West Antarctica, over the last millennium. Journal of Glaciology 58, 741–752. https://doi.org/10.3189/2012JoG11J219

Catania, G.A., Conway, H., Raymond, C.F., Scambos, T.A., 2006. Evidence for floatation or near floatation in the mouth of Kamb Ice Stream, West Antarctica, prior to stagnation. Journal of Geophysical Research: Earth Surface 111.

Catania, G.A., Conway, H., Raymond, C.F., Scambos, T.A., 2005. Surface morphology and internal layer stratigraphy in the downstream end of Kamb Ice Stream, West Antarctica. Journal of Glaciology 51, 423–431. https://doi.org/10.3189/172756505781829142

Chatterjee, A., 2000. An introduction to the proper orthogonal decomposition. Current Science 78, 808–817.

Christianson, K., Jacobel, R.W., Horgan, H.J., Alley, R.B., Anandakrishnan, S., Holland, D.M., DallaSanta, K.J., 2016. Basal conditions at the grounding zone of Whillans Ice Stream, West Antarctica, from ice-penetrating radar. J. Geophys. Res. Earth Surf. 121, 2015JF003806. https://doi.org/10.1002/2015JF003806

Clough, J.W., 1973. Radio Echo Sounding: Brine Percolation Layer * . Journal of Glaciology 12, 141–143. https://doi.org/10.3189/S0022143000022796

Conway, H., 1999. Past and Future Grounding-Line Retreat of the West Antarctic Ice Sheet. Science 286, 280–283. https://doi.org/10.1126/science.286.5438.280

Conway, H., Catania, G., Raymond, C.F., Gades, A.M., Scambos, T.A., Engelhardt, H., 2002. Switch of flow direction in an Antarctic ice stream. Nature 419, 465–467.

Craven, M., Allison, I., Fricker, H.A., Warner, R., 2009. Properties of a marine ice layer under the Amery Ice Shelf, East Antarctica. Journal of Glaciology 55, 717–728.

Cuffey, K.M., Paterson, W.S.B., 2010. The physics of glaciers. Academic Press.

DeConto, R.M., Pollard, D., 2016. Contribution of Antarctica to past and future sea-level rise. Nature 531, 591–597. https://doi.org/10.1038/nature17145

DeConto, R.M., Pollard, D., Kowalewski, D., 2012. Modeling Antarctic ice sheet and climate variations during Marine Isotope Stage 31. Global and Planetary Change 88–89, 45–52. https://doi.org/10.1016/j.gloplacha.2012.03.003

Denton, G.H., Bockheim, J.G., Wilson, S.C., Leide, J.E., Andersen, B.G., 1989. Late Quaternary ice-surface fluctuations of Beardmore Glacier, Transantarctic Mountains. Quaternary Research 31, 183–209. https://doi.org/10.1016/0033-5894(89)90005-7

Ditchburn, R.G., Whitehead, N.E., 1994. The separation of ^{10}Be from silicates.

Dowdeswell, J.A., Ottesen, D., Evans, J., Cofaigh, C.Ó., Anderson, J.B., 2008. Submarine glacial landforms and rates of ice-stream collapse. Geology 36, 819–822. https://doi.org/10.1130/G24808A.1

Dubrovin, L.I., 1960. Brine in the Lazarev Ice Shelf. Informatsionny Byulleten'Sovetkoj Antarkticheskoj Ekspeditsii [Soviet Antarctic Expedition Information Bulletin] 22, 15–16.

Dutton, A., Carlson, A.E., Long, A.J., Milne, G.A., Clark, P.U., DeConto, R., Horton, B.P., Rahmstorf, S., Raymo, M.E., 2015. Sea-level rise due to polar ice-sheet mass loss during past warm periods. Science 349, aaa4019. https://doi.org/10.1126/science.aaa4019

Dutton, A., Lambeck, K., 2012. Ice Volume and Sea Level During the Last Interglacial. Science 337, 216–219. https://doi.org/10.1126/science.1205749

Edwards, T.L., Brandon, M.A., Durand, G., Edwards, N.R., Golledge, N.R., Holden, P.B., Nias, I.J., Payne, A.J., Ritz, C., Wernecke, A., 2019. Revisiting Antarctic ice loss due to marine ice-cliff instability. Nature 566, 58. https://doi.org/10.1038/s41586-019-0901-4

EPICA Community Members, 2004. Eight glacial cycles from an Antarctic ice core. Nature 429, 623–628. https://doi.org/EPICA Community Members

Fahnestock, M.A., Scambos, T.A., Bindschadler, R.A., Kvaran, G., 2000. A millennium of variable ice flow recorded by the Ross Ice Shelf, Antarctica. Journal of Glaciology 46, 652–664.

Feldmann, J., Levermann, A., 2015. Collapse of the West Antarctic Ice Sheet after local destabilization of the Amundsen Basin. PNAS 112, 14191–14196. https://doi.org/10.1073/pnas.1512482112

Fretwell, P., Pritchard, H.D., Vaughan, D.G., Bamber, J.L., Barrand, N.E., Bell, R., Bianchi, C., Bingham, R.G., Blankenship, D.D., Casassa, G., Catania, G., Callens, D., Conway, H., Cook, A.J., Corr, H.F.J., Damaske, D., Damm, V., Ferraccioli, F., Forsberg, R., Fujita, S., Gim, Y., Gogineni, P., Griggs, J.A., Hindmarsh, R.C.A., Holmlund, P., Holt, J.W., Jacobel, R.W., Jenkins, A., Jokat, W., Jordan, T., King, E.C., Kohler, J., Krabill, W., Riger-Kusk, M., Langley, K.A., Leitchenkov, G., Leuschen, C., Luyendyk, B.P., Matsuoka, K., Mouginot, J., Nitsche, F.O., Nogi, Y., Nost, O.A., Popov, S.V., Rignot, E., Rippin, D.M., Rivera, A., Roberts, J., Ross, N., Siegert, M.J., Smith, A.M., Steinhage, D.,

Studinger, M., Sun, B., Tinto, B.K., Welch, B.C., Wilson, D., Young, D.A., Xiangbin, C., Zirizzotti, A., 2013. Bedmap2: improved ice bed, surface and thickness datasets for Antarctica. The Cryosphere 7, 375–393. https://doi.org/10.5194/tc-7-375-2013

Fricker, H.A., Popov, S., Allison, I., Young, N., 2001. Distribution of marine ice beneath the Amery Ice Shelf. Geophys. Res. Lett. 28, 2241–2244. https://doi.org/10.1029/2000GL012461

Fujita, S., Maeno, H., Uratsuka, S., Furukawa, T., Mae, S., Fujii, Y., Watanabe, O., 1999. Nature of radio echo layering in the Antarctic Ice Sheet detected by a two-frequency experiment. J. Geophys. Res. 104, 13013–13024. https://doi.org/10.1029/1999JB900034

Gaylord, D.R., Robertson, J.D., 1975. Sediments exposed on the surface of the Ross Ice Shelf, Antarctica. Journal of Glaciology 14, 332–333.

Gillespie, M.K., Lawson, W., Rack, W., Anderson, B., Blankenship, D.D., Young, D.A., Holt, J.W., 2017. Geometry and ice dynamics of the Darwin–Hatherton glacial system, Transantarctic Mountains. Journal of Glaciology 1–14. https://doi.org/10.1017/jog.2017.60

Goehring, B.M., Wilson, J., Nichols, K., 2019. A fully automated system for the extraction of in situ cosmogenic carbon-14 in the Tulane University cosmogenic nuclide laboratory. Nuclear Instruments and Methods in Physics Research Section B: Beam Interactions with Materials and Atoms. https://doi.org/10.1016/j.nimb.2019.02.006

Goldberg, D., Holland, D.M., Schoof, C., 2009. Grounding line movement and ice shelf buttressing in marine ice sheets. J. Geophys. Res. 114, F04026. https://doi.org/10.1029/2008JF001227

Golledge, N.R., Levy, R.H., McKay, R.M., Naish, T.R., 2017. East Antarctic ice sheet most vulnerable to Weddell Sea warming. Geophys. Res. Lett. 44, 2016GL072422. https://doi.org/10.1002/2016GL072422

Gomez, N., Pollard, D., Mitrovica, J.X., 2013. A 3-D coupled ice sheet – sea level model applied to Antarctica through the last 40 ky. Earth and Planetary Science Letters 384, 88–99. https://doi.org/10.1016/j.epsl.2013.09.042

Goosse, H., Brovkin, V., Fichefet, T., Haarsma, R., Huybrechts, P., Jongma, J., Mouchet, A., Selten, F., Barriat, P.-Y., Campin, J.-M., Deleersnijder, E., Driesschaert, E., Goelzer, H., Janssens, I., Loutre, M.-F., Morales Maqueda, M.A., Opsteegh, T., Mathieu, P.-P., Munhoven, G., Pettersson, E.J., Renssen, H., Roche, D.M., Schaeffer, M., Tartinville, B., Timmermann, A., Weber, S.L., 2010. Description of the Earth system model of intermediate complexity LOVECLIM version 1.2. Geoscientific Model Development 3, 603–633. https://doi.org/10.5194/gmd-3-603-2010

Gourmelen, N., Goldberg, D.N., Snow, K., Henley, S.F., Bingham, R.G., Kimura, S., Hogg, A.E., Shepherd, A., Mouginot, J., Lenaerts, J., 2017. Channelized melting drives thinning under a rapidly melting Antarctic ice shelf. Geophysical Research Letters 44, 9796–9804.

Greene, C.A., Gwyther, D.E., Blankenship, D.D., 2017a. Antarctic mapping tools for MATLAB. Computers & Geosciences 104, 151–157.

Greene, C.A., Gwyther, D.E., Blankenship, D.D., 2017b. Antarctic Mapping Tools for Matlab. Computers & Geosciences 104, 151–157. https://doi.org/10.1016/j.cageo.2016.08.003

Grima, C., Greenbaum, J.S., Lopez Garcia, E.J., Soderlund, K.M., Rosales, A., Blankenship, D.D., Young, D.A., 2016. Radar detection of the brine extent at McMurdo Ice Shelf, Antarctica, and its control by snow accumulation. Geophys. Res. Lett. 43, 2016GL069524. https://doi.org/10.1002/2016GL069524

Halberstadt, A.R.W., Simkins, L.M., Greenwood, S.L., Anderson, J.B., 2016. Past ice-sheet behaviour: retreat scenarios and changing controls in the Ross Sea, Antarctica. The Cryosphere 10, 1003–1020. https://doi.org/10.5194/tc-10-1003-2016

Hall, B.L., Baroni, C., Denton, G.H., 2004. Holocene relative sea-level history of the Southern Victoria Land Coast, Antarctica. Global and Planetary Change, Ice sheets and neotectonics 42, 241–263. https://doi.org/10.1016/j.gloplacha.2003.09.004

Haran, T., Bohlander, J., Scambos, T., Painter, T., Fahnestock, M., 2014. MODIS Mosaic of Antarctica 2008–2009 (MOA2009) image map. Boulder, Colorado USA, National Snow and Ice Data Center 10, N5KP8037.

Hay, C., Mitrovica, J.X., Gomez, N., Creveling, J.R., Austermann, J., E. Kopp, R., 2014. The sea-level fingerprints of ice-sheet collapse during interglacial periods. Quaternary Science Reviews 87, 60–69. https://doi.org/10.1016/j.quascirev.2013.12.022

Hellmer, H.H., Kauker, F., Timmermann, R., Determann, J., Rae, J., 2012. Twenty-first-century warming of a large Antarctic ice-shelf cavity by a redirected coastal current. Nature 485, nature11064. https://doi.org/10.1038/nature11064

Hendy, C.H., 2000. Late Quaternary Lakes in the McMurdo Sound Region of Antarctica. Geografiska Annaler: Series A, Physical Geography 82, 411–432. https://doi.org/10.1111/j.0435-3676.2000.00131.x

Holland, P.R., Corr, H.F.J., Vaughan, D.G., Jenkins, A., Skvarca, P., 2009. Marine ice in Larsen Ice Shelf. Geophys. Res. Lett. 36, L11604. https://doi.org/10.1029/2009GL038162

Holland, P.R., Jenkins, A., Holland, D.M., 2008. The Response of Ice Shelf Basal Melting to Variations in Ocean Temperature. J. Climate 21, 2558–2572. https://doi.org/10.1175/2007JCLI1909.1

Holschuh, N., Christianson, K., Anandakrishnan, S., 2014. Power loss in dipping internal reflectors, imaged using ice-penetrating radar. Annals of Glaciology 55, 49–56. https://doi.org/10.3189/2014AoG67A005

Hönisch, B., Hemming, N.G., Archer, D., Siddall, M., McManus, J.F., 2009. Atmospheric carbon dioxide concentration across the mid-Pleistocene transition. Science 324, 1551–1554.

Howat, I.M., Porter, C., Smith, B.E., Noh, M.-J., Morin, P., 2019. The Reference Elevation Model of Antarctica. The Cryosphere 13, 665–674.

Hughes, T., Zhao, Z., Hintz, R., Fastook, J., 2017. Instability of the Antarctic Ross Sea Embayment as climate warms. Rev. Geophys. 55, 2016RG000545. https://doi.org/10.1002/2016RG000545

Hughes, T.J., 1981. The weak underbelly of the West Antarctic ice-Sheet.

Hulbe, C., Fahnestock, M., 2007. Century-scale discharge stagnation and reactivation of the Ross ice streams, West Antarctica. J. Geophys. Res. 112, F03S27. https://doi.org/10.1029/2006JF000603

Hulbe, C.L., Fahnestock, M.A., 2004. West Antarctic ice-stream discharge variability: mechanism, controls and pattern of grounding-line retreat. Journal of Glaciology 50, 471–484. https://doi.org/10.3189/172756504781829738

Jansen, D., Luckman, A., Kulessa, B., Holland, P.R., King, E.C., 2013. Marine ice formation in a suture zone on the Larsen C Ice Shelf and its influence on ice shelf dynamics. J. Geophys. Res. Earth Surf. 118, 1628–1640. https://doi.org/10.1002/jgrf.20120

Jones, R.S., Mackintosh, A.N., Norton, K.P., Golledge, N.R., Fogwill, C.J., Kubik, P.W., Christl, M., Greenwood, S.L., 2015. Rapid Holocene thinning of an East Antarctic outlet glacier

driven by marine ice sheet instability. Nat Commun 6, 8910. https://doi.org/10.1038/ncomms9910

Joughin, I., Smith, B.E., Howat, I.M., Floricioiu, D., Alley, R.B., Truffer, M., Fahnestock, M., 2012. Seasonal to decadal scale variations in the surface velocity of Jakobshavn Isbrae, Greenland: Observation and model-based analysis. Journal of Geophysical Research: Earth Surface 117.

Joughin, I., Smith, B.E., Medley, B., 2014. Marine Ice Sheet Collapse Potentially Under Way for the Thwaites Glacier Basin, West Antarctica. Science 344, 735–738. https://doi.org/10.1126/science.1249055

Jouzel, J., Masson-Delmotte, V., Cattani, O., Dreyfus, G., Falourd, S., Hoffmann, G., Minster, B., Nouet, J., Barnola, J.M., Chappellaz, J., Fischer, H., Gallet, J.C., Johnsen, S., Leuenberger, M., Loulergue, L., Luethi, D., Oerter, H., Parrenin, F., Raisbeck, G., Raynaud, D., Schilt, A., Schwander, J., Selmo, E., Souchez, R., Spahni, R., Stauffer, B., Steffensen, J.P., Stenni, B., Stocker, T.F., Tison, J.L., Werner, M., Wolff, E.W., 2007. Orbital and Millennial Antarctic Climate Variability over the Past 800,000 Years. Science 317, 793–796. https://doi.org/10.1126/science.1141038

Joy, K., Fink, D., Storey, B., Atkins, C., 2014. A 2 million year glacial chronology of the Hatherton Glacier, Antarctica and implications for the size of the East Antarctic Ice Sheet at the Last Glacial Maximum. Quaternary Science Reviews 83, 46–57. https://doi.org/10.1016/j.quascirev.2013.10.028

Kessler, M.A., Anderson, R.S., Briner, J.P., 2008. Fjord insertion into continental margins driven by topographic steering of ice. Nature Geoscience 1, 365–369. https://doi.org/10.1038/ngeo201

Khazendar, A., Jenkins, A., 2003. A model of marine ice formation within Antarctic ice shelf rifts. J. Geophys. Res. 108, 3235. https://doi.org/10.1029/2002JC001673

Khazendar, A., Rignot, E., Larour, E., 2009. Roles of marine ice, rheology, and fracture in the flow and stability of the Brunt/Stancomb-Wills Ice Shelf. Journal of Geophysical Research 114. https://doi.org/10.1029/2008JF001124

King, C.C., 2017. Understanding climate history and ice extent in the mid- to high-latitudes of the Southern Hemisphere during the Last Glacial Maximum 335.

Kingslake, J., Scherer, R.P., Albrecht, T., Coenen, J., Powell, R.D., Reese, R., Stansell, N.D., Tulaczyk, S., Wearing, M.G., Whitehouse, P.L., 2018. Extensive retreat and re-advance of the West Antarctic Ice Sheet during the Holocene. Nature 1. https://doi.org/10.1038/s41586-018-0208-x

Kohl, C.P., Nishiizumi, K., 1992. Chemical isolation of quartz for measurement of in-situ-produced cosmogenic nuclides. Geochimica et Cosmochimica Acta 56, 3583–3587.

Kulessa, B., Jansen, D., Luckman, A.J., King, E.C., Sammonds, P.R., 2014. Marine ice regulates the future stability of a large Antarctic ice shelf. Nature Communications 5, ncomms4707. https://doi.org/10.1038/ncomms4707

Larour, E., Rignot, E., Aubry, D., 2004. Processes involved in the propagation of rifts near Hemmen Ice Rise, Ronne Ice Shelf, Antarctica. Journal of Glaciology 50, 329–341. https://doi.org/10.3189/172756504781829837

Larour, E., Seroussi, H., Adhikari, S., Ivins, E., Caron, L., Morlighem, M., Schlegel, N., 2019. Slowdown in Antarctic mass loss from solid Earth and sea-level feedbacks. Science eaav7908. https://doi.org/10.1126/science.aav7908

Laskar, J., Robutel, P., Joutel, F., Gastineau, M., Correia, A.C.M., Levrard, B., 2004. A long-term numerical solution for the insolation quantities of the Earth. Astronomy & Astrophysics 428, 261–285. https://doi.org/10.1051/0004-6361:20041335

Laskar, Jacques, Robutel, P., Joutel, F., Gastineau, M., Correia, A.C.M., Levrard, B., 2004. A long-term numerical solution for the insolation quantities of the Earth. Astronomy & Astrophysics 428, 261–285.

Le Brocq, A.M., Payne, A.J., Vieli, A., 2010. An improved Antarctic dataset for high resolution numerical ice sheet models (ALBMAP v1). Earth System Science Data 2, 247–260. https://doi.org/10.5194/essd-2-247-2010

Lee, J.I., McKay, R.M., Golledge, N.R., Yoon, H.I., Yoo, K.-C., Kim, H.J., Hong, J.K., 2017. Widespread persistence of expanded East Antarctic glaciers in the southwest Ross Sea during the last deglaciation. Geology G38715.1. https://doi.org/10.1130/G38715.1

Lenaerts, Jan TM, Van Den Broeke, M.R., Scarchilli, C., Agosta, C., 2012. Impact of model resolution on simulated wind, drifting snow and surface mass balance in Terre Adélie, East Antarctica. Journal of Glaciology 58, 821–829.

Lenaerts, J. T., Van den Broeke, M.R., van de Berg, W.J., van Meijgaard, E., Kuipers Munneke, P., 2012. A new, high-resolution surface mass balance map of Antarctica (1979–2010) based on regional atmospheric climate modeling. Geophysical Research Letters 39.

Lewis, C., Gogineni, S., Rodriguez-Morales, F., Panzer, B., Stumpf, T., Paden, J., Leuschen, C., 2015. Airborne fine-resolution UHF radar: an approach to the study of englacial reflections, firn compaction and ice attenuation rates. Journal of Glaciology 61, 89–100. https://doi.org/10.3189/2015JoG14J089

Lewis, E.L., Perkin, R.G., 1986. Ice pumps and their rates. Journal of Geophysical Research: Oceans 91, 11756–11762.

Lisiecki, L.E., Raymo, M.E., 2005. A Pliocene-Pleistocene stack of 57 globally distributed benthic δ18O records. Paleoceanography 20, PA1003. https://doi.org/10.1029/2004PA001071

Liu, Z., Otto-Bliesner, B.L., He, F., Brady, E.C., Tomas, R., Clark, P.U., Carlson, A.E., Lynch-Stieglitz, J., Curry, W., Brook, E., Erickson, D., Jacob, R., Kutzbach, J., Cheng, J., 2009. Transient simulation of last deglaciation with a new mechanism for Bolling-Allerod warming. Science 325, 310–314. https://doi.org/10.1126/science.1171041

Looyenga, H., 1965. Dielectric constants of heterogeneous mixtures. Physica 31, 401–406. https://doi.org/10.1016/0031-8914(65)90045-5

Loutre, M.F., Berger, A., 2003. Marine Isotope Stage 11 as an analogue for the present interglacial. Global and Planetary Change, THE EEMIAN INTERGLACIAL: A GLOBAL PERSPECTIVE 36, 209–217. https://doi.org/10.1016/S0921-8181(02)00186-8

Lüthi, D., Le Floch, M., Bereiter, B., Blunier, T., Barnola, J.-M., Siegenthaler, U., Raynaud, D., Jouzel, J., Fischer, H., Kawamura, K., Stocker, T.F., 2008. High-resolution carbon dioxide concentration record 650,000–800,000 years before present. Nature 453, 379–382. https://doi.org/10.1038/nature06949

Lux, F., 1993. Models proposed to explain the electrical conductivity of mixtures made of conductive and insulating materials. Journal of materials science 28, 285–301.

MacAyeal, D.R., Bindschadler, R.A., Stephenson, S., Shabtaie, S., Bentley, C.R., 1987. Force, mass, and energy budgets of the Crary Ice Rise complex, Antarctica. Journal of Glaciology 33, 218–230.

Matsuoka, K., Hindmarsh, R.C.A., Moholdt, G., Bentley, M.J., Pritchard, H.D., Brown, J., Conway, H., Drews, R., Durand, G., Goldberg, D., Hattermann, T., Kingslake, J., Lenaerts, J.T.M., Martín, C., Mulvaney, R., Nicholls, K.W., Pattyn, F., Ross, N., Scambos, T., Whitehouse, P.L., 2015. Antarctic ice rises and rumples: Their properties and significance for ice-sheet dynamics and evolution. Earth-Science Reviews 150, 724–745. https://doi.org/10.1016/j.earscirev.2015.09.004

McKay, R., Golledge, N.R., Maas, S., Naish, T., Levy, R., Dunbar, G., Kuhn, G., 2016. Antarctic marine ice-sheet retreat in the Ross Sea during the early Holocene. Geology 44, 7–10. https://doi.org/10.1130/G37315.1

McKay, R., Naish, T., Powell, R., Barrett, P., Scherer, R., Talarico, F., Kyle, P., Monien, D., Kuhn, G., Jackolski, C., Williams, T., 2012. Pleistocene variability of Antarctic Ice Sheet extent in the Ross Embayment. Quaternary Science Reviews 34, 93–112. https://doi.org/10.1016/j.quascirev.2011.12.012

Mercer, J.H., 1978. West Antarctic ice sheet and CO2 greenhouse effect: a threat of disaster. Nature 271, 321.

Monahan, A.H., Fyfe, J.C., Ambaum, M.H.P., Stephenson, D.B., North, G.R., 2009. Empirical Orthogonal Functions: The Medium is the Message. Journal of Climate 22, 6501–6514. https://doi.org/10.1175/2009JCLI3062.1

Monnin, E., Steig, E.J., Siegenthaler, U., Kawamura, K., Schwander, J., Stauffer, B., Stocker, T.F., Morse, D.L., Barnola, J.-M., Bellier, B., Raynaud, D., Fischer, H., 2004. Evidence for substantial accumulation rate variability in Antarctica during the Holocene, through synchronization of CO2 in the Taylor Dome, Dome C and DML ice cores. Earth and Planetary Science Letters 224, 45–54. https://doi.org/10.1016/j.epsl.2004.05.007

Neal, C.S., 1979. The Dynamics of the Ross Ice Shelf Revealed by Radio Echo-Sounding. Journal of Glaciology 24, 295–307. https://doi.org/10.3198/1979JoG24-90-295-307

NEEM community Members, Dahl-Jensen, D., Albert, M.R., Aldahan, A., Azuma, N., Balslev-Clausen, D., Baumgartner, M., Berggren, A.-M., Bigler, M., Binder, T., Blunier, T., Bourgeois, J.C., Brook, E.J., Buchardt, S.L., Buizert, C., Capron, E., Chappellaz, J., Chung, J., Clausen, H.B., Cvijanovic, I., Davies, S.M., Ditlevsen, P., Eicher, O., Fischer, H., Fisher, D.A., Fleet, L.G., Gfeller, G., Gkinis, V., Gogineni, S., Goto-Azuma, K., Grinsted, A., Gudlaugsdottir, H., Guillevic, M., Hansen, S.B., Hansson, M., Hirabayashi, M., Hong, S., Hur, S.D., Huybrechts, P., Hvidberg, C.S., Iizuka, Y., Jenk, T., Johnsen, S.J., Jones, T.R., Jouzel, J., Karlsson, N.B., Kawamura, K., Keegan, K., Kettner, E., Kipfstuhl, S., Kjær, H.A., Koutnik, M., Kuramoto, T., Köhler, P., Laepple, T., Landais, A., Langen, P.L., Larsen, L.B., Leuenberger, D., Leuenberger, M., Leuschen, C., Li, J., Lipenkov, V., Martinerie, P., Maselli, O.J., Masson-Delmotte, V., McConnell, J.R., Miller, H., Mini, O., Miyamoto, A., Montagnat-Rentier, M., Mulvaney, R., Muscheler, R., Orsi, A.J., Paden, J., Panton, C., Pattyn, F., Petit, J.-R., Pol, K., Popp, T., Possnert, G., Prié, F., Prokopiou, M., Quiquet, A., Rasmussen, S.O., Raynaud, D., Ren, J., Reutenauer, C., Ritz, C., Röckmann, T., Rosen, J.L., Rubino, M., Rybak, O., Samyn, D., Sapart, C.J., Schilt, A., Schmidt, A.M.Z., Schwander, J., Schüpbach, S., Seierstad, I., Severinghaus, J.P., Sheldon, S., Simonsen, S.B., Sjolte, J., Solgaard, A.M., Sowers, T., Sperlich, P., Steen-Larsen, H.C., Steffen, K., Steffensen, J.P., Steinhage, D., Stocker, T.F., Stowasser, C., Sturevik, A.S., Sturges, W.T., Sveinbjörnsdottir, A., Svensson, A., Tison, J.-L., Uetake, J., Vallelonga, P., van de Wal, R.S.W., van der Wel, G., Vaughn, B.H., Vinther, B., Waddington, E., Wegner, A., Weikusat, I., White, J.W.C., Wilhelms, F., Winstrup,

M., Witrant, E., Wolff, E.W., Xiao, C., Zheng, J., 2013. Eemian interglacial reconstructed from a Greenland folded ice core. Nature 493, 489–494. https://doi.org/10.1038/nature11789

Ng, F., Conway, H., 2004. Fast-flow signature in the stagnated Kamb Ice Stream, West Antarctica. Geology 32, 481–484. https://doi.org/10.1130/G20317.1

Noonan, B., Zawar-Reza, P., Lawson, W., 2015. Boundary-layer climate of the Darwin-Hatherton Glacial System, Antarctica: meso- and synoptic-scale circulations: DARWIN-HATHERTON BOUNDARY-LAYER CLIMATE, ANTARCTICA. International Journal of Climatology 35, 3608–3623. https://doi.org/10.1002/joc.4235

Petit, J.-R., Jouzel, J., Raynaud, D., Barkov, N.I., Barnola, J.-M., Basile, I., Bender, M., Chappellaz, J., Davis, M., Delaygue, G., others, 1999. Climate and atmospheric history of the past 420,000 years from the Vostok ice core, Antarctica. Nature 399, 429–436.

Pollard, D., Chang, W., Haran, M., Applegate, P., DeConto, R., 2016. Large ensemble modeling of the last deglacial retreat of the West Antarctic Ice Sheet: comparison of simple and advanced statistical techniques. Geosci. Model Dev. 9, 1697–1723. https://doi.org/10.5194/gmd-9-1697-2016

Pollard, D., DeConto, R.M., 2012a. Description of a hybrid ice sheet-shelf model, and application to Antarctica. Geosci. Model Dev. 5, 1273–1295. https://doi.org/10.5194/gmd-5-1273-2012

Pollard, D., DeConto, R.M., 2012b. A simple inverse method for the distribution of basal sliding coefficients under ice sheets, applied to Antarctica. The Cryosphere 6, 953–971. https://doi.org/10.5194/tc-6-953-2012

Pollard, D., DeConto, R.M., 2009. Modelling West Antarctic ice sheet growth and collapse through the past five million years. Nature 458, 329–332. https://doi.org/10.1038/nature07809

Pollard, D., DeConto, R.M., Alley, R.B., 2015. Potential Antarctic Ice Sheet retreat driven by hydrofracturing and ice cliff failure. Earth and Planetary Science Letters 412, 112–121. https://doi.org/10.1016/j.epsl.2014.12.035

Pollard, David, Won Chang, Haran, M., Applegate, P., DeConto, R., 2016. Large ensemble modeling of the last deglacial retreat of the West Antarctic Ice Sheet: comparison of simple and advanced statistical techniques. Geoscientific Model Development 9, 1697–1723. https://doi.org/10.5194/gmd-9-1697-2016

Raymo, M.E., Kozdon, R., Evans, D., Lisiecki, L., Ford, H.L., 2018. The accuracy of mid-Pliocene δ18O-based ice volume and sea level reconstructions. Earth-Science Reviews 177, 291–302. https://doi.org/10.1016/j.earscirev.2017.11.022

Raymo, M.E., Lisiecki, L.E., Nisancioglu, K.H., 2006. Plio-Pleistocene ice volume, Antarctic climate, and the global δ18O record. Science 313, 492–495.

Raymo, M.E., Mitrovica, J.X., 2012. Collapse of polar ice sheets during the stage 11 interglacial. Nature 483, 453–456. https://doi.org/10.1038/nature10891

Raymond, C.F., 2000. Energy balance of ice streams. Journal of Glaciology 46, 665–674.

Raymond, C.F., 1983. Deformation in the Vicinity of Ice Divides. Journal of Glaciology 29, 357–373. https://doi.org/10.3189/S0022143000030288

Reese, R., Winkelmann, R., Gudmundsson, G.H., 2018. Grounding-line flux formula applied as a flux condition in numerical simulations fails for buttressed Antarctic ice streams. The Cryosphere Discussions 1–22. https://doi.org/10.5194/tc-2017-289

Reyes, A.V., Carlson, A.E., Beard, B.L., Hatfield, R.G., Stoner, J.S., Winsor, K., Welke, B., Ullman, D.J., 2014. South Greenland ice-sheet collapse during Marine Isotope Stage 11. Nature 510, 525–528. https://doi.org/10.1038/nature13456

Rignot, E., Casassa, G., Gogineni, P., Krabill, W., Rivera, A., Thomas, R., 2004. Accelerated ice discharge from the Antarctic Peninsula following the collapse of Larsen B ice shelf. Geophysical Research Letters 31. https://doi.org/10.1029/2004GL020697

Rignot, E., MacAyeal, D.R., 1998. Ice-shelf dynamics near the front of the Filchner—Ronne Ice Shelf, Antarctica, revealed by SAR interferometry. Journal of Glaciology 44, 405–418. https://doi.org/10.3189/S0022143000002732

Rignot, E., Mouginot, J., Scheuchl, B., 2011. Ice flow of the Antarctic ice sheet. Science 333, 1427–1430.

Rodriguez-Morales, F., Gogineni, S., Leuschen, C.J., Paden, J.D., Li, J., Lewis, C.C., Panzer, B., Gomez-Garcia Alvestegui, D., Patel, A., Byers, K., Crowe, R., Player, K., Hale, R.D., Arnold, E.J., Smith, L., Gifford, C.M., Braaten, D., Panton, C., 2014. Advanced Multifrequency Radar Instrumentation for Polar Research. IEEE Transactions on Geoscience and Remote Sensing 52, 2824–2842. https://doi.org/10.1109/TGRS.2013.2266415

Scambos, T., Fricker, H.A., Liu, C.-C., Bohlander, J., Fastook, J., Sargent, A., Massom, R., Wu, A.-M., 2009. Ice shelf disintegration by plate bending and hydro-fracture: Satellite observations and model results of the 2008 Wilkins ice shelf break-ups. Earth and Planetary Science Letters 280, 51–60.

Schaefer, J.M., Finkel, R.C., Balco, G., Alley, R.B., Caffee, M.W., Briner, J.P., Young, N.E., Gow, A.J., Schwartz, R., 2016. Greenland was nearly ice-free for extended periods during the Pleistocene. Nature 540, 252–255. https://doi.org/10.1038/nature20146

Scherer, RP, 1988. Micropaleontological analysis of sediments from the Crary Ice Rise, Ross ice Shelf. Antarctic Journ. U.S.

Scherer, R.P., Aldahan, A., Tulaczyk, S., Possnert, G., Engelhardt, H., Kamb, B., 1998. Pleistocene Collapse of the West Antarctic Ice Sheet. Science 281, 82–85. https://doi.org/10.1126/science.281.5373.82

Scherer, R.P., Bohaty, S.M., Dunbar, R.B., Esper, O., Flores, J.-A., Gersonde, R., Harwood, D.M., Roberts, A.P., Taviani, M., 2008. Antarctic records of precession-paced insolation-driven warming during early Pleistocene Marine Isotope Stage 31. Geophysical Research Letters 35. https://doi.org/10.1029/2007GL032254

Schoof, C., 2007. Ice sheet grounding line dynamics: Steady states, stability, and hysteresis. Journal of Geophysical Research 112. https://doi.org/10.1029/2006JF000664

Shabtaie, S., Bentley, C.R., 1987. West Antarctic ice streams draining into the Ross Ice Shelf: configuration and mass balance. Journal of Geophysical Research: Solid Earth (1978–2012) 92, 1311–1336.

Siddall, M., Chappell, J., Potter, E.-K., 2007. 7. Eustatic sea level during past interglacials, in: Developments in Quaternary Sciences. Elsevier, pp. 75–92.

Spector, P., Stone, J., Cowdery, S.G., Hall, B., Conway, H., Bromley, G., 2017. Rapid early-Holocene deglaciation in the Ross Sea, Antarctica. Geophys. Res. Lett. 2017GL074216. https://doi.org/10.1002/2017GL074216

Spector, P., Stone, J., Pollard, D., Hillebrand, T., Lewis, C., Gombiner, J., 2018. West Antarctic sites for subglacial drilling to test for past ice-sheet collapse. The Cryosphere 12, 2741–2757. https://doi.org/10.5194/tc-12-2741-2018

Spratt, R.M., Lisiecki, L.E., 2016. A Late Pleistocene sea level stack. Climate of the Past 12, 1079–1092. https://doi.org/10.5194/cp-12-1079-2016

Stearns, L.A., 2011. Dynamics and mass balance of four large East Antarctic outlet glaciers. Annals of Glaciology 52, 116–126.

Steig, E.J., Morse, D.L., Waddington, E.D., Stuiver, M., Grootes, P.M., Mayewski, P.A., Twickler, M.S., Whitlow, S.I., 2000. Wisconsinan and Holocene Climate History from an Ice Core at Taylor Dome, Western Ross Embayment, Antarctica. Geografiska Annaler: Series A, Physical Geography 82, 213–235. https://doi.org/10.1111/j.0435-3676.2000.00122.x

Stolt, R.H., 1978. Migration by Fourier transform. Geophysics 43, 23–48.

Stone, E.J., Lunt, D.J., Annan, J.D., Hargreaves, J.C., 2013. Quantification of the Greenland ice sheet contribution to Last Interglacial sea level rise. Climate of the Past 9, 621–639. https://doi.org/10.5194/cp-9-621-2013

Stone, J., Spector, P., Hillebrand, T., Gombiner, J., Feathers, J., Severinghaus, J., Pollard, D., Balco, G., Fifield, K., Talghader, J., DeWitt, R., 2017. West Antarctic Ice Sheet History from a Subglacial Bedrock Core. West Antarctic Ice Sheet Workshop in Coupeville, WA.

Stone, J.O., 2000. Air pressure and cosmogenic isotope production. J. Geophys. Res. 105, 23753–23759. https://doi.org/10.1029/2000JB900181

Storey, B.C., Fink, D., Hood, D., Joy, K., Shulmeister, J., Riger-Kusk, M., Stevens, M.I., 2010. Cosmogenic nuclide exposure age constraints on the glacial history of the Lake Wellman area, Darwin Mountains, Antarctica. Antarctic Science 22, 603–618. https://doi.org/10.1017/S0954102010000799

Sutter, J., Gierz, P., Grosfeld, K., Thoma, M., Lohmann, G., 2016. Ocean temperature thresholds for Last Interglacial West Antarctic Ice Sheet collapse. Geophysical Research Letters 43, 2675–2682.

Swithinbank, C., Brunk, K., Sievers, J., 1988. A glaciological map of Filchner-Ronne ice shelf, Antarctica. Ann. Glaciol 11, 150–155.

Thomas, R.H., 1975. Liquid brine in ice shelves. Journal of Glaciology 14, 125–136.

Thomas, R.H., MacAyeal, D.R., Eilers, D.H., Gaylord, D.R., 1984. Glaciological studies on the Ross ice shelf, Antarctica, 1973–1978. Wiley Online Library.

Thyssen, F., Bombosch, A., Sandhäger, H., 1993. Elevation, ice thickness and structure mark maps of the central part of the Filchner-Ronne Ice Shelf. Polarforschung 62, 17–26.

Tigchelaar, M., Timmermann, A., Pollard, D., Friedrich, T., Heinemann, M., 2018. Local insolation changes enhance Antarctic interglacials: Insights from an 800,000-year ice sheet simulation with transient climate forcing. Earth and Planetary Science Letters 495, 69–78. https://doi.org/10.1016/j.epsl.2018.05.004

Timmermann, R., Hellmer, H.H., 2013. Southern Ocean warming and increased ice shelf basal melting in the twenty-first and twenty-second centuries based on coupled ice-ocean finite-element modelling. Ocean Dynamics 63, 1011–1026. https://doi.org/10.1007/s10236-013-0642-0

Todd, C., Stone, J., Conway, H., Hall, B., Bromley, G., 2010. Late Quaternary evolution of Reedy Glacier, Antarctica. Quaternary Science Reviews 29, 1328–1341. https://doi.org/10.1016/j.quascirev.2010.02.001

van de Berg, W.J., Broeke, M.R. van den, Reijmer, C.H., Meijgaard, E. van, 2006. Reassessment of the Antarctic surface mass balance using calibrated output of a regional atmospheric

climate model. Journal of Geophysical Research: Atmospheres 111. https://doi.org/10.1029/2005JD006495

Vaughan, D.G., Corr, H.F.J., Bindschadler, R.A., Dutrieux, P., Gudmundsson, G.H., Jenkins, A., Newman, T., Vornberger, P., Wingham, D.J., 2012. Subglacial melt channels and fracture in the floating part of Pine Island Glacier, Antarctica. J. Geophys. Res. 117, F03012. https://doi.org/10.1029/2012JF002360

Warren, C., Giannopoulos, A., Giannakis, I., 2016. gprMax: Open source software to simulate electromagnetic wave propagation for Ground Penetrating Radar. Computer Physics Communications 209, 163–170. https://doi.org/10.1016/j.cpc.2016.08.020

Warren, S.G., Roesler, C.S., Brandt, R.E., Curran, M., 2019. Green Icebergs Revisited. Journal of Geophysical Research: Oceans 0. https://doi.org/10.1029/2018JC014479

Warren, S.G., Roesler, C.S., Morgan, V.I., Brandt, R.E., Goodwin, I.D., Allison, I., 1993. Green icebergs formed by freezing of organic-rich seawater to the base of Antarctic ice shelves. Journal of Geophysical Research: Oceans 98, 6921–6928. https://doi.org/10.1029/92JC02751

Webster, J., Hawes, I., Downes, M., Timperley, M., Howard-Williams, C., 1996. Evidence for regional climate change in the recent evolution of a high latitude pro-glacial lake. Antarctic Science 8, 49–59. https://doi.org/10.1017/S0954102096000090

Webster-Brown, J., Gall, M., Gibson, J., Wood, S., Hawes, I., 2010. The biogeochemistry of meltwater habitats in the Darwin Glacier region (80°S), Victoria Land, Antarctica. Antarctic Science 22, 646–661. https://doi.org/10.1017/S0954102010000787

Weertman, J., 1974. Stability of the Junction of an Ice Sheet and an Ice Shelf. Journal of Glaciology 13, 3–11. https://doi.org/10.3198/1974JoG13-67-3-11

Whillans, I.M., Merry, C.J., 2001. Analysis of a shear zone where a tractor fell into a crevasse, western side of the Ross Ice Shelf, Antarctica. Cold Regions Science and Technology 33, 1–17. https://doi.org/10.1016/S0165-232X(01)00024-6

Zotikov, I.A., Zagorodnov, V.S., Raikovsky, J.V., 1980. Core drilling through the Ross Ice Shelf (Antarctica) confirmed basal freezing. Science 207, 1463–1465.

APPENDIX A

Table S 1: Cosmogenic nuclide and location data for samples from Darwin and Hatherton glaciers. Reported 1σ errors incorporate both production rate and analytical uncertainties. Blank cells indicate no measurement. All measurements are on quartz.

Sample	Lat.	Lon.	Elevation (m)	Thickness (cm)	Density (g cm^{3})	Horizon correction	[Be-10] (10^4 atoms g^{-1})	[Al-26] (10^5 atoms g^{-1})	[C-14] (10^5 atoms g^{-1})
13-HAT-004-LW	-79.92333	156.80100	1196	4	2.5	0.995	30.50 ± 0.65		
13-HAT-006-LW	-79.92666	156.84691	1259.7	4	2.5	1.000	31.24 ± 0.67		
13-HAT-007-LW	-79.92646	156.84644	1258.8	4	2.5	1.000	51.88 ± 1.10		
13-HAT-009-LW	-79.91775	156.80047	1061.3	5	2.65	0.997	19.87 ± 0.42		
13-HAT-010-LW	-79.91770	156.80041	1061.3	4	2.65	0.998	9.59 ± 0.32	6.20 ± 0.27	
13-HAT-018-LW	-79.91243	156.78796	1012.6	4.5	2.65	0.994	9.18 ± 0.28	6.81 ± 0.28	
13-HAT-020-LW	-79.91346	156.79340	1015.8	4	2.65	0.997	9.35 ± 0.22	6.69 ± 0.32	
13-HAT-029-LW	-79.89079	156.75929	1129.5	4	2.5	0.996	92.62 ± 1.96		
13-HAT-030-LW	-79.89234	156.75795	1133.2	4	2.5	0.996	60.31 ± 1.06		
13-HAT-031-LW	-79.89044	156.75995	1124.75	4	2.5	0.997	16.07 ± 0.35		
13-HAT-036-LW	-79.91424	157.05614	1127.5	6	2.65	0.989	433.01 ± 11.40		
13-HAT-041-LW	-79.91864	157.04753	998.2	5	2.5	0.997	22.69 ± 0.69		
13-HAT-042-LW	-79.91943	157.04586	969.2	2	2.5	0.997	99.01 ± 1.33		
13-HAT-044-LW	-79.93334	156.86501	1298.6	4	2.5	0.999	64.96 ± 1.19		
13-HAT-047-LW	-79.92941	156.85678	1267.8	4	2.5	0.999	34.45 ± 0.72		
13-HAT-049A-LW	-79.93291	156.96286	856.95	6	2.5	0.998	0.49 ± 0.05		
13-HAT-058-LW	-79.91696	156.90154	865.4	6.75	2.65	0.998	1.55 ± 0.07		
13-HAT-059-DV	-79.99374	155.53179	1285.3	7	2.5	0.993	9.14 ± 0.23		
13-HAT-060-DV	-79.99383	155.53026	1308.95	3.5	2.5	0.989	8.92 ± 0.44		
13-HAT-061-DV	-79.99464	155.52677	1298.7	5	2.5	0.992	9.41 ± 0.21		
13-HAT-063-DV	-79.99105	155.53415	1310.85	4.5	2.5	0.990	9.56 ± 0.23		
13-HAT-067-DV	-79.99795	155.51309	1418.4	6.25	2.5	0.997	14.40 ± 0.35	11.26 ± 0.41	
13-HAT-068-DV	-79.99867	155.51435	1405.2	3	2.5	0.997	15.91 ± 0.51	12.20 ± 0.45	
13-HAT-069-DV	-79.99942	155.51624	1388.5	6	2.5	0.997	14.68 ± 0.31	10.51 ± 0.42	
13-HAT-071-DV	-80.00268	155.50844	1468.15	3	2.5	0.998	253.93 ± 3.86	172.13 ± 3.46	
13-HAT-073-DV	-80.00271	155.50991	1469.25	3	2.5	0.998	244.21 ± 3.58	168.59 ± 3.25	
13-HAT-074-DV	-80.00293	155.51120	1465.6	7	2.5	0.997	260.85 ± 4.40	172.70 ± 3.20	
13-HAT-077-DV	-80.00269	155.51267	1466.2	4	2.5	0.999	302.37 ± 4.51	166.47 ± 3.11	
13-HAT-079-DV	-80.00256	155.51465	1463.3	4	2.5	0.998	239.11 ± 3.92	176.87 ± 3.46	
13-HAT-080-BV	-80.00230	155.51686	1460.5	3	2.5	0.998	226.16 ± 3.67	169.26 ± 3.22	
13-HAT-081-BV	-79.97580	155.45995	1358.2	5	2.5	0.999	11.55 ± 0.25		
13-HAT-082-BV	-79.97585	155.45925	1359.1	7	2.5	0.999	11.32 ± 0.28		

13-HAT-083-BV	-79.97585	155.45963	1359.1	4	2.5	0.997	11.72 ± 0.25		
13-HAT-086-BV	-79.97885	155.40348	1420.95	3.5	2.5	0.990	224.82 ± 3.34	165.29 ± 3.19	
13-HAT-087-BV	-79.97885	155.40348	1419	3.5	2.5	0.988	230.43 ± 3.33	165.23 ± 3.15	
13-HAT-088-BV	-79.97908	155.40314	1419.2	5	2.5	0.991	316.13 ± 5.13	164.67 ± 3.11	
13-HAT-099-BV	-79.97617	155.44690	1364.4	4	2.5	0.995	12.38 ± 0.24		
13-HAT-100-BV	-79.97563	155.48090	1321.4	3	2.5	0.997	10.01 ± 0.22		
13-HAT-102-BV	-79.97355	155.48655	1317.5	3.9	2.5	0.998	9.56 ± 0.22		
13-HAT-106-BV	-79.97134	155.50521	1236.7	3.5	2.5	0.998	6.32 ± 0.21		
13-HAT-111-BV	-79.96812	155.51457	1212.8	2	2.5	0.999	5.33 ± 0.15		
13-HAT-118-DAN	-79.98709	155.52618	1487.7	5	2.5	0.999	16.56 ± 0.46	12.82 ± 0.59	
13-HAT-119-DAN	-79.98717	155.52629	1485.1	5	2.5	0.998	16.43 ± 0.34	11.62 ± 0.40	3.45 ± 0.05
13-HAT-120-DAN	-79.98652	155.52658	1497.15	5	2.5	0.999	16.93 ± 0.50	10.91 ± 0.41	
13-HAT-121-DAN	-79.986	155.52882	1487.05	2.5	2.5	0.999	14.19 ± 0.40		
13-HAT-125-DAN	-79.98512	155.53307	1433.5	2.75	2.5	0.990	12.11 ± 0.26		
13-HAT-127-DAN	-79.98400	155.53654	1402.25	4	2.5	0.999	11.40 ± 0.30		
13-HAT-128-DAN	-79.98273	155.53733	1366.3	5	2.5	0.997	9.85 ± 0.22		
13-HAT-129-DAN	-79.98178	155.54128	1347.15	6.5	2.5	0.998	10.42 ± 0.33		
13-HAT-130-DAN	-79.97989	155.54394	1324.75	6.5	2.5	0.998	9.18 ± 0.53		
13-HAT-132-DAN	-79.97692	155.52992	1311.6	5	2.5	0.998	9.07 ± 0.24		
13-HAT-133-BV	-79.96676	155.53136	1187.55	7	2.5	0.999	115.74 ± 1.73		
13-HAT-137-UM	-79.94852	155.49588	1500	5	2.5	0.999	14.90 ± 0.41	10.74 ± 0.39	
13-HAT-138-UM	-79.94852	155.49588	1499	6	2.5	0.999	14.86 ± 0.54	11.92 ± 0.60	
13-HAT-140-UM	-79.94825	155.49541	1514.0	5	2.5	0.999	14.35 ± 0.48		
14-HAT-001-DH	-79.85766	159.08361	876.7	4.75	2.65	0.997	230.42 ± 4.82		
14-HAT-006-DH	-79.86803	159.29819	593	3.5	2.65	0.998	697.20 ± 41.27	312.09 ± 11.89	2.49 ± 0.07
14-HAT-008-DH	-79.83759	159.23672	385	5.5	2.65	0.997	25.03 ± 0.67		
14-HAT-009-DH	-79.83779	159.23359	376.9	4	2.65	0.997	139.95 ± 3.59		
14-HAT-011-DH	-79.83724	159.2241	389.7	4	2.65	0.997	5.44 ± 0.13		
14-HAT-012-DH	-79.89907	159.13856	341.35	7	2.63	0.999	2.88 ± 0.07		
14-HAT-014-DH	-79.89914	159.13362	333.8	6	2.76	0.998	2.48 ± 0.07		
14-HAT-015-DH	-79.89931	159.13302	327.3	5.5	2.69	0.993	2.47 ± 0.07		
14-HAT-016-DH	-79.89994	159.13287	303.4	7	2.67	0.991	1.88 ± 0.06		
14-HAT-017-DH	-79.89994	159.13287	303.4	4.5	2.62	0.996	2.11 ± 0.07		
14-HAT-022-DH	-79.89873	159.10245	376.8	6	2.58	0.999	3.53 ± 0.09		
14-HAT-024-DH	-79.89827	159.09121	413.1	4.5	2.62	0.998	4.02 ± 0.13		
14-HAT-026-DH	-79.89289	159.09048	472	6.25	2.65	0.999	371.75 ± 14.89	158.38 ± 3.63	1.26 ± 0.05
14-HAT-030-DH	-79.83676	159.17842	450.1	6.5	2.65	0.997	14.01 ± 0.35		
14-HAT-032-DH	-79.90332	159.13686	279.9	5	2.66	0.999	0.21 ± 0.02		0.31 ± 0.13
14-HAT-033-DH	-79.90332	159.13686	279.9	4	2.65	0.998	10.50 ± 0.23	6.49 ± 0.24	0.11 ± 0.04

14-HAT-035-DH	-79.85197	159.10872	813.00	5	2.65	0.998	929.96 ± 12.45	343.01 ± 8.09	1.24 ± 0.06
14-HAT-036-DH	-79.86430	159.16061	1287	7	2.65	1.000	2391.92 ± 97.03	965.54 ± 22.93	3.24 ± 0.13
14-HAT-039-DH	-79.85829	159.15805	1135	2.75	2.65	0.999	623.88 ± 25.90	358.05 ± 8.47	1.92 ± 0.07
14-HAT-040-MV	-80.07939	156.16582	1263.6	2.5	2.5	0.991	15.55 ± 0.33	11.46 ± 0.48	
14-HAT-041-MV	-80.07938	156.16663	1265.8	2.5	2.5	0.992	20.27 ± 0.48		
14-HAT-042-MV	-80.07918	156.17209	1269.9	3	2.5	0.992	14.84 ± 0.32	10.82 ± 0.51	
14-HAT-044-MV	-80.07903	156.17661	1270.95	3	2.5	0.991	17.26 ± 0.37	11.70 ± 0.40	
14-HAT-045-MV	-80.07822	156.12726	1247.4	3.5	2.65	0.995	51.49 ± 0.86		
14-HAT-046-MV	-80.07795	156.12637	1247.8	3.5	2.5	0.995	13.31 ± 0.29	9.63 ± 0.37	
14-HAT-048-MV	-80.05866	156.29645	1361.75	3.5	2.5	0.996	22.95 ± 0.46		
14-HAT-050-MV	-80.07715	156.16058	1233.9	4	2.5	0.994	11.88 ± 0.26		
14-HAT-052-MV	-80.07594	156.1655	1219.8	2.5	2.5	0.993	14.77 ± 0.36		
14-HAT-053-MV	-80.07577	156.16642	1214.7	6	2.5	0.993	10.23 ± 0.22		
14-HAT-056-MV	-80.07317	156.17001	1183.4	3	2.5	0.992	9.41 ± 0.20		
14-HAT-057-MV	-80.07303	156.17206	1178.7	5.5	2.5	0.992	9.07 ± 0.22		
14-HAT-059-MV	-80.07095	156.17406	1156.2	2	2.5	0.993	16.96 ± 0.38		
14-HAT-060-MV	-80.05932	156.28334	1334.45	1.5	2.5	0.998	18.99 ± 0.36		
14-HAT-063-MV	-80.05823	156.28662	1316.5	2	2.5	0.993	13.32 ± 0.53		
14-HAT-065-MV	-80.05791	156.28536	1302	4	2.65	0.996	21.52 ± 0.67	15.07 ± 0.52	
14-HAT-066-MV	-80.05748	156.27967	1310.4	2	2.5	0.999	23.93 ± 0.58		
14-HAT-067-MV	-80.05753	156.27868	1307.3	2	2.5	0.998	17.93 ± 0.38		
14-HAT-068-MV	-80.0451	156.12618	1227.4	2	2.5	0.988	9.34 ± 0.20		
14-HAT-069-MV	-80.04499	156.12692	1223.3	8	2.5	0.989	8.73 ± 0.30		
14-HAT-070-MV	-80.04627	156.10858	1340.8	2.5	2.5	0.989	13.99 ± 0.30	9.84 ± 0.40	

Table S 2: Cosmogenic nuclide data from the RB-2 core at the Pirrit Hills. Reported 1σ errors incorporate both production rate and analytical uncertainties.

Name	Depth (m)	[Be-10] (10^3 atoms g^{-1})	$[Al\text{-}26]_{quartz}$ (ppm)	[Al-26] (10^3 atoms g^{-1})	Al-26/Be-10
RB-2-016-025	0.16-0.25	4.43 ± 0.09	93.35 ± 0.21	15.25 ± 5.55	3.44 ± 1.27
RB-2-045-051	0.45-0.51	4.12 ± 0.10	98.31 ± 0.37	19.86 ± 3.54	4.82 ± 0.96
RB-2-065-071	0.65-0.71	3.96 ± 0.09	92.56 ± 0.44	23.77 ± 5.15	6.01 ± 1.40
RB-2-094-103	0.94-1.03	3.80 ± 0.09	90.24 ± 0.41	16.24 ± 3.76	4.28 ± 1.03
RB-2-132-139	1.32-1.39	4.12 ± 0.10	98.17 ± 0.53	20.29 ± 3.82	4.93 ± 1.02
RB-2-160-166	1.60-1.66	3.52 ± 0.10	95.18 ± 0.60	23.29 ± 3.87	6.62 ± 1.34
RB-2-200-209	2.00-2.09	4.15 ± 0.10	97.41 ± 0.35	24.43 ± 4.07	5.89 ± 1.06
RB-2-241-250	2.31-2.50	3.79 ± 0.09	89.80 ± 0.66	13.48 ± 2.83	3.55 ± 0.79
RB-2-279-288	2.79-2.88	4.20 ± 0.10	96.38 ± 0.30	16.70 ± 3.77	3.98 ± 0.94
RB-2-376-385	3.76-3.85	3.60 ± 0.09	89.98 ± 0.32	12.39 ± 3.21	3.45 ± 0.95
RB-2-425-434	4.25-4.34	3.68 ± 0.09	87.57 ± 0.04	18.40 ± 4.00	5.01 ± 1.18
RB-2-475-484	4.75-484	3.53 ± 0.09	92.50 ± 0.52	17.54 ± 3.14	4.97 ± 0.97
RB-2-528-536	5.28-5.36	3.54 ± 0.09	89.91 ± 0.64	15.98 ± 3.05	4.52 ± 0.92
RB-2-582-591	5.82-5.91	3.19 ± 0.09	90.91 ± 1.06	10.72 ± 3.35	3.36 ± 1.23
RB-2-639-648	6.39-6.48	3.69 ± 0.09	92.44 ± 0.66	18.46 ± 3.51	5.00 ± 1.06
RB-2-698-707	6.98-7.07	3.63 ± 0.10	102.06 ± 0.75	14.08 ± 2.98	3.87 ± 0.87
RB-2-759-768	7.59-7.68	3.61 ± 0.10	99.05 ± 0.34	19.52 ± 3.67	5.40 ± 1.10

VITA

Trevor R. Hillebrand
Ph.D. Candidate in Earth and Space Sciences
University of Washington

Research Interests

I investigate ice dynamics during deglaciations, feedbacks between erosion and ice dynamics, and interglacial ice sheet collapse. I incorporate records of ice sheet fluctuations from cosmogenic isotopes and ice-penetrating radar into numerical models of ice flow to extend local measurements to regional and continental scales.

Education

June 2019 (expected)	Ph.D.	Earth and Space Sciences	University of Washington	GPA: 3.76/4
Advisor: Dr. John Stone		Dissertation: Quaternary grounding-line fluctuations in Antarctica		
March 2018	M.Sc.	Applied Mathematics	University of Washington	GPA: 3.75/4
June 2016	Ph.C.	Earth and Space Sciences	University of Washington	
Dec. 2012	B.A.	Geology (High Honors), Music	University of California Berkeley	GPA: 3.79/4
Advisors: Dr. Kurt Cuffey & Dr. David Shuster		Honors Thesis: A comparison of tectonics of the eastern Sierra Nevada, CA in the vicinity of Mt. Whitney and Lee Vining, using (U-Th)/He and $^{4}He/^{3}He$ thermo-chronometry: Preliminary results and thermal modeling		

Professional Positions

Los Alamos National Laboratory	Starting 2019	Postdoctoral Research Associate
University of Washington	2013-present	Teaching and Research Assistant
University of Washington	June – Sept. 2013	Lab Assistant
Berkeley Geochronology Center	Sept. – Dec. 2012	Undergraduate Research Assistant
United States Forest Service	May – Aug. 2012	Physical Science Technician
Berkeley Geochronology Center	May – Aug. 2011	Undergraduate Research Assistant
UCSB Institute for Crustal Studies	May – Aug. 2010	Undergraduate Research Assistant

Research Grants and Fellowships

National Science Foundation Earth Sciences Postdoctoral Fellowship: *Did multiple scales of erosion beneath the Laurentide Ice Sheet control Pleistocene glacial cycles?* 2019 ($174,000; declined)

University of Washington Quaternary Research Center Award: *Constraining past Antarctic Ice Sheet thickness using cosmogenic ^{14}C in bedrock*. 2017 ($6,750)

Scientific Committee on Antarctic Research travel grant to attend Past Antarctic Ice Sheet conference in Trieste, Italy. 2017 ($1,210)

University of Washington Earth and Space Sciences Inquisitive Graduate Student Support Fund Fellowship & Jody Bourgeois Graduate Student Support Fund Fellowship: *Holocene deglaciation of the Ross Sea, Antarctica*. 2015 ($2,500)

University of Washington Earth and Space Sciences Peter Misch Fellowship: *Surface evolution of Khumbu Glacier: quantifying the effects of climate change at the Himalayan crest*. 2014 ($800)

University of California Berkeley Charles Ramsden Undergraduate Research Fellowship: *Tectonic evolution of the eastern Sierra Nevada, California*. 2012 ($2,400)

Awards and Honors

UC Berkeley High Honors in Geology, Dec. 2012
UC Berkeley Distinction in General Scholarship, Dec. 2012
UC Berkeley Dean's Honors List, Dec. 2012

Patents

None

Peer Reviewed Publications

Spector, P, Stone, J, Pollard, D, **Hillebrand, TR**, Lewis, C, Gombiner, J (2018). West Antarctic Sites for Subglacial Drilling to Test for Past Ice-Sheet Collapse. *The Cryosphere* 12(8): 2741–57.

Balco, G, Todd, C, Huybers, K, Campbell, S, Vermeulen, M, Hegland, M, ... & **Hillebrand, TR** (2016). Cosmogenic-nuclide exposure ages from the Pensacola Mountains adjacent to the Foundation Ice Stream, Antarctica. *American Journal of Science*, *316*(6), 542-577.

Manuscripts in preparation

Hillebrand, TR, King, C., Koutnik, MR, Stone, J, Hall, BL, Conway, H, Pollard, D, Goehring, BM, Nichols, KA, and Gillespie, M. Manuscript in preparation. Holocene grounding-line retreat and deglaciation of the Darwin-Hatherton glacier system, Antarctica

Hillebrand, TR, Spector, P, Pollard, D, and Stone, J. Manuscript in preparation. West Antarctic Ice Sheet fluctuations during three Pleistocene interglacials.

Hillebrand, TR, Conway, H., Martín, C., Paden, J., Koutnik, K.R., Winberry, J.P, Cooley, L.J.. Manuscript in preparation. Structure of Crary Ice Rise revealed by radio-echo sounding

King, C., B. Hall, J. Stone, & **TR Hillebrand**. Manuscript in prep. Holocene-Age Local Last Glacial Maximum and Subsequent Deglaciation, Lake Wellman region, Hatherton Glacier, Antarctica

Martín, C., **TR Hillebrand**, H. Conway, J. P. Winberry, M. Koutnik, H. F. J. Corr, K.W. Nicholls, C.L. Stewart, J. Kingslake, A. Brisbourne. Manuscript in prep. Radar polarimetry at Crary Ice Rise, Antarctica, reveals details of ice-flow reorganization over the last millennium

Presentations & Abstracts

Hillebrand, TR, Spector, P, Pollard, D, and Stone, J. West Antarctic Ice Sheet fluctuations during Pleistocene super-interglacials (2019). Oral presentation at the UW ESS Research Gala

Hillebrand, TR, King, C., Koutnik, MR, Stone, J, Hall, BL, Conway, H, Pollard, D, Goehring, BM, Nichols, KA, and Gillespie, M. (2018). Antarctic Ice Sheet retreat in the western Ross Embayment since the Last Glacial Maximum constrained by geochronology and ice flow modeling. In *AGU Fall Meeting Abstracts*

Spector, P, J Stone, **TR Hillebrand**, & J Gombiner (2017). Selecting Antarctic sites for subglacial bedrock recovery to test for past ice-sheet collapse, an example from the Pirrit Hills. Oral presentation at Geological Society of America (GSA) meeting in Seattle, WA

Hillebrand, TR & 9 others (2017). Holocene grounding-line retreat and deglaciation of Darwin and Hatherton glaciers, Antarctica. Poster presentation at the West Antarctic Ice Sheet (WAIS) Workshop in Camp Casey, WA

Conway, H, **TR Hillebrand** & 4 others (2017). The grounding and formation of Crary Ice Rise. Oral presentation at the West Antarctic Ice Sheet Workshop in Camp Casey, WA

Gombiner, J & 6 others (**TR Hillebrand** is 7th author) (2017). Optical dating of past ice-free conditions in West Antarctica. Poster presentation at the West Antarctic Ice Sheet Workshop in Camp Casey, WA

Stone, JO, P Spector, **TR Hillebrand** & 8 others (2017). West Antarctic Ice Sheet history from subglacial bedrock core. Invited oral presentation at the West Antarctic Ice Sheet Workshop in Camp Casey, WA

Hillebrand, TR & 9 others (2017). Delayed deglaciation of Darwin and Hatherton glaciers, Antarctica. Poster presentation at Past Antarctic Ice Sheet Dynamics conference in Trieste, Italy

Hillebrand, TR & 8 others (2017). Delayed deglaciation of Darwin Glacier, Antarctica. Oral presentation at UW Earth and Space Sciences Graduate Research Gala in Seattle, WA

Martin, C, **TR Hillebrand** & 8 others (2017). Radar polarimetry at Crary Ice Rise, Antarctica, reveals details of ice-flow reorganization over the last millennium. Oral presentation at EGU General Assembly in Vienna.

Hillebrand, TR & 6 others (2016). Structure of Crary Ice Rise, Antarctica revealed by ultra-high frequency radio echo sounding. Poster presentation at WAIS Workshop in Sterling, VA

Hillebrand, TR & 8 others (2016). High frequency radio echo sounding of Crary Ice Rise, Antarctica. Oral presentation at UW Earth and Space Sciences Graduate Research Gala in Seattle, WA

King, C, B Hall, JO Stone, **TR Hillebrand** (2016). Radiocarbon chronology of the local Last Glacial Maximum and subsequent recession alongside Hatherton Glacier, Antarctica. Poster presentation at WAIS Workshop in Sterling, VA

Hillebrand, TR & 5 others (2015). Holocene deglaciation of the Darwin-Hatherton glacier system and the Ross Embayment, Antarctica. Oral presentation at WAIS Workshop in Loveland, CO

Hillebrand, TR & 5 others (2015). Holocene deglaciation of the Ross Sea, Antarctica. Oral presentation at UW Earth and Space Sciences Graduate Research Gala in Seattle, WA

King, C, B Hall, JO Stone, **TR Hillebrand** (2015). The timing of the Last Glacial Maximum in the Lake Wellman region, Hatherton Glacier, Antarctica. Oral presentation at WAIS Workshop in Loveland, CO

Koutnik, M, H Conway, **TR Hillebrand**, JO Stone, & P Spector (2015). Assimilating geochronological data into ice-flow models to constrain the deglaciation of Transantarctic outlet glaciers. Poster presentation at WAIS Workshop in Loveland, CO

Hillebrand, TR & 5 others (2014). Late Quaternary ice elevations of Hatherton Glacier, Antarctica. Oral presentation at GSA General Meeting in Vancouver, BC

Hillebrand, TR, Barker, A.D., & Hallet, B. (2013). Surface evolution of Khumbu Glacier, Nepal. Oral presentation at Northwest Glaciologists Meeting at Simon Fraser University, BC

Field Experience

Nov. 2016 – Feb. 2017	Pirrit Hills, West Antarctica
July – Aug. 2016	Teanaway River, Cascade Mountains, WA
Nov. – Dec. 2015	Crary Ice Rise, Antarctica
Nov. 2013 – Jan. 2014 & Dec. 2014 – Jan. 2015	Darwin and Hatherton Glaciers, Antarctica
April – May 2013	Khumbu Glacier, Everest Region, Nepal
March 2013	Kennicott Glacier, AK

May – Sept. 2012	Eastern Sierra Nevada, CA
July - Aug. 2011	Pioneer Mountains, MT

Service Activities

2017 – present UW Earth & Space Sciences *Diversity Committee member*

2016 - 2017 *Graduate student representative* to UW Earth & Space Sciences Preliminary Exams

2015 - 2016 *Outreach Coordinator* for UW Earth & Space Sciences Rockin' Out K-12 outreach program. Acting coordinator March 2017. During my time as coordinator, we taught 853 students in small classroom visits, and presented at science nights with combined student and family attendance of over 2,200.

2014 – present *Volunteer Instructor/Presenter* for Rockin' Out at various elementary and middle school science nights, classroom visits, and fieldtrips; at UW glaciology exhibit at annual Polar Science Weekend.

Teaching experience

Teaching Assistant at University of Washington

Spring 2019	Introduction to Earth Sciences
Winter 2018	Earth Materials
Spring 2016	Economic Geology
Fall 2014	Introduction to Earth Sciences; The Great Ice Age
Winter 2014	Earth Materials

Technical Skills

Fieldwork	Glacial geologic mapping and sampling, ground based ice-penetrating radar surveys, GPS strain grid surveys
Laboratory	Mineral separation, purification, & dissolution; ICP-OES elemental analysis; column chemistry; AMS Al & Be cathode preparation
Data analysis	Inverse theory, parameter estimation, geospatial analysis in QGIS, spectral analysis, principal component analysis, image processing, dynamic mode decomposition
Numerical	Finite-difference and finite-volume modeling of ice sheet and glacier flow, finite element methods, spectral methods, finite-difference time-domain methods for radar waveform modeling (currently learning)
Programming	MATLAB, Python, bash, tcsh, some Fortran